

# Magnetic Domain States and Critical Sizes in the Titanomagnetite Series

Brendan J Cych<sup>1</sup>, Greig Paterson<sup>1</sup>, Lesleis Nagy<sup>1</sup>, Wyn Williams<sup>2</sup>, and Bruce Moskowitz<sup>3</sup>

<sup>1</sup>University of Liverpool

<sup>2</sup>University of Edinburgh

<sup>3</sup>University of Minnesota

April 16, 2024

## Abstract

The minerals carrying the magnetic remanence in geological samples are commonly a solid solution series of iron-titanium spinels known as titanomagnetites. Despite the range of compositions within this series, micromagnetic studies that characterize the magnetic domain structures present in these minerals have typically focused on magnetite. No studies systematically comparing the domain-states present in titanomagnetites have been undertaken since the discovery of the single vortex (SV) structure and the advent of modern micromagnetism. The magnetic properties of the titanomagnetite series are known to vary with composition, which may influence the domain states present in these minerals, and therefore the magnetic stability of the samples bearing them.

We present results from micromagnetic simulations of titanomagnetite ellipsoids of varying shape and composition to find the size ranges of the single domain (SD) and SV structures. These size ranges overlap, allowing for regions where the SD and SV structures are both available. These regions are of interest as they may lead to magnetic instability and ‘pTRM tails’ in paleointensity experiments. We find that although this SD+SV zone occupies a narrow range of sizes for equidimensional magnetite, it is widest for intermediate (TM30-40) titanomagnetite compositions, and increases for both oblate and prolate particles, with some compositions and sizes having an SD+SV zone up to 100s of nm wide. Our results help to explain the prevalence of pTRM tail-like behavior in paleointensity experiments. They also highlight regions of particles with unusual domain states to target for further investigation into the definitive mechanism behind paleointensity failure.

1                   **Magnetic Domain States and Critical Sizes in the**  
2                                   **Titanomagnetite Series**

3                   **Brendan Cych<sup>1</sup>, Greig A. Paterson<sup>1</sup>, Lesleis Nagy<sup>1</sup>, Wyn Williams<sup>2</sup>, Bruce**  
4                                   **Moskowitz<sup>3</sup>**

5                   <sup>1</sup>Department of Earth, Ocean and Environmental Sciences, University of Liverpool, Liverpool, L69 7ZE,  
6                                   UK

7                   <sup>2</sup>School of GeoSciences, University of Edinburgh, Grant Institute, West Mains Road, Edinburgh, EH9  
8                                   3JW, UK

9                   <sup>3</sup>Institute for Rock Magnetism, Department of Earth and Environmental Sciences, University of  
10                                   Minnesota, 150 John T. Tate Hall, 116 Church St. SE, Minneapolis, MN 55455U, USA

11                   **Key Points:**

- 12                   • We systematically map out the domain states in titanomagnetite as a function of  
13                                   shape and composition.  
14                   • Our results highlight ranges of compositions, shapes and sizes which contain un-  
15                                   reliable paleomagnetic recorders.  
16                   • For certain shapes and compositions, these regions span hundreds of nanometers,  
17                                   representing a significant proportion of remanence carriers.

## 18 Abstract

19 The minerals carrying the magnetic remanence in geological samples are commonly a  
 20 solid solution series of iron-titanium spinels known as titanomagnetites. Despite the range  
 21 of possible compositions within this series, micromagnetic studies that characterize the  
 22 magnetic domain structures present in these minerals have typically focused on magnetite.  
 23 No studies systematically comparing the domain-states present in titanomagnetites have  
 24 been undertaken since the discovery of the single vortex (SV) structure and the advent  
 25 of modern micromagnetism. The magnetic properties of the titanomagnetite series are  
 26 known to vary strongly with composition, which may influence the domain states present  
 27 in these minerals, and therefore the magnetic stability of the samples bearing them.

28 We present results from micromagnetic simulations of titanomagnetite ellipsoids  
 29 of varying shape and composition to find the size ranges of the single domain (SD) and  
 30 SV structures. These size ranges overlap, allowing for regions where the SD and SV struc-  
 31 tures are both available. These regions are of interest as they may lead to magnetic in-  
 32 stability and “pTRM tails” in paleointensity experiments. We find that although this SD+SV  
 33 zone occupies a narrow range of sizes for equidimensional magnetite, it is widest for in-  
 34 termediate (TM30-40) titanomagnetite compositions, and increases for both oblate and  
 35 prolate particles, with some compositions and sizes having an SD+SV zone up to 100s  
 36 of nm wide. Our results help to explain the prevalence of pTRM tail-like behavior in pa-  
 37 leointensity experiments. They also highlight regions of particles with unusual domain  
 38 states to target for further investigation into the definitive mechanism behind paleoin-  
 39 tensity failure.

## 40 Plain Language Summary

41 Rocks that record Earth’s magnetic field often contain the mineral magnetite. The  
 42 crystal structure of magnetite allows titanium atoms to substitute for iron, giving rise  
 43 to a range of minerals known as titanomagnetites. The internal magnetic structure of  
 44 titanomagnetite particles in rocks, known as the “domain structure”, controls the abil-  
 45 ity of that particle to record magnetic fields. Particles with certain kinds of domain struc-  
 46 ture are unstable magnetic recorders, which can cause problems for experiments trying  
 47 to determine Earth’s magnetic field strength in the past (paleointensity experiments).  
 48 Although the domain structures in magnetite are well understood, there are no recent  
 49 studies which describe them in titanomagnetites.

50 In this paper, we simulate the domain structures in small titanomagnetite parti-  
 51 cles and map these out as a function of size, shape and chemical composition. In doing  
 52 so, we identify types of magnetic particles with multiple possible domain structures that  
 53 may give rise to unstable magnetizations. Our results indicate that some titanomagnetite  
 54 particles may have unstable magnetizations over a much larger range of sizes than has  
 55 previously been seen in magnetite. This wide range of sizes could explain the high fail-  
 56 ure rates of paleointensity experiments.

## 57 1 Introduction

58 Magnetite is one of the most important magnetic minerals in igneous and sedimen-  
 59 tary rocks, commonly forming during the crystallization of basaltic magmas, and in sed-  
 60 iments through erosional and biogenic processes. Stoichiometrically pure magnetite ( $\text{Fe}_3\text{O}_4$ )  
 61 is a well studied magnetic mineral, but in nature it forms a solid solution series with ti-  
 62 tanium rich ulvospinel ( $\text{Fe}_2\text{TiO}_4$ ). Titanomagnetite compositions within the series  $\text{Fe}_{3-x}\text{Ti}_x\text{O}_4$   
 63 ( $0 \leq x \leq 1$ ) are represented using the notation  $\text{TM}x$  (e.g.  $x = 0.6$  is  $\text{TM}60$ ). Funda-  
 64 mental magnetic properties of the titanomagnetites, including the Curie temperature (Nishitani  
 65 & Kono, 1983), saturation magnetization (Bleil, 1976) and magnetocrystalline anisotropy  
 66 constants (Kakol et al., 1994), have been observed to vary across the solid solution se-

67 ries. The distribution of Curie temperatures in igneous rocks compiled from a compi-  
 68 lation of 38 papers indicate that approximately 75% of paleomagnetic samples do not  
 69 contain pure magnetite (see supplementary information for detailed references). Instead,  
 70 they suggest that compositions from TM0 to TM60 are prevalent along with other min-  
 71 erals. Despite this wide range of compositions and behaviours in nature, the rock mag-  
 72 netic properties of titanomagnetites and their influences on paleomagnetic experiments  
 73 are understudied.

74 Rocks containing titanomagnetites are used to determine Earth’s magnetic field strength  
 75 and direction in the distant past. This information has many practical applications in  
 76 the geosciences, from detecting the age of archeological samples, to determining the mo-  
 77 tion of tectonic plates and the nucleation age of Earth’s inner core. The fundamental physics  
 78 that explain how a rock can record a thermal remanent magnetization (TRM) by cool-  
 79 ing in a field was first described by Louis Néel (Néel, 1949). This work assumes that the  
 80 magnetic particles contained within rocks are uniformly magnetized in a structure known  
 81 as “single-domain” (hereafter referred to as SD). Unfortunately, the SD structure is only  
 82 energetically efficient over a small range of particle sizes, and the majority of the mag-  
 83 netization in natural materials is carried by particles in other states, as we show below.  
 84 Consequently, paleomagnetic experiments often produce results that are complicated and  
 85 difficult to interpret. A better understanding of the domain states present in magnetic  
 86 materials is necessary to understand this behavior, and to ensure that paleomagnetists  
 87 can obtain accurate results.

88 To determine the dominant domain states of a magnetic particle, researchers use  
 89 the micromagnetic modelling approach of Brown (1963). This technique was adapted  
 90 by Fredkin and Koehler (1987) into a computational finite-element based technique, which  
 91 finds stable magnetization states that minimize the energy of the particle. Some of the  
 92 earliest findings from this approach demonstrated that magnetite particles sized approx-  
 93 imately 100 nm - 1  $\mu$ m have magnetizations which curl in a “vortex” shape around a uni-  
 94 form core, known as the Single Vortex (SV) structure (Schabes & Bertram, 1988; W. Williams  
 95 & Dunlop, 1989).

96 Recent work has shown that there is an “unstable zone” (where particle relaxation  
 97 times drop precipitously) in equidimensional magnetite particles at the lower size limit  
 98 of the SV structure. In this region, the dominant domain state is a single vortex with  
 99 the vortex core aligned along a magnetocrystalline hard axis direction . The energy needed  
 100 to escape this state is small, and so it is not stable over geological timescales. Nagy et  
 101 al. (2022) additionally showed that competition between shape easy- and hard-aligned  
 102 SV states in magnetite can produce complicated “partial TRM (pTRM) tail” behaviour  
 103 similar to that frequently seen in paleointensity experiments (e.g. Bol’Shakov, 1979; Dun-  
 104 lop & Özdemir, 2001; Riisager & Riisager, 2001; Santos & Tauxe, 2019).

105 Several studies have focused on determining the range of sizes and shapes over which  
 106 domain states are stable in metallic iron (Muxworthy & Williams, 2015), magnetite (Muxworthy  
 107 & Williams, 2006; Nagy et al., 2019), and greigite (Muxworthy et al., 2013; Valdez-Grijalva  
 108 et al., 2018). Despite the range of titanomagnetite compositions prevalent in nature, there  
 109 has been little work published on domain states in titanomagnetites since Butler and Baner-  
 110 jee (1975). That study showed that the size range over which the SD structure was stable  
 111 varied as a function of TM composition. Moskowitz (1980) and Moskowitz and Halgedahl  
 112 (1987) followed this work, calculating this size range for TM60 as a function of oxida-  
 113 tion, temperature and stress. These two studies were undertaken before the discovery  
 114 of the SV structure, instead considering a transition between a single domain and the  
 115 two-domain structure of Kittel (1949). Muxworthy and Williams (2006) used micromag-  
 116 netic modelling to determine the range of sizes for which the SD and SV structures were  
 117 available in elongated magnetite cuboids. This range of sizes differed significantly from  
 118 that of Butler and Banerjee (1975), but a modern micromagnetic approach was not ap-  
 119 plied to other TM compositions. Khakhalova et al. (2018) simulated single and multi-

120 vortex states in a large pyramidal TM54 particle, but did not explore the variation in  
121 domain state with the size and shape of particles.

122 In this paper, we present results from a series of micromagnetic models using the  
123 Micromagnetic Earth Related Robust Interpreted Language Laboratory (MERRILL; Ó  
124 Conbhuí et al., 2018) software package, v1.8.6p. Each simulation determines the range  
125 of possible sizes over which the single domain and single vortex structures can exist us-  
126 ing a “size hysteresis” algorithm (e.g. Witt et al., 2005; Muxworthy & Williams, 2006,  
127 2015; Nagy et al., 2019) where a minimum energy state is calculated in a titanomagnetite  
128 particle whilst progressively varying its size (described fully in Section 2.1). We perform  
129 these simulations for ellipsoidal titanomagnetite particles of varying composition and ax-  
130 ial ratio, from oblate to prolate. Our results, which are presented in Section 3 give the  
131 size ranges for the SD and SV structures for a range of TM compositions and prolate  
132 and oblate particles. This expands on the existing results of Muxworthy and Williams  
133 (2006) for prolate magnetites by more than an order of magnitude. We discuss the im-  
134 plications of these results, as well as the potential impact on paleomagnetic experiments  
135 in Section 4.

## 136 2 Methodology

### 137 2.1 The size hysteresis algorithm

138 For each geometry and titanomagnetite composition in this paper, we use a “size  
139 hysteresis” algorithm. A graphical example for a sphere of TM25 is shown in Figure 1.  
140 The algorithm works as follows:

- 141 1. For a 40 nm particle of a particular titanomagnetite composition and geometry,  
142 start with a uniform magnetization aligned along one of the magnetocrystalline  
143 easy axes in zero external field. An energy minimization is performed using MER-  
144 RILL on this particle, producing a magnetization that is a local energy minimum  
145 (LEM) state.
- 146 2. The magnetization is taken and scaled up to a particle of a slightly larger size. An  
147 energy minimization is then performed on the new particle size. We define our size  
148 using the diameter of a sphere with equivalent volume (referred to as ESVD; equiv-  
149 alent spherical volume diameter). We increase the particle size by 10 nm when the  
150 ESVD is between 40 and 250 nm, and steps of 25 nm are used from 250 to 500  
151 nm.
- 152 3. For a certain size range, the particle will remain in the SD structure (Figure 1 i.),  
153 but at some critical size, the SD structure stops being energetically favorable, and  
154 the domain state collapses to the SV structure (Figure 1 ii.). We call the diam-  
155 eter associated this size  $d_{\max}$ , which is defined as being the center point between  
156 the SD and SV structures (e.g. between Figure 1 i. and ii.).
- 157 4. We continue this process of scaling the magnetization onto particles of progres-  
158 sively larger sizes and minimizing the energy, repeating up to a size of 500 nm.
- 159 5. After reaching 500 nm, we reverse the process, mapping the magnetization onto  
160 progressively smaller particles and minimizing the energy. At some point, (between  
161 Figure 1 iii. and iv.), the particle transitions from the SV structure to the SD struc-  
162 ture. We call this size  $d_{\min}$ , which may differ from  $d_{\max}$ .

163 As can be seen from Figure 1, the critical sizes for transitioning between the SD  
164 and SV structures and vice-versa are not the same, with  $d_{\max}$  occurring at a larger size  
165 (165 nm) than  $d_{\min}$  (105 nm). During the “shrinking” branch of the magnetization, we  
166 observe a hard-aligned vortex (Figure 1 iii.). The region between  $d_{\min}$  and  $d_{\max}$  is there-  
167 fore of interest as it may contain the “unstable zone” of Nagy et al. (2017).

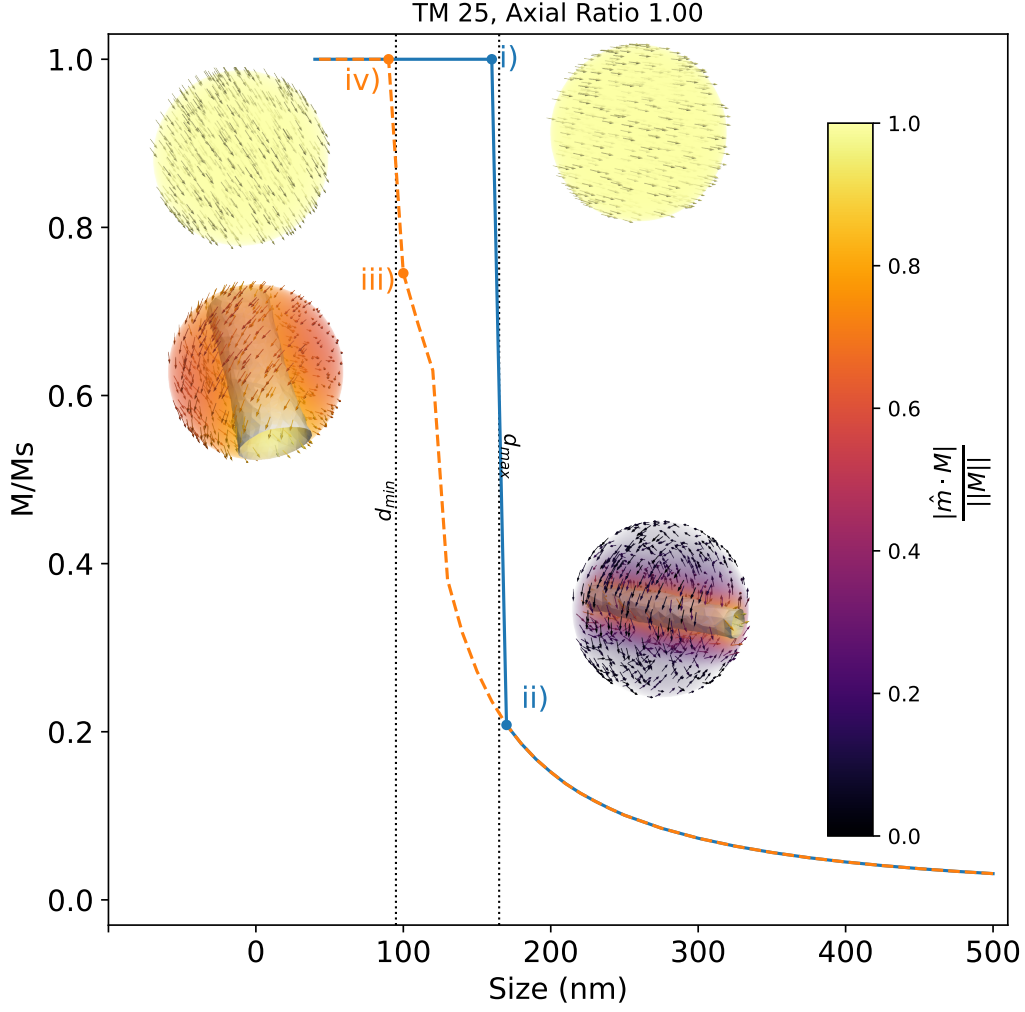


**Figure 1.** Ratio of the magnetization over the saturation magnetization ( $M/M_s$ ) plotted against EVSD (nm) in a “size hysteresis loop” for a sphere of TM25. The blue solid line represents the magnetization as the particle is grown from 40 from 500 nm, and the orange dashed line represents the magnetization as it is shrunk from 500 nm to 40 nm. Example magnetization states from the loop are shown at points i - iv). Vectors represent the direction of the magnetization at that location in the particle. Grey cylinder in ii) and iii) represents an isosurface where the relative helicity ( $h_{rel}$ , described in the supplemental information) is 0.95. Colors represent the absolute value of the dot product of these vectors with the direction of the net magnetization, with lighter yellow regions being aligned with the net magnetization, and darker purple regions being perpendicular. The magnetization transitions from the SD to the vortex state between i) and ii) (160-170 nm) and the magnitude of the magnetization continues to be reduced up to 500 nm due to the tightening of the vortex core. The vortex rotates to a magnetocrystalline hard axis direction between ii) and iii) and transitions back into a single domain state between iii) and iv) (100-90 nm) along a different easy direction.  $d_{min}$  and  $d_{max}$  are plotted as vertical lines.

168

## 2.2 Compositions and geometries

169

170

171

172

173

174

175

176

In this study, we will test the effects of titanomagnetite composition as well as shape on  $d_{\max}$  and  $d_{\min}$ . To produce a micromagnetic model using a particular material, fundamental material parameters are needed: the Curie temperature  $T_c$ , saturation magnetization  $M_s$ , exchange constant  $A_{\text{ex}}$  and magnetocrystalline anisotropy constants  $k_1$  and  $k_2$ . An extensive set of experimental data from previous work was compiled. Polynomial fits to these data were used to obtain functions that can return the material parameters for a given TM composition. Details of the datasets and resulting parameters used in this study are given in the Supplemental Material.

177

178

179

180

181

182

183

184

185

186

187

188

189

190

We applied the size hysteresis algorithm to ellipsoids of rotation with thirteen different axial ratios, logarithmically spaced between 1/3 and 3. A set of thirteen different titanomagnetite compositions was used, in 5% increments from 0% to 60% Ti. Tetrahedral meshes were produced for each size, shape and composition using the Coreform Cubit software package (Coreform LLC, 2017). The coarseness of the mesh used depended on the size of the geometry (keeping minimum number of elements to  $\sim 15000$ ) and the exchange length ( $\lambda_{\text{ex}}$ ; Rave et al., 1998) of the material. For some combinations of composition and geometry,  $d_{\max}$  was not reached by a size of 500 nm. In these cases, we ran the algorithm to a size of 1  $\mu\text{m}$  (in steps of 50 nm to 800 nm, then 100 nm to 1  $\mu\text{m}$ ), with a set of meshes using a maximum of a million elements. This meant that some meshes exceeded  $\lambda_{\text{ex}}$  and so  $d_{\max}$  values greater than 500 nm should be considered less precise. If  $d_{\max}$  was greater than 1  $\mu\text{m}$ , then it was not reported, and  $d_{\min}$  was instead obtained by forcing a vortex state initial condition at 500 nm and proceeding with the “shrinking” branch as normal.

191

192

193

194

195

196

197

198

199

For each composition and geometry, two size hysteresis simulations were run, one in which the major axis of the ellipsoid was aligned with the magnetocrystalline easy axis of the material (referred to as “magnetocrystalline easy-shape easy” or ME-SE), and one in which it was aligned with the magnetocrystalline hard axis (referred to as “magnetocrystalline hard-shape easy” or MH-SE). The results displayed in Section 3 were produced by taking the maximum  $d_{\max}$  and minimum  $d_{\min}$  of the two datasets for each composition and geometry, and the resulting surfaces were interpolated by a 2d cubic spline using the SciPy package (Virtanen et al., 2020). The difference between results from the ME-SE and MH-SE datasets are discussed in Sections 3.2 and 3.3.

200

201

202

203

204

205

206

207

208

209

210

211

The LEMs at each step in the size hysteresis loop were visualized using the ParaView software (Ayachit, 2015). For each visualization, the relative helicity  $h_{\text{rel}}$  was calculated (see supplementary material for details). To determine  $d_{\min}$  and  $d_{\max}$ , the SV structure was identified by the presence of a coherent cylindrical isosurface at  $h_{\text{rel}}=0.95$  containing a “vortex core” intersecting the surface of the particle in two places, and the SD structure was identified by the absence of such a core. Examples of SV structures with vortex cores can be seen in Figure 1 ii and iii). When visualizing LEM states, the volume and magnetization arrows are colored by the absolute cosine of the angle between the individual magnetization vectors and the particle’s net magnetization. The lighter colours in the cores of vortex structures demonstrate that the bulk of the magnetization is carried in this core, and that the volume of the core influences the magnitude of the net magnetization.

## 212 3 Results

### 213 3.1 Anisotropy energies of the titanomagnetite series

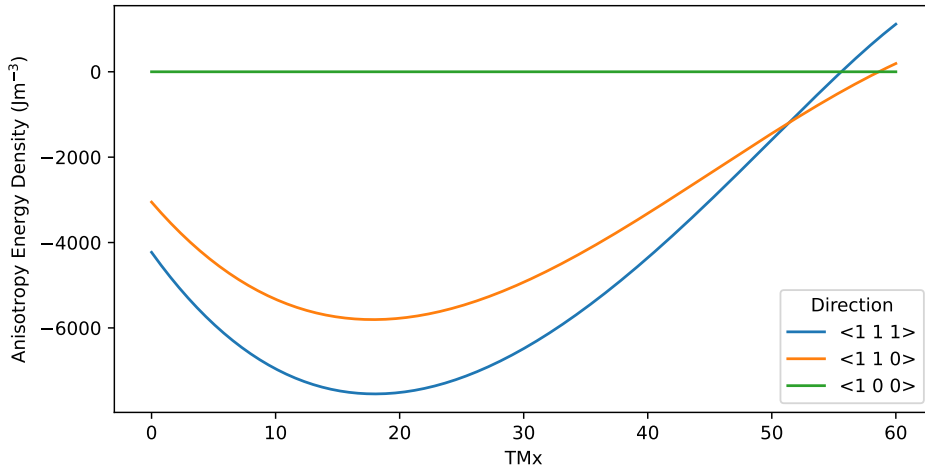


**Figure 2.** Magnetocrystalline anisotropy energy densities for an SD titanomagnetite particle as a function of composition. Different coloured lines are the anisotropy energy density for different magnetocrystalline directions. The line with the lowest (most negative) magnetocrystalline energy density is the easy axis.

214 Figure 2 shows the magnetocrystalline energy densities in SD titanomagnetites for  
 215 the  $\langle 1\ 0\ 0 \rangle$ ,  $\langle 1\ 1\ 0 \rangle$  and  $\langle 1\ 1\ 1 \rangle$  directions obtained from our fit to experimental data  
 216 for the  $k_1$  and  $k_2$  anisotropy constants. The magnetocrystalline easy axis for a particle  
 217 can be determined by the lowest (most negative) energy. Anisotropy properties change  
 218 significantly across the titanomagnetite series, the easy axis is along  $\langle 1\ 1\ 1 \rangle$  for TM0  
 219 - 50, changing to  $\langle 1\ 1\ 0 \rangle$  at  $\sim$  TM51 and  $\langle 1\ 0\ 0 \rangle$  at  $\sim$  TM59. The hard axis is  $\langle 1$   
 220  $0\ 0 \rangle$  from TM0 - 55 and changes to  $\langle 1\ 1\ 1 \rangle$  just above TM55. The difference in anisotropy  
 221 energy between the easy and hard directions reaches a maximum at  $\sim$  TM20, and is sig-  
 222 nificantly smaller at high TM compositions ( $\geq$ TM40).

### 223 3.2 Observed states

224 Examples of typical states observed during the size hysteresis algorithm are shown  
 225 in Figures 1 and 3. Spherical particles behaved as in Figure 1, with the SD structure chang-  
 226 ing into an SV structure on the growing branch and back to an SD structure on the shrink-  
 227 ing branch, usually rotating to a magnetocrystalline hard direction close to  $d_{\min}$  on the  
 228 shrinking branch (Figure 1 iii). The rotation to a magnetocrystalline hard-aligned vor-  
 229 tex was occasionally preceded by a rotation to a magnetocrystalline intermediate axis,  
 230 particularly in TM55 and TM60 particles. SV states aligned with the magnetocrystalline  
 231 hard axis were found by Nagy et al. (2017) to have extremely low stability, which may  
 232 be of interest for paleomagnetists. Oblate particles behaved similarly for both ME-SE  
 233 and MH-SE anisotropies, nucleating a vortex along the short (shape hard) axis of the  
 234 particle (Figure 3e - f).

235 Different states were observed in prolate particles depending on elongation direc-  
 236 tion: In ME-SE particles, a vortex state aligned along the major axis continued to ex-  
 237 ist without changing up to the maximum size of 500 nm (Figure 3a ii) and continued un-

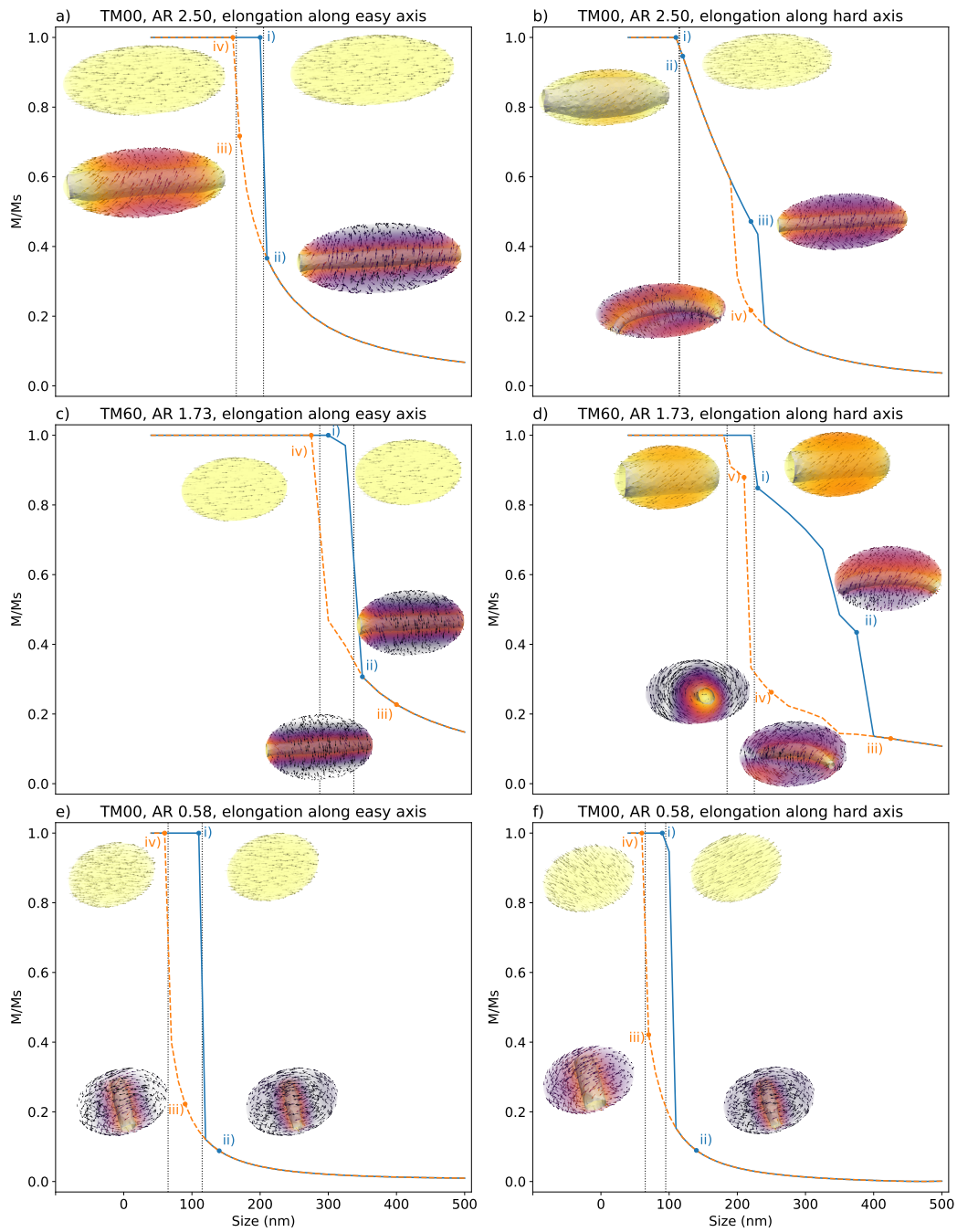


**Figure 3.** Example size hysteresis loop for particles elongated along the magnetocrystalline easy axis (left column) and for the same particles elongated along the magnetocrystalline hard axis (right column). a - b) size hysteresis loop for a prolate magnetite particle with an axial ratio of 2.50. c - d) size hysteresis loop for a prolate TM60 particle with an axial ratio of 1.73. e - f) size hysteresis loop for an oblate particle with an axial ratio of 0.58. In all plots, the numerals i), ii), iii), iv), v) denote the order in which the minimizations were performed, and the colours represent the growing (blue) or shrinking (orange) branch.  $d_{\min}$  and  $d_{\max}$  are plotted as vertical dotted lines.

238 changed down to  $d_{\min}$  (Figure 3a iii). By contrast, in MH-SE particles, a secondary sharp  
 239 drop in the magnetization was observed at sizes above  $d_{\max}$ , with the SV state along the  
 240 major axis (Figure 3b iii) transitioning to a state with a curved vortex core which had  
 241 its ends deflected away from the major axis (Figure 3b iv). These cores were deflected  
 242 in a variety of directions, forming “Banana” or “S” shapes depending on the whether the  
 243 two ends of the core were deflected in adjacent or opposing directions. The deflected vor-  
 244 tex structures persisted to lower sizes on the shrinking branch than on the growing branch,  
 245 leading to another “loop” on the size hysteresis diagrams. The transition at  $d_{\min}$  for MH-  
 246 SE particles was often more subtle than for ME-SE ones, with little change in energy,  
 247 and often a closed loop ( $d_{\min} = d_{\max}$ ) e.g. Fig 3b).

248 The “S” shaped vortices were frequently observed undergoing rotations during the  
 249 shrinking branch of the size hysteresis loop, with the core rotating to lie along one of the  
 250 short (shape-hard) axes of the particle, similar to the states observed in Nagy et al. (2022),  
 251 which were found to cause pTRM tails in paleointensity experiments. This behaviour  
 252 can be seen in Figure 3d ii-iv, and occurred most frequently in prolate particles with ax-  
 253 ial ratios between 1 and 2. This rotation to a short axis was occasionally observed in ME-  
 254 SE particles, but was far less prevalent overall.

### 255 3.3 Trends in $d_{\min}$ and $d_{\max}$

256 The critical domain transition sizes for  $d_{\min}$  and  $d_{\max}$  for each composition and shape  
 257 are presented as contour plots and surfaces in Figure 4. To obtain  $d_{\min}$  and  $d_{\max}$  as a  
 258 continuous function of TM composition and axial ratio, the extant data were interpo-  
 259 lated using a piecewise cubic 2D interpolation routine. White dashed contours with 100  
 260 nm spacing are used to highlight regions where  $d_{\max}$  was greater than 500 nm, where  
 261 a rapid increase occurs. Additionally, some regions of the  $d_{\min}$  and  $d_{\max}$  surfaces are miss-  
 262 ing from this dataset. This is because the SD state persists beyond 1  $\mu\text{m}$  during the grow-  
 263 ing branch of the size hysteresis loop. Obtaining  $d_{\min}$  and  $d_{\max}$  for loops above this size  
 264 becomes rapidly more computationally expensive

265 The surfaces displayed in Figure 4 exhibit some consistent trends with both size  
 266 and shape. Slices through these surfaces (represented by thick lines on Figure 4a, b and  
 267 d) at constant composition or axial ratio are displayed in Figure 5. The most noticeable  
 268 feature of the surfaces is that  $d_{\max}$  sharply increases for both prolate and oblate parti-  
 269 cles relative to equidimensional ones for all compositions (Figure 4a,c). By contrast  $d_{\min}$   
 270 tends to increase with increasing axial ratio across almost all shapes. The relationship  
 271 between  $d_{\max}$  and TM composition is more complicated. For equidimensional particles,  
 272  $d_{\max}$  appears to increase rapidly for compositions from TM00 - TM40, decrease from TM40  
 273 - TM50, followed by another increase to TM55 and a decrease to TM60. This broad trend  
 274 is observed for all other shapes where data are available.  $d_{\min}$  tends to increase relatively  
 275 uniformly with increasing TM composition.

276 The  $d_{\min}$  and  $d_{\max}$  surfaces for both the ME-SE and MH-SE particles are displayed  
 277 in Figure 6. It is apparent that the  $d_{\max}$  surface in Figure 4 is similar to the ME-SE sur-  
 278 face, except at the highest TM compositions. This is primarily driven by the reduced  
 279  $d_{\max}$  for prolate MH-SE particles, with many of the loops being closed (i.e.  $d_{\min} = d_{\max}$ ).  
 280 The anisotropy for MH-SE particles has a less uniaxial character, and so the SD struc-  
 281 ture cannot be a LEM state at larger sizes. The LEM states in the ME-SE particles change  
 282 rapidly from an SD structure to a vortex structure, accompanied by a sharp drop in the  
 283 net magnetization (Figure 3a i to ii) By contrast, the MH-SE particles change more grad-  
 284 ually from an SD to an SV structure (Figure 3b i to ii), with the first SV states having  
 285 wide vortex cores encompassing nearly the entire particle. There is also a reduction in  
 286  $d_{\max}$  for MH-SE oblate surfaces (Figure 3e - f), particularly at intermediate TM com-  
 287 positions.

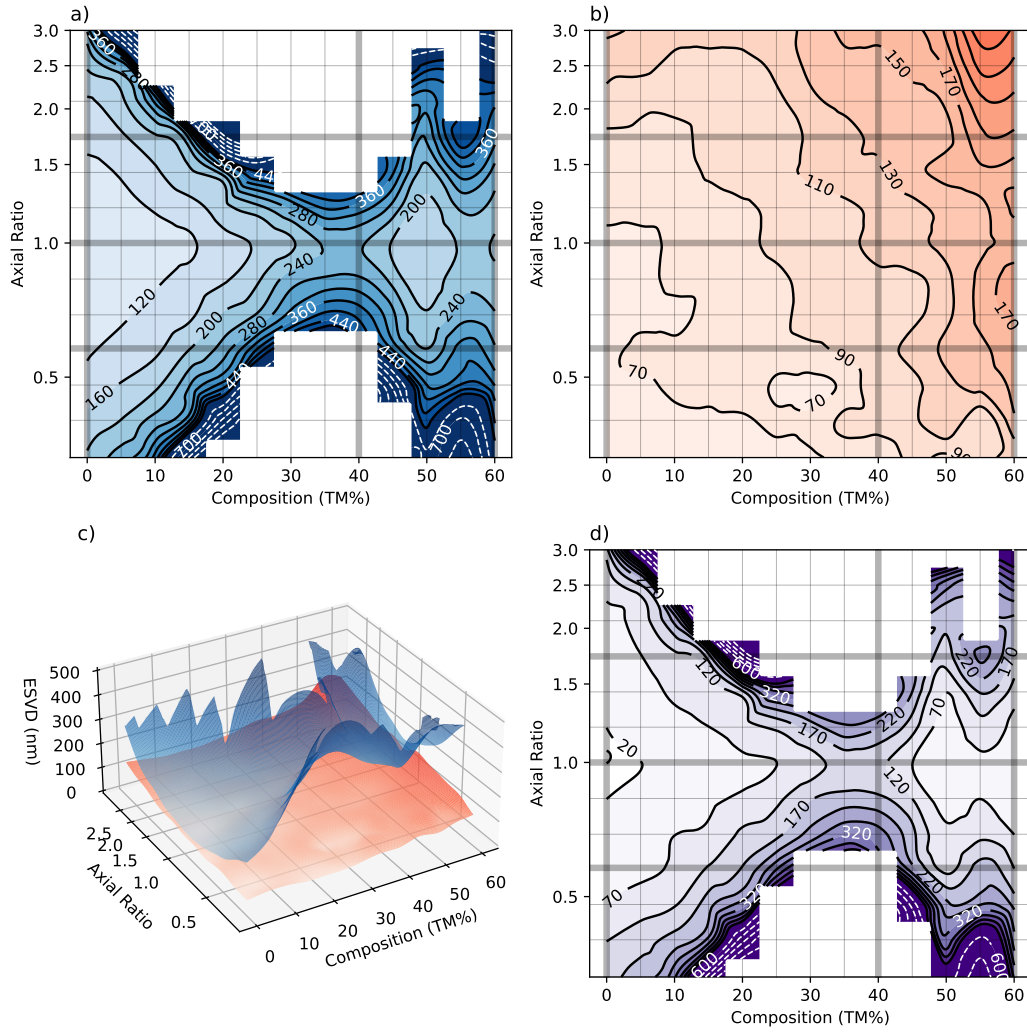


**Figure 4.** Plots of the maximum  $d_{max}$  and minimum  $d_{min}$  of the ME-SE and MH-SE anisotropies as a function of composition and shape. a) Contour plot of the maximum size at which the SD structure was observed on growing ( $d_{max}$ ). b) Contour plot of the minimum size at which the SV structure was observed when shrinking ( $d_{min}$ ). c) 3D surface plot of the  $d_{min}$  and  $d_{max}$  surfaces in a and b. d) Contour plot of the difference (in nm) between the surfaces shown in a, b and c. This represents the range of sizes where both the SD and SV structures are available to a particle of this composition and geometry. The surface and contour plots shown here are produced from a smoothed cubic spline surface fit to the data, with the original data located on the corners of the grid. Thicker grid lines show the locations of slices through the contour plot shown in Figure 5. White dashed contours represent wider spacings of 100 nm in regions where  $500 < d_{max} < 1000$  nm, where the models may be less precise. Note that for ease of viewing, the surface in c is truncated at 500 nm.  $d_{max}$  data are missing for particles that remained in the SD structure after growing to  $1 \mu\text{m}$ .

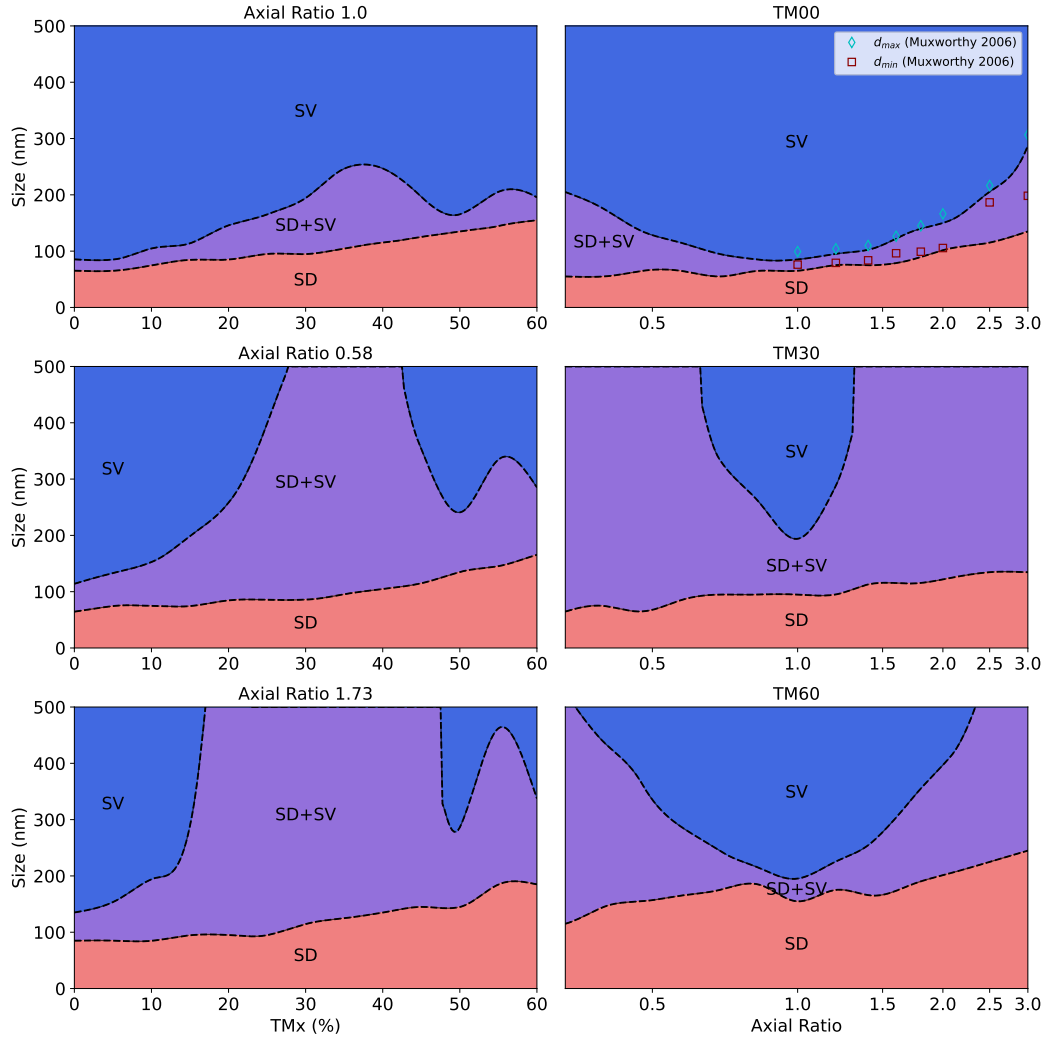


**Figure 5.** Slices through surfaces displayed in Figure 4. Blue represents regions above the upper surface where the SV structure (and other more complicated states) is available. Red represents the region in which the SD structure is available. Purple represents the range of sizes in which the SD and SV structures are both available. For the TM00 (magnetite) composition, the minimum  $d_{\min}$  and maximum  $d_{\max}$  of Muxworthy and Williams (2006) are plotted as red squares and blue diamonds for comparison.

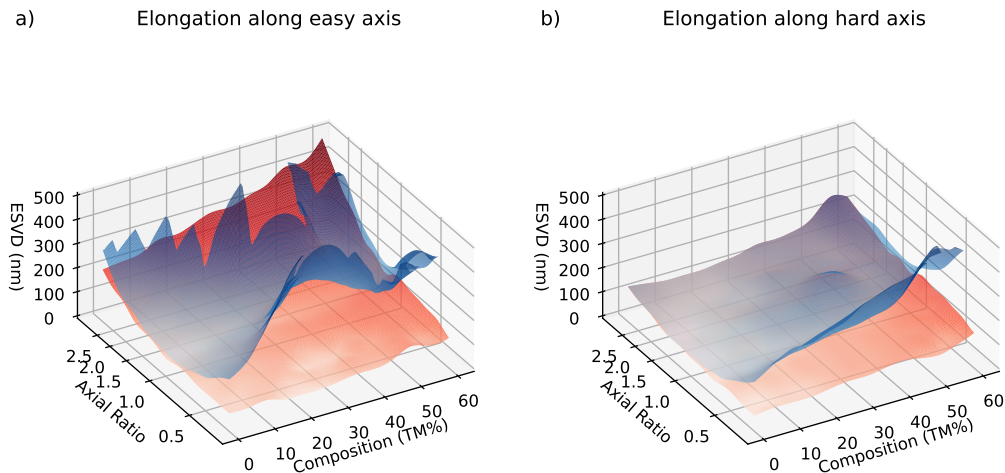


**Figure 6.** Critical size surfaces for ME-SE (left) vs MH-SE (right) particles. The presentation of these surfaces is the same as in Figure 4c.

## 288 4 Discussion

### 289 4.1 Comparison to other studies

290 Our results provide the first description of the domain states present in titanomag-  
 291 netites using modern micromagnetic models. Our maps of the size ranges of the SD and  
 292 SV structures follow the work of Butler and Banerjee (1975), but our results are based  
 293 on unconstrained, inhomogeneous 3-D models. This allows us to evaluate the true LEM  
 294 states not available from classic Kittel two-domain structure calculations. Additionally,  
 295 our titanomagnetite material parameters are empirically derived using far more data than  
 296 were available to Butler and Banerjee, and include the second magnetocrystalline anisotropy  
 297 constant  $k_2$ . This robust physical basis, combined with the increased scale and resolu-  
 298 tion of our models, enables us to make realistic predictions about the domain states of  
 299 remanence carriers in igneous rocks. This in turn enables us to identify carriers with po-  
 300 tential to cause problematic behaviors in paleomagnetic experiments.

301 The results presented in Section 3 are most quantitatively comparable to those of  
 302 Muxworthy and Williams (2006), who applied the size-hysteresis algorithm for prolate  
 303 magnetite parallelepipeds. We extend this approach to 12 additional compositions and  
 304 oblate geometries. Our results for  $d_{\min}$  and  $d_{\max}$  in magnetite are compared to theirs  
 305 (converted to ESVD) in Figure 5. The  $d_{\max}$  data follow a very similar trend with our  
 306  $d_{\max}$  values being slightly smaller for all elongations. The  $d_{\min}$  values are also mostly  
 307 consistent, but Muxworthy & Williams observe a large increase in  $d_{\min}$  at an axial ra-  
 308 tio of 2.5, which is not seen in our data. The general similarity between the trends in  
 309 both studies is encouraging, demonstrating the reproducibility of the size-hysteresis al-  
 310 gorithm.

311 The discrepancy between some of our  $d_{\min}$  values and those of Muxworthy and Williams  
 312 (2006) can be explained by numerous differences between our methodology and theirs;  
 313 The material parameters for magnetite used are slightly different, our domain states are  
 314 defined differently, Muxworthy & Williams used a micromagnetic method involving a fast  
 315 fourier transform rather than the finite element method currently used in MERRILL,  
 316 and our results are for ellipsoidal particles rather than parallelepipeds. Ellipsoids were

317 used because faceted surfaces affect the available domain states available to a particle,  
 318 an effect known as configurational anisotropy (see W. Williams et al., 2006 for a detailed  
 319 discussion). The ellipsoidal geometry minimizes the effect of configurational anisotropy  
 320 by minimizing the size of faceted surfaces, ensuring that the dominant controls on  $d_{\min}$   
 321 and  $d_{\max}$  are composition and axial ratio.

322 Usov and Serebryakova (2023) calculated the energies of different domain states  
 323 present in magnetite ellipsoids, using a different algorithm to that employed in MER-  
 324 RILL. They calculated a critical size, defined as the size at which the energy of the SV  
 325 structure was lower than that of the SD structure. These critical sizes lie between our  
 326  $d_{\min}$  and  $d_{\max}$  when converted to ESVD, which should be expected as our critical sizes  
 327 are bounds on the existence of the structures. The authors findings also shared three com-  
 328 mon features with ours; Firstly, differences between the size ranges of domain structures  
 329 in ME-SE and MH-SE particles. Secondly, SD and SV structures existing in overlapping  
 330 size ranges. Finally, SV states aligned with a variety of magnetocrystalline and shape  
 331 easy/hard directions. These similarities when using a different software, algorithm, and  
 332 material parameters suggest that these features are robust properties of titanomagnetites.

## 333 4.2 Domain states and instability

334 The range of sizes between  $d_{\min}$  and  $d_{\max}$ , where both the SD and SV structures  
 335 can exist, is largest for highly elongated or flattened particles and intermediate TM com-  
 336 positions. Within this range of sizes, the magnetocrystalline hard-aligned vortex observed  
 337 by Nagy et al. (2017) is observed in equidimensional particles, and the multiple avail-  
 338 able domain states could lead to non-ideal “pTRM tail” type behaviour in paleointen-  
 339 sity experiments. The “unstable zone” of Nagy et al. containing magnetocrystalline hard-  
 340 aligned vortices was only found to be  $\sim 10$  nm wide for equidimensional magnetite, but  
 341 we demonstrate that for other compositions and geometries, there are multiple available  
 342 domain states that can exist over many hundreds of nanometers.

343 A second region with multiple domain structures was observed in prolate MH-SE  
 344 particles at larger sizes than  $d_{\max}$  (e.g. Figure 3b, d). In this region, an SV state aligned  
 345 with the long (shape-easy) of the particle coexists with a state where the ends of the vor-  
 346 tex core are deflected away from this axis. The deflection is likely related to the influ-  
 347 ence of the magnetocrystalline easy axes, which could pull the core away from the shape-  
 348 easy direction towards one of a number of magnetocrystalline-easy directions. Upon fur-  
 349 ther shrinking, the vortex core rotated further and shape-hard aligned SV states were  
 350 frequently observed. The multiplicity of states offered by the different magnetocrystalline  
 351 and shape directions, and the wide range of sizes over which these states overlap with  
 352 the SV state suggest that there may be a second “unstable zone” in prolate MH-SE par-  
 353 ticles above  $d_{\max}$  and into the SV size range. Nagy et al. (2022) simulated pTRM tail  
 354 behaviour using a prolate faceted magnetite particle that did not have any single-domain  
 355 LEM states, supporting this hypothesis.

356 Without thermal energy barriers, size hysteresis experiments cannot calculate the  
 357 stability of individual particles, but the  $d_{\min}$  and  $d_{\max}$  sizes represent bounds on a re-  
 358 gion of interest, which should be a target for future micromagnetic studies. Energy bar-  
 359 rier calculations for particles in this region may further our understanding of the pTRM  
 360 tail phenomenon. Equidimensional particles near  $d_{\min}$  and prolate MH-SE particles should  
 361 be of particular interest to researchers studying this phenomenon, as they exhibit the  
 362 largest variety of states including the magnetocrystalline hard-aligned vortices of Nagy  
 363 et al. (2017) and the shape hard-aligned vortices of Nagy et al. (2022).

### 364 4.3 The effect of elongation direction

365 Overall, our findings indicate that the domain states available to magnetic parti-  
 366 cles have a dependence on the alignment of the magnetocrystalline and shape easy axes  
 367 (as seen in Figures 3 and 6). This effect has also been observed in micromagnetic algo-  
 368 rithms using magnetite cuboids by Muxworthy and Williams (2006) and recently in mag-  
 369 netite ellipsoids by Usov and Serebryakova (2023). Our results indicate that this effect  
 370 may be even more important than previously thought, as we observe domain states in  
 371 prolate titanomagnetites that are only present when the elongation direction is along a  
 372 shape hard axis, which may cause instability as multiple domain states exist in this re-  
 373 gion.

374 There have been few observations of the relationship between the elongation di-  
 375 rection and magnetization direction in natural samples. Feinberg et al. (2004) used the  
 376 Electron Back-Scatter Diffraction (EBSD) technique to make observations about the ori-  
 377 entations of prolate magnetite particles exsolved in clinopyroxene, and Ageeva et al. (2020)  
 378 used the same technique to investigate particles exsolved in plagioclase. Both found mag-  
 379 netite particles elongated along the  $\langle 111 \rangle$  (magnetocrystalline easy) and  $\langle 110 \rangle$  (in-  
 380 termediate) directions. By contrast, Li et al. (2020) recently found that bullet shaped  
 381 magnetite particles in chains of magnetosomes were predominantly elongated along the  
 382  $\langle 100 \rangle$  (hard) axis. These limited studies indicate that there is varying competition  
 383 between shape and magnetocrystalline axes in natural samples, with the dominant anisotropies  
 384 being strongly tied to the mechanism of particle growth. More EBSD observations of the  
 385 elongation directions in titanomagnetites of different origins will be necessary to constrain  
 386 the available domain states in a wider range of real samples.

## 387 5 Conclusions

388 We present a comprehensive set of results from micromagnetic models to determine  
 389 the range of possible domain states in ellipsoidal titanomagnetite particles of varying size,  
 390 shape and composition. Previous micromagnetic models characterizing the domain states  
 391 in samples have focused solely on equidimensional and prolate magnetite particles. The  
 392 range of compositions and shapes described in our study increase the number of exist-  
 393 ing domain state characterizations by more than an order of magnitude, improving our  
 394 understanding of a much wider range of remanence carriers.

395 For each titanomagnetite composition and geometry, we find the critical size at which  
 396 a single domain (SD) magnetization transitions to a single vortex (SV) magnetization  
 397 upon growing a particle ( $d_{\max}$ ) and the size at which an SV magnetization transitions  
 398 to an SD magnetization on shrinking the particle ( $d_{\min}$ ). Particles between these sizes  
 399 can be magnetized both in the single domain structure, and the single vortex structure.  
 400 This is significant, as for these particles we observe vortex structures aligned along the  
 401 magnetocrystalline hard axis, which were found to be unstable by Nagy et al. (2017).  
 402 Our results indicate that titanomagnetite particles of intermediate composition have a  
 403 larger range of sizes where both the SD and SV structures are available, and that this  
 404 range of sizes is larger for both oblate and prolate particles than for equidimensional ones.

405 Further, we find that the angle between the magnetocrystalline and shape easy axes  
 406 has a significant effect on the observed domain states in a particle. Prolate particles have  
 407 a much larger SD + SV size range when their elongation direction is along the magne-  
 408 tocrystalline easy axis (ME-SE) than when along the hard axis (MH-SE). MH-SE pro-  
 409 late particles exhibit “S” and “Banana” states in the SV size range, where the vortex core  
 410 of the magnetization is deflected away from the elongation direction. These states some-  
 411 times rotate to the particle’s short axis on shrinking, leading to a potential second “un-  
 412 stable zone” in titanomagnetites. Further investigation of the relationship between par-

413 ticle shape and crystallographic directions in natural samples should be undertaken to  
414 better understand this effect.

415 Overall, we show that the domain states available to grains vary as a function of  
416 shape and composition. The domain states observed indicate that the range of sizes, shapes  
417 and compositions of unstable remanence carriers that cause problematic behavior in pa-  
418 leomagnetic studies could be far larger than previously demonstrated. A prevalence of  
419 these carriers could explain the high failure rate of paleointensity experiments seen in  
420 paleomagnetic literature. Future work will focus on the unstable particles identified in  
421 this study to understand the effects of these instabilities on paleomagnetic experiments.

## 422 Open Research

423 The micromagnetic models were produced using the open source micromagnetic  
424 modeling MERRILL (Ó Conbhuí et al., 2018; W. Williams et al., n.d.), which is avail-  
425 able under a CC-BY-SA 4.0 International license at [https://bitbucket.org/wynwilliams/  
426 merrill/](https://bitbucket.org/wynwilliams/merrill/). A Zenodo repository containing a spreadsheet of results, as well as example  
427 scripts to reproduce this research can be found at [https://doi.org/10.5281/zenodo  
428 .10471806](https://doi.org/10.5281/zenodo.10471806) (Cych, 2024).

## 429 Acknowledgements

430 B.C. and G.A.P. acknowledge funding from Natural Environmental Research Coun-  
431 cil (NERC) grant NE/W006707/1. G.A.P. further acknowledges a NERC Independent  
432 Research Fellowship (NE/P017266/1). L.N. acknowledges funding from NERC Indepen-  
433 dent Research Fellowship NE/V014722/1. W.W. acknowledges NERC grants NE/S001018/1  
434 and NE/V001388/1. The Institute for Rock Magnetism (IRM) is a US National Multi-  
435 user Facility supported through the Instrumentation and Facilities program of the Na-  
436 tional Science Foundation, Earth Sciences Division, award NSF-EAR 2153786, and by  
437 funding from the University of Minnesota. This is IRM publication number 2401.

## 438 References

- 439 Ageeva, O., Bian, G., Habler, G., Pertsev, A., & Abart, R. (2020). Crystallographic  
440 and shape orientations of magnetite micro-inclusions in plagioclase. *Contrib.  
441 Mineral. Petrol.*, *175*(10), 1–16. doi: 10.1007/s00410-020-01735-8
- 442 Ahn, H.-S., Kidane, T., Yamamoto, Y., & Otofujii, Y.-i. (2016). Low geomagnetic  
443 field intensity in the matuyama chron: palaeomagnetic study of a lava se-  
444 quence from afar depression, east africa. *Geophysical Journal International*,  
445 *204*(1), 127–146.
- 446 Akimoto, S.-i., Katsura, T., & Yoshida, M. (1957). Magnetic properties of  $\text{TiFe}_2\text{O}_4$ -  
447  $\text{Fe}_3\text{O}_4$  system and their change with oxidation. *J. Geomagn. Geoelec.*, *9*(4),  
448 165–178. doi: 10.5636/jgg.9.165
- 449 Aragón, R. (1992). Cubic magnetic anisotropy of nonstoichiometric magnetite. *Phys-  
450 ical Review B*, *46*(9), 5334.
- 451 Ayachit, U. (2015). *The paraview guide: a parallel visualization application*. Kitware,  
452 Inc.
- 453 Banerjee, S. K. (1991). Magnetic properties of Fe-Ti oxides. In D. H. Lindsley (Ed.),  
454 *Oxide minerals: Petrologic and magnetic significance* (pp. 107–128). Berlin,  
455 Boston: De Gruyter. doi: 10.1515/9781501508684-007
- 456 Bickford, L., Brownlow, J., & Penoyer, R. (1957). Magnetocrystalline anisotropy  
457 in cobalt-substituted magnetite single crystals. *Proceedings of the IEE-Part B:  
458 Radio and Electronic Engineering*, *104*(5S), 238–244.
- 459 Bickford Jr, L. (1950). Ferromagnetic resonance absorption in magnetite single crys-  
460 tals. *Physical Review*, *78*(4), 449.

- 461 Bleil, U. (1976). An experimental study of the titanomagnetite solid solution series.  
462 *Pure and Applied geophysics*, *114*, 165–175.
- 463 Böhnell, H. N., Dekkers, M. J., Delgado-Argote, L. A., & Gratton, M. N. (2009).  
464 Comparison between the microwave and multispecimen parallel difference pTRM  
465 paleointensity methods. *Geophysical Journal International*, *177*(2), 383–394.
- 466 Bol'shakov, A. (1979). A thermomagnetic criterion for determining the domain  
467 structure of ferrimagnetics. *Izv. Acad. Sci. USSR Phys. Solid Earth*, *15*, 111–  
468 117.
- 469 Bowles, J. A., Gerzich, D. M., & Jackson, M. J. (2018). Assessing new and old  
470 methods in paleomagnetic paleothermometry: a test case at Mt. St. Helens,  
471 USA. *Geochemistry, Geophysics, Geosystems*, *19*(6), 1714–1730.
- 472 Bowles, J. A., Morris, A., Tivey, M., & Lascu, I. (2020). Magnetic mineral popula-  
473 tions in lower oceanic crustal gabbros (Atlantis bank, SW Indian ridge): Impli-  
474 cations for marine magnetic anomalies. *Geochemistry, Geophysics, Geosystems*,  
475 *21*(3), e2019GC008847.
- 476 Brown, W. F. B. (1963). *Micromagnetics*. New York: John Wiley & Sons.
- 477 Butler, R. F., & Banerjee, S. K. (1975). Theoretical single-domain grain size range  
478 in magnetite and titanomagnetite. *J. Geophys. Res.*, *80*(29), 4049–4058. doi:  
479 10.1029/JB080i029p04049
- 480 Calhoun, B. (1954). Magnetic and electric properties of magnetite at low tempera-  
481 tures. *Physical Review*, *94*(6), 1577.
- 482 Calvo, M., Prévot, M., Perrin, M., & Riisager, J. (2002). Investigating the reasons  
483 for the failure of palaeointensity experiments: a study on historical lava flows  
484 from Mt. Etna (Italy). *Geophysical journal international*, *149*(1), 44–63.
- 485 Calvo-Rathert, M., Bógalo, M. F., Gogichaishvili, A., Sologashvili, J., & Vashakidze,  
486 G. (2013). New paleomagnetic and paleointensity data from pliocene lava flows  
487 from the lesser caucasus. *Journal of Asian Earth Sciences*, *73*, 347–361.
- 488 Calvo-Rathert, M., Goguitchaichvili, A., Bógalo, M.-F., Vegas-Tubía, N., Carrancho,  
489 Á., & Sologashvili, J. (2011). A paleomagnetic and paleointensity study on  
490 pleistocene and pliocene basaltic flows from the djavakheti highland (southern  
491 georgia, caucasus). *Physics of the Earth and Planetary interiors*, *187*(3-4),  
492 212–224.
- 493 Calvo-Rathert, M., Goguitchaichvili, A., & Vegas-Tubia, N. (2009). A paleointensity  
494 study on middle miocene to pliocene volcanic rocks from south-eastern spain.  
495 *Earth, planets and space*, *61*, 61–69.
- 496 Carvallo, C., Camps, P., Ruffet, G., Henry, B., & Poidras, T. (2003). Mono lake  
497 or Laschamp geomagnetic event recorded from lava flows in Amsterdam is-  
498 land (southeastern Indian Ocean). *Geophysical Journal International*, *154*(3),  
499 767–782.
- 500 Carvallo, C., Özdemir, Ö., & Dunlop, D. J. (2004). Palaeointensity determina-  
501 tions, palaeodirections and magnetic properties of basalts from the Emperor  
502 seamounts. *Geophysical Journal International*, *156*(1), 29–38.
- 503 Chauvin, A., Gillot, P.-Y., & Bonhommet, N. (1991). Paleointensity of the Earth's  
504 magnetic field recorded by two late quaternary volcanic sequences at the island  
505 of La Réunion (Indian ocean). *Journal of Geophysical Research: Solid Earth*,  
506 *96*(B2), 1981–2006.
- 507 Chikazumi, S. (1964). *Physics of magnetism*. John Wiley & Sons.
- 508 Coe, R. S., Grommé, S., & Mankinen, E. A. (1978). Geomagnetic paleointensities  
509 from radiocarbon-dated lava flows on Hawaii and the question of the pacific  
510 nondipole low. *Journal of Geophysical Research: Solid Earth*, *83*(B4), 1740–  
511 1756.
- 512 Coe, R. S., Gromme, S., & Mankinen, E. A. (1984). Geomagnetic paleointensities  
513 from excursion sequences in lavas on Oahu, Hawaii. *Journal of Geophysical Re-  
514 search: Solid Earth*, *89*(B2), 1059–1069.
- 515 Coreform LLC. (2017). *Coreform Cubit, v2022.4 (64-Bit)*. Retrieved from <https://>

- 516 coreform.com
- 517 Cych, B. (2024). *Titanomagnetite size hysteresis*. Zenodo. Retrieved from  
 518 <https://doi.org/10.5281/zenodo.10471806> (Software) doi: 10.5281/  
 519 zenodo.10471806
- 520 de Groot, L. V., Dekkers, M. J., & Mullender, T. A. (2012). Exploring the potential  
 521 of acquisition curves of the anhysteretic remanent magnetization as a tool to  
 522 detect subtle magnetic alteration induced by heating. *Physics of the Earth and  
 523 Planetary Interiors*, *194*, 71–84.
- 524 de Groot, L. V., Mullender, T. A., & Dekkers, M. J. (2013). An evaluation of the  
 525 influence of the experimental cooling rate along with other thermomagnetic  
 526 effects to explain anomalously low palaeointensities obtained for historic lavas  
 527 of Mt Etna (Italy). *Geophysical Journal International*, *193*(3), 1198–1215.
- 528 Donadini, F., Elming, S.-Å., Tauxe, L., & Hålenius, U. (2011). Paleointensity de-  
 529 termination on a 1.786 ga old gabbro from Hoting, central Sweden. *Earth and  
 530 Planetary Science Letters*, *309*(3-4), 234–248.
- 531 Dunlop, D. J., & Özdemir, Ö. (2001). Beyond Néel’s theories: thermal demagne-  
 532 tization of narrow-band partial thermoremanent magnetizations. *Phys. Earth  
 533 Planet. Inter.*, *126*(1), 43–57. doi: 10.1016/S0031-9201(01)00243-6
- 534 Dunlop, D. J., & Özdemir, Ö. (1997). *Rock magnetism: fundamentals and frontiers*  
 535 (No. 3). Cambridge university press.
- 536 Fabian, K., Kirchner, A., Williams, W., Heider, F., Leibl, T., & Huber, A. (1996).  
 537 Three-dimensional micromagnetic calculations for magnetite using FFT. *Geo-  
 538 phys. J. Int.*, *124*(1), 89–104. doi: 10.1111/j.1365-246X.1996.tb06354.x
- 539 Feinberg, J. M., Harrison, R. J., Kasama, T., Dunin-Borkowski, R. E., Scott, G. R.,  
 540 & Renne, P. R. (2006). Effects of internal mineral structures on the magnetic  
 541 remanence of silicate-hosted titanomagnetite inclusions: An electron hologra-  
 542 phy study. *Journal of Geophysical Research: Solid Earth*, *111*(B12).
- 543 Feinberg, J. M., Wenk, H.-R., Renne, P. R., & Scott, G. R. (2004). Epitaxial  
 544 relationships of clinopyroxene-hosted magnetite determined using electron  
 545 backscatter diffraction (EBSD) technique. *Am. Mineral.*, *89*(2-3), 462–466.  
 546 doi: 10.2138/am-2004-2-328
- 547 Ferk, A., Aulock, F. v., Leonhardt, R., Hess, K.-U., & Dingwell, D. (2010). A  
 548 cooling rate bias in paleointensity determination from volcanic glass: An ex-  
 549 perimental demonstration. *Journal of Geophysical Research: Solid Earth*,  
 550 *115*(B8).
- 551 Ferk, A., Denton, J., Leonhardt, R., Tuffen, H., Koch, S., Hess, K.-U., & Dingwell,  
 552 D. (2012). Paleointensity on volcanic glass of varying hydration states. *Physics  
 553 of the Earth and Planetary Interiors*, *208*, 25–37.
- 554 Fletcher, E., & O’Reilly, W. (1974). Contribution of Fe<sup>2+</sup> ions to the magnetocrys-  
 555 talline anisotropy constant  $k_1$  of Fe<sub>3-x</sub>Ti<sub>x</sub>O<sub>4</sub> (0 < x < 1). *Journal of Physics  
 556 C: Solid State Physics*, *7*(1), 171.
- 557 Fontana, G., Mac Niocaill, C., Brown, R. J., Sparks, R. S. J., & Field, M. (2011).  
 558 Emplacement temperatures of pyroclastic and volcanoclastic deposits in kim-  
 559 berlite pipes in southern Africa. *Bulletin of Volcanology*, *73*, 1063–1083.
- 560 Fredkin, D., & Koehler, T. (1987). Numerical micromagnetics by the finite element  
 561 method. *IEEE Transactions on Magnetism*, *23*(5), 3385–3387.
- 562 Gonzalez, S., Sherwood, G., Böhnell, H., & Schnepf, E. (1997). Palaeosecular vari-  
 563 ation in central Mexico over the last 30000 years: the record from lavas. *Geo-  
 564 physical Journal International*, *130*(1), 201–219.
- 565 Hauptman, Z. (1974). High temperature oxidation, range of non-stoichiometry and  
 566 curie point variation of cation deficient titanomagnetite Fe<sub>2.4</sub>Ti<sub>0.6</sub>O<sub>4+γ</sub>. *Geo-  
 567 physical Journal International*, *38*(1), 29–47.
- 568 Heider, F., & Williams, W. (1988). Note on temperature dependence of exchange  
 569 constant in magnetite. *Geophysical Research Letters*, *15*(2), 184–187.
- 570 Hill, M. J., & Shaw, J. (1999). Palaeointensity results for historic lavas from Mt

- 571 Etna using microwave demagnetization/remagnetization in a modified Thellier-  
572 type experiment. *Geophysical Journal International*, 139(2), 583–590.
- 573 Hill, M. J., & Shaw, J. (2000). Magnetic field intensity study of the 1960 Kilauea  
574 lava flow, Hawaii, using the microwave palaeointensity technique. *Geophysical*  
575 *Journal International*, 142(2), 487–504.
- 576 Hunt, C. P., Moskowitz, B. M., & Banerjee, S. K. (1995). Magnetic properties of  
577 rocks and minerals. *Rock physics and phase relations: A handbook of physical*  
578 *constants*, 3, 189–204.
- 579 Kąkol, Z., Sabol, J., & Honig, J. (1991a). Cation distribution and magnetic proper-  
580 ties of titanomagnetites  $\text{Fe}_{3-x}\text{Ti}_x\text{O}_4$  ( $0 \leq x < 1$ ). *Physical Review B*, 43(1),  
581 649.
- 582 Kąkol, Z., Sabol, J., & Honig, J. (1991b). Magnetic anisotropy of titanomagnetites  
583  $\text{Fe}_{3-x}\text{Ti}_x\text{O}_4$  ( $0 \leq x < 0.55$ ). *Physical Review B*, 44(5), 2198.
- 584 Kąkol, Z., Sabol, J., Stickler, J., Kozłowski, A., & Honig, J. (1994). Influence of ti-  
585 tanium doping on the magnetocrystalline anisotropy of magnetite. *Physical Re-*  
586 *view B*, 49(18), 12767.
- 587 Keefer, C. M., & Shive, P. N. (1981). Curie temperature and lattice constant  
588 reference contours for synthetic titanomaghemites. *Journal of Geophysical*  
589 *Research: Solid Earth*, 86(B2), 987–998.
- 590 Khakhalova, E., Moskowitz, B. M., Williams, W., Biedermann, A. R., & Solheid,  
591 P. (2018). Magnetic vortex states in small octahedral particles of interme-  
592 diate titanomagnetite. *Geochem. Geophys. Geosyst.*, 19(9), 3071–3083. doi:  
593 10.1029/2018GC007723
- 594 Kittel, C. (1949). Physical theory of ferromagnetic domains. *Reviews of modern*  
595 *Physics*, 21(4), 541.
- 596 Kono, M. (1974). Intensities of the Earth’s magnetic field about 60 my ago deter-  
597 mined from the Deccan trap basalts, India. *Journal of Geophysical Research*,  
598 79(8), 1135–1141.
- 599 Kono, M., & Tosha, T. (1980). Geomagnetic paleointensity measurements on leg 55  
600 basalts. *Init. Repts. DSDP*, 753–758.
- 601 Larson, E., Ozima, M., Nagata, T., & Strangway, D. (1969). Stability of  
602 remanent magnetization of igneous rocks. *Geophysical Journal International*,  
603 17(3), 263–292.
- 604 Li, J., Menguy, N., Roberts, A. P., Gu, L., Leroy, E., Bourgon, J., . . . Pan, Y.  
605 (2020). Bullet-shaped magnetite biomineralization within a magnetotactic  
606 deltaproteobacterium: Implications for magnetofossil identification. *J. Geo-*  
607 *phys. Res. Biogeosci.*, 125(7), e2020JG005680. doi: 10.1029/2020JG005680
- 608 Mankinen, E. A. (1994). *Preliminary geomagnetic paleointensities from long valley*  
609 *caldera, california*. US Geological Survey.
- 610 Martín-Hernández, F., Bominaar-Silkens, I. M., Dekkers, M. J., & Maan, J. K.  
611 (2006). High-field cantilever magnetometry as a tool for the determination of  
612 the magnetocrystalline anisotropy of single crystals. *Tectonophysics*, 418(1-2),  
613 21–30.
- 614 Matzka, J., & Krása, D. (2007). Oceanic basalt continuous thermal demagnetization  
615 curves. *Geophysical Journal International*, 169(3), 941–950.
- 616 Michalk, D. M., Biggin, A. J., Knudsen, M. F., Böhnell, H. N., Nowaczyk, N. R.,  
617 Ownby, S., & López-Martínez, M. (2010). Application of the multispecimen  
618 palaeointensity method to pleistocene lava flows from the Trans-Mexican vol-  
619 canic belt. *Physics of the Earth and Planetary Interiors*, 179(3-4), 139–156.
- 620 Moskowitz, B. M. (1980). Theoretical grain size limits for single-domain, pseudo-  
621 single-domain and multi-domain behavior in titanomagnetite ( $x = 0.6$ ) as a  
622 function of low-temperature oxidation. *Earth Planet. Sci. Lett.*, 47(2), 285–  
623 293. doi: 10.1016/0012-821X(80)90045-X
- 624 Moskowitz, B. M. (1993). High-temperature magnetostriction of magnetite and ti-  
625 tanomagnetites. *Journal of Geophysical Research: Solid Earth*, 98(B1), 359–

- 371.
- 626  
627 Moskowitz, B. M., & Halgedahl, S. L. (1987). Theoretical temperature and grain-size  
628 dependence of domain state in  $x=0.6$  titanomagnetite. *Journal of Geophysical*  
629 *Research: Solid Earth*, *92*(B10), 10667–10682.
- 630 Moskowitz, B. M., Jackson, M., & Kissel, C. (1998). Low-temperature magnetic  
631 behavior of titanomagnetites. *Earth and Planetary Science Letters*, *157*(3-4),  
632 141–149.
- 633 Muxworthy, A. R., & Williams, W. (2006). Critical single-domain/multidomain  
634 grain sizes in noninteracting and interacting elongated magnetite particles:  
635 Implications for magnetosomes. *J. Geophys. Res. Solid Earth*, *111*(B12). doi:  
636 10.1029/2006JB004588
- 637 Muxworthy, A. R., & Williams, W. (2015). Critical single-domain grain sizes in  
638 elongated iron particles: implications for meteoritic and lunar magnetism. *Geo-*  
639 *phys. J. Int.*, *202*(1), 578–583. doi: 10.1093/gji/ggv180
- 640 Muxworthy, A. R., Williams, W., Roberts, A. P., Winklhofer, M., Chang, L., &  
641 Pósfai, M. (2013). Critical single domain grain sizes in chains of interacting  
642 greigite particles: Implications for magnetosome crystals. *Geochem. Geophys.*  
643 *Geosyst.*, *14*(12), 5430–5441. doi: 10.1002/2013GC004973
- 644 Nagy, L., Williams, W., Muxworthy, A. R., Fabian, K., Almeida, T. P., Conbhuí,  
645 P. Ó., & Shcherbakov, V. P. (2017). Stability of equidimensional  
646 pseudo-single-domain magnetite over billion-year timescales. *Proc. Natl.*  
647 *Acad. Sci. U.S.A.*, *114*(39), 10356–10360. doi: 10.1073/pnas.1708344114
- 648 Nagy, L., Williams, W., Tauxe, L., & Muxworthy, A. (2022). Chasing tails: In-  
649 sights from micromagnetic modeling for thermomagnetic recording in non-  
650 uniform magnetic structures. *Geophys. Res. Lett.*, *49*(23), e2022GL101032.  
651 doi: 10.1029/2022GL101032
- 652 Nagy, L., Williams, W., Tauxe, L., & Muxworthy, A. R. (2019). From nano to  
653 micro: Evolution of magnetic domain structures in multidomain magnetite.  
654 *Geochem. Geophys. Geosyst.*, *20*(6), 2907–2918. doi: 10.1029/2019GC008319
- 655 Néel, L. (1949). Théorie du traînage magnétique des ferromagnétiques en grains fins  
656 avec application aux terres cuites. *Annales de géophysique*, *5*, 99–136.
- 657 Newell, A. J., Dunlop, D. J., & Enkin, R. J. (1990). Temperature dependence  
658 of critical sizes, wall widths and moments in two-domain magnetite grains.  
659 *Physics of the earth and planetary interiors*, *65*(1-2), 165–176.
- 660 Nishitani, T., & Kono, M. (1983). Curie temperature and lattice constant of oxi-  
661 dized titanomagnetite. *Geophysical Journal International*, *74*(2), 585–600.
- 662 Ó Conbhuí, P. Ó., Williams, W., Fabian, K., Ridley, P., Nagy, L., & Muxworthy,  
663 A. R. (2018). MERRILL: Micromagnetic Earth Related Robust Interpreted  
664 Language Laboratory. *Geochem. Geophys. Geosyst.*, *19*(4), 1080–1106. doi:  
665 10.1002/2017GC007279
- 666 O'Donovan, J., & O'Reilly, W. (1977). The preparation, characterization and mag-  
667 netic properties of synthetic analogues of some carriers of the palaeomagnetic  
668 record. *Journal of geomagnetism and geoelectricity*, *29*(4), 331–344.
- 669 Özdemir, Ö., & O'Reilly, W. (1978). Magnetic properties of monodomain  
670 aluminium-substituted titanomagnetite. *Physics of the Earth and Planetary*  
671 *Interiors*, *16*(3), 190–195.
- 672 Ozima, M., & Larson, E. (1970). Low-and high-temperature oxidation of titano-  
673 magnetite in relation to irreversible changes in the magnetic properties of  
674 submarine basalts. *Journal of Geophysical Research*, *75*(5), 1003–1017.
- 675 Ozima, M., Ozima, M., & Kaneoka, I. (1968). Potassium-argon ages and magnetic  
676 properties of some dredged submarine basalts and their geophysical implica-  
677 tions. *Journal of Geophysical Research*, *73*(2), 711–723.
- 678 Ozima, M., & Sakamoto, N. (1971). Magnetic properties of synthesized ti-  
679 tanomaghemite. *Journal of Geophysical Research*, *76*(29), 7035–7046.
- 680 Pan, Y., Hill, M. J., & Zhu, R. (2005). Paleomagnetic and paleointensity study of

- 681 an oligocene–miocene lava sequence from the Hannuoba basalts in northern  
682 China. *Physics of the Earth and Planetary Interiors*, 151(1-2), 21–35.
- 683 Paterson, G. A., Roberts, A. P., Mac Niocaill, C., Muxworthy, A. R., Gurioli, L.,  
684 Viramonté, J. G., ... Weider, S. (2010). Paleomagnetic determination of  
685 emplacement temperatures of pyroclastic deposits: an under-utilized tool.  
686 *Bulletin of Volcanology*, 72, 309–330.
- 687 Pauthenet, R., & Bochirol, L. (1951). Aimantation spontanée des ferrites. *J. phys.*  
688 *radium*, 12(3), 249–251.
- 689 Piper, J., Koçbulut, F., Gürsoy, H., Tatar, O., Viereck, L., Lepetit, P., ... Akpınar,  
690 Z. (2013). Palaeomagnetism of the Cappadocian volcanic succession, central  
691 Turkey: Major ignimbrite emplacement during two short (Miocene) episodes  
692 and Neogene tectonics of the Anatolian collage. *Journal of Volcanology and*  
693 *Geothermal Research*, 262, 47–67.
- 694 Rahman, A., & Parry, L. (1978). Titanomagnetites prepared at different oxidation  
695 conditions: hysteresis properties. *Physics of the Earth and Planetary Interiors*,  
696 16(3), 232–239.
- 697 Rave, W., Fabian, K., & Hubert, A. (1998). Magnetic states of small cubic parti-  
698 cles with uniaxial anisotropy. *Journal of Magnetism and Magnetic Materials*,  
699 190(3), 332–348. doi: Doi10.1016/S0304-8853(98)00328-X
- 700 Readman, P., & O'Reilly, W. (1972). Magnetic properties of oxidized (cation-  
701 deficient) titanomagnetites (Fe, Ti, □)<sub>3</sub> O<sub>4</sub>. *Journal of geomagnetism and*  
702 *geolectricity*, 24(1), 69–90.
- 703 Riisager, P., & Riisager, J. (2001). Detecting multidomain magnetic grains in Thel-  
704 lier palaeointensity experiments. *Physics of the Earth and Planetary Interiors*,  
705 125(1), 111–117. doi: [https://doi.org/10.1016/S0031-9201\(01\)00236-9](https://doi.org/10.1016/S0031-9201(01)00236-9)
- 706 Robins, B. W. (1972). *Remanent magnetization in spinel iron-oxides* (Unpublished  
707 doctoral dissertation). UNSW Sydney.
- 708 Rolph, T. (1997). An investigation of the magnetic variation within two recent lava  
709 flows. *Geophysical Journal International*, 130(1), 125–136.
- 710 Sahu, S., & Moskowitz, B. M. (1995). Thermal dependence of magnetocrystalline  
711 anisotropy and magnetostriction constants of single crystal Fe<sub>2.4</sub>Ti<sub>0.6</sub>O<sub>4</sub>. *Geo-*  
712 *physical research letters*, 22(4), 449–452.
- 713 Santos, C. N., & Tauxe, L. (2019). Investigating the accuracy, precision, and  
714 cooling rate dependence of laboratory-acquired thermal remanences during  
715 paleointensity experiments. *Geochem. Geophys. Geosyst.*, 20(1), 383–397. doi:  
716 10.1029/2018GC007946
- 717 Schabes, M. E., & Bertram, H. N. (1988). Magnetization processes in ferromagnetic  
718 cubes. *Journal of Applied Physics*, 64(3), 1347–1357.
- 719 Selkin, P. A., Gee, J. S., Meurer, W. P., & Hemming, S. R. (2008). Paleointen-  
720 sity record from the 2.7 Ga Stillwater Complex, Montana. *Geochem. Geophys.*  
721 *Geosyst.*, 9(12). doi: 10.1029/2008GC001950
- 722 Sherwood, G., Shaw, J., Baer, G., & Mallik, S. B. (1993). The strength of the ge-  
723 omagnetic field during the cretaceous quiet zone: palaeointensity results from  
724 Israeli and Indian lavas. *Journal of geomagnetism and geolectricity*, 45(4),  
725 339–360.
- 726 Syono, Y. (1965). Magnetocrystalline anisotropy and magnetostriction of Fe<sub>3</sub>O<sub>4</sub>-  
727 Fe<sub>2</sub>TiO<sub>4</sub> series-with special application to rocks magnetism. *Jpn. J. Geophys.*,  
728 4, 71–143.
- 729 Syono, Y., & Ishikawa, Y. (1963). Magnetostriction constants of xFe<sub>2</sub>TiO<sub>4</sub> · (1 -  
730 x)Fe<sub>3</sub>O<sub>4</sub>. *Journal of the Physical Society of Japan*, 18(8), 1231–1232.
- 731 Tanaka, H., & Komuro, N. (2009). The Shaw paleointensity method: Can the ARM  
732 simulate the TRM alteration? *Physics of the Earth and Planetary Interiors*,  
733 173(3-4), 269–278.
- 734 Thellier, E. (1941). Sur les propriétés de l'aimantation thermorémanente des terres  
735 cuites. *CR Acad. Sci. Paris*, 213, 1019–1022.

- 736 Thellier, E., & Thellier, O. (1941). Sur les variations thermiques de l'aimantation  
737 thermorémanente des terres cuites. *CR Hebd. Seances Acad. Sci*, 213, 59–61.
- 738 Tsunakawa, H., & Shaw, J. (1994). The Shaw method of palaeointensity determina-  
739 tions and its application to recent volcanic rocks. *Geophysical Journal Interna-*  
740 *tional*, 118(3), 781–787.
- 741 Usov, N. A., & Serebryakova, O. N. (2023). Non uniform micromagnetic states in  
742 spheroidal magnetite nanoparticles. *J. Magn. Magn. Mater.*, 588, 171345. doi:  
743 10.1016/j.jmmm.2023.171345
- 744 Uyeda, S. (1958). Thermo-remanent magnetism as a medium of paleomagnetism,  
745 with special reference to reverse thermo-remanent magnetism. *J. Japan Geo-*  
746 *phys.*, 2, 1–123.
- 747 Valdez-Grijalva, M. A., Nagy, L., Muxworthy, A. R., Williams, W., & Fabian, K.  
748 (2018). The magnetic structure and palaeomagnetic recording fidelity of sub-  
749 micron greigite (Fe<sub>3</sub>S<sub>4</sub>). *Earth and Planetary Science Letters*, 483, 76–89.
- 750 V erard, C., Leonhardt, R., Winklhofer, M., & Fabian, K. (2012). Variations of  
751 magnetic properties in thin lava flow profiles: Implications for the recording of  
752 the Laschamp excursion. *Physics of the Earth and Planetary Interiors*, 200,  
753 10–27.
- 754 Villasante-Marcos, V., & Pav on-Carrasco, F. J. (2014). Palaeomagnetic constraints  
755 on the age of lomo negro volcanic eruption (el hierro, canary islands). *Geo-*  
756 *physical Journal International*, 199(3), 1497–1514.
- 757 Virtanen, P., Gommers, R., Oliphant, T. E., Haberland, M., Reddy, T., Courn-  
758 peau, D., . . . SciPy 1.0 Contributors (2020). SciPy 1.0: Fundamental algo-  
759 rithms for scientific computing in Python. *Nature Methods*, 17, 261–272. doi:  
760 10.1038/s41592-019-0686-2
- 761 Wanamaker, B., & Moskowitz, B. M. (1994). Effect of nonstoichiometry on the  
762 magnetic and electrical properties of synthetic single crystal Fe<sub>2.4</sub>Ti<sub>0.6</sub>O<sub>4</sub>. *Geo-*  
763 *physical Research Letters*, 21(11), 983–986.
- 764 Wang, D., & Van der Voo, R. (2004). The hysteresis properties of multidomain mag-  
765 netite and titanomagnetite/titanomaghemite in mid-ocean ridge basalts. *Earth*  
766 *and Planetary Science Letters*, 220(1-2), 175–184.
- 767 Wechsler, B. A., Lindsley, D. H., & Prewitt, C. T. (1984). Crystal structure and  
768 cation distribution in titanomagnetites (Fe<sub>3-x</sub>Ti<sub>x</sub>O<sub>4</sub>). *American Mineralogist*,  
769 69(7-8), 754–770.
- 770 Williams, H., & Bozorth, R. (1953). Magnetic study of low temperature transforma-  
771 tion in magnetite. *Reviews of Modern Physics*, 25(1), 79.
- 772 Williams, W., & Dunlop, D. J. (1989). Three-dimensional micromagnetic modelling  
773 of ferromagnetic domain structure. *Nature*, 337(6208), 634–637.
- 774 Williams, W., Fabian, K., P., R., Nagy, L., Paterson, G. A., & Muxworthy, A. R.  
775 (n.d.). *Merrill* [software]. Retrieved from <https://bitbucket.org/wynwilliams/merrill>
- 776
- 777 Williams, W., Muxworthy, A. R., & Paterson, G. A. (2006). Configurational  
778 anisotropy in single-domain and pseudosingle-domain grains of magnetite.  
779 *Journal of Geophysical Research: Solid Earth*, 111(B12).
- 780 Witt, A., Fabian, K., & Bleil, U. (2005). Three-dimensional micromagnetic calcu-  
781 lations for naturally shaped magnetite: Octahedra and magnetosomes. *Earth*  
782 *Planet. Sci. Lett.*, 233(3), 311–324. doi: 10.1016/j.epsl.2005.01.043

1

# Magnetic Domain States and Critical Sizes in the Titanomagnetite Series

2

3

**Brendan Cych<sup>1</sup>, Greig A. Paterson<sup>1</sup>, Lesleis Nagy<sup>1</sup>, Wyn Williams<sup>2</sup>, Bruce  
Moskowitz<sup>3</sup>**

4

5

<sup>1</sup>Department of Earth, Ocean and Environmental Sciences, University of Liverpool, Liverpool, L69 7ZE,  
UK

6

7

<sup>2</sup>School of GeoSciences, University of Edinburgh, Grant Institute, West Mains Road, Edinburgh, EH9  
3JW, UK

8

9

<sup>3</sup>Institute for Rock Magnetism, Department of Earth and Environmental Sciences, University of  
Minnesota, 150 John T. Tate Hall, 116 Church St. SE, Minneapolis, MN 55455U, USA

10

11

## **Key Points:**

12

13

14

15

16

17

- We systematically map out the domain states in titanomagnetite as a function of shape and composition.
- Our results highlight ranges of compositions, shapes and sizes which contain unreliable paleomagnetic recorders.
- For certain shapes and compositions, these regions span hundreds of nanometers, representing a significant proportion of remanence carriers.

**Abstract**

The minerals carrying the magnetic remanence in geological samples are commonly a solid solution series of iron-titanium spinels known as titanomagnetites. Despite the range of possible compositions within this series, micromagnetic studies that characterize the magnetic domain structures present in these minerals have typically focused on magnetite. No studies systematically comparing the domain-states present in titanomagnetites have been undertaken since the discovery of the single vortex (SV) structure and the advent of modern micromagnetism. The magnetic properties of the titanomagnetite series are known to vary strongly with composition, which may influence the domain states present in these minerals, and therefore the magnetic stability of the samples bearing them.

We present results from micromagnetic simulations of titanomagnetite ellipsoids of varying shape and composition to find the size ranges of the single domain (SD) and SV structures. These size ranges overlap, allowing for regions where the SD and SV structures are both available. These regions are of interest as they may lead to magnetic instability and “pTRM tails” in paleointensity experiments. We find that although this SD+SV zone occupies a narrow range of sizes for equidimensional magnetite, it is widest for intermediate (TM30-40) titanomagnetite compositions, and increases for both oblate and prolate particles, with some compositions and sizes having an SD+SV zone up to 100s of nm wide. Our results help to explain the prevalence of pTRM tail-like behavior in paleointensity experiments. They also highlight regions of particles with unusual domain states to target for further investigation into the definitive mechanism behind paleointensity failure.

**Plain Language Summary**

Rocks that record Earth’s magnetic field often contain the mineral magnetite. The crystal structure of magnetite allows titanium atoms to substitute for iron, giving rise to a range of minerals known as titanomagnetites. The internal magnetic structure of titanomagnetite particles in rocks, known as the “domain structure”, controls the ability of that particle to record magnetic fields. Particles with certain kinds of domain structure are unstable magnetic recorders, which can cause problems for experiments trying to determine Earth’s magnetic field strength in the past (paleointensity experiments). Although the domain structures in magnetite are well understood, there are no recent studies which describe them in titanomagnetites.

In this paper, we simulate the domain structures in small titanomagnetite particles and map these out as a function of size, shape and chemical composition. In doing so, we identify types of magnetic particles with multiple possible domain structures that may give rise to unstable magnetizations. Our results indicate that some titanomagnetite particles may have unstable magnetizations over a much larger range of sizes than has previously been seen in magnetite. This wide range of sizes could explain the high failure rates of paleointensity experiments.

**1 Introduction**

Magnetite is one of the most important magnetic minerals in igneous and sedimentary rocks, commonly forming during the crystallization of basaltic magmas, and in sediments through erosional and biogenic processes. Stoichiometrically pure magnetite ( $\text{Fe}_3\text{O}_4$ ) is a well studied magnetic mineral, but in nature it forms a solid solution series with titanium rich ulvospinel ( $\text{Fe}_2\text{TiO}_4$ ). Titanomagnetite compositions within the series  $\text{Fe}_{3-x}\text{Ti}_x\text{O}_4$  ( $0 \leq x \leq 1$ ) are represented using the notation  $\text{TM}x$  (e.g.  $x = 0.6$  is  $\text{TM}60$ ). Fundamental magnetic properties of the titanomagnetites, including the Curie temperature (Nishitani & Kono, 1983), saturation magnetization (Bleil, 1976) and magnetocrystalline anisotropy constants (Kakol et al., 1994), have been observed to vary across the solid solution se-

67 ries. The distribution of Curie temperatures in igneous rocks compiled from a compi-  
68 lation of 38 papers indicate that approximately 75% of paleomagnetic samples do not  
69 contain pure magnetite (see supplementary information for detailed references). Instead,  
70 they suggest that compositions from TM0 to TM60 are prevalent along with other min-  
71 erals. Despite this wide range of compositions and behaviours in nature, the rock mag-  
72 netic properties of titanomagnetites and their influences on paleomagnetic experiments  
73 are understudied.

74 Rocks containing titanomagnetites are used to determine Earth’s magnetic field strength  
75 and direction in the distant past. This information has many practical applications in  
76 the geosciences, from detecting the age of archeological samples, to determining the mo-  
77 tion of tectonic plates and the nucleation age of Earth’s inner core. The fundamental physics  
78 that explain how a rock can record a thermal remanent magnetization (TRM) by cool-  
79 ing in a field was first described by Louis Néel (Néel, 1949). This work assumes that the  
80 magnetic particles contained within rocks are uniformly magnetized in a structure known  
81 as “single-domain” (hereafter referred to as SD). Unfortunately, the SD structure is only  
82 energetically efficient over a small range of particle sizes, and the majority of the mag-  
83 netization in natural materials is carried by particles in other states, as we show below.  
84 Consequently, paleomagnetic experiments often produce results that are complicated and  
85 difficult to interpret. A better understanding of the domain states present in magnetic  
86 materials is necessary to understand this behavior, and to ensure that paleomagnetists  
87 can obtain accurate results.

88 To determine the dominant domain states of a magnetic particle, researchers use  
89 the micromagnetic modelling approach of Brown (1963). This technique was adapted  
90 by Fredkin and Koehler (1987) into a computational finite-element based technique, which  
91 finds stable magnetization states that minimize the energy of the particle. Some of the  
92 earliest findings from this approach demonstrated that magnetite particles sized approx-  
93 imately 100 nm - 1  $\mu$ m have magnetizations which curl in a “vortex” shape around a uni-  
94 form core, known as the Single Vortex (SV) structure (Schabes & Bertram, 1988; W. Williams  
95 & Dunlop, 1989).

96 Recent work has shown that there is an “unstable zone” (where particle relaxation  
97 times drop precipitously) in equidimensional magnetite particles at the lower size limit  
98 of the SV structure. In this region, the dominant domain state is a single vortex with  
99 the vortex core aligned along a magnetocrystalline hard axis direction . The energy needed  
100 to escape this state is small, and so it is not stable over geological timescales. Nagy et  
101 al. (2022) additionally showed that competition between shape easy- and hard-aligned  
102 SV states in magnetite can produce complicated “partial TRM (pTRM) tail” behaviour  
103 similar to that frequently seen in paleointensity experiments (e.g. Bol’Shakov, 1979; Dun-  
104 lop & Özdemir, 2001; Riisager & Riisager, 2001; Santos & Tauxe, 2019).

105 Several studies have focused on determining the range of sizes and shapes over which  
106 domain states are stable in metallic iron (Muxworthy & Williams, 2015), magnetite (Muxworthy  
107 & Williams, 2006; Nagy et al., 2019), and greigite (Muxworthy et al., 2013; Valdez-Grijalva  
108 et al., 2018). Despite the range of titanomagnetite compositions prevalent in nature, there  
109 has been little work published on domain states in titanomagnetites since Butler and Baner-  
110 jee (1975). That study showed that the size range over which the SD structure was stable  
111 varied as a function of TM composition. Moskowitz (1980) and Moskowitz and Halgedahl  
112 (1987) followed this work, calculating this size range for TM60 as a function of oxida-  
113 tion, temperature and stress. These two studies were undertaken before the discovery  
114 of the SV structure, instead considering a transition between a single domain and the  
115 two-domain structure of Kittel (1949). Muxworthy and Williams (2006) used micromag-  
116 netic modelling to determine the range of sizes for which the SD and SV structures were  
117 available in elongated magnetite cuboids. This range of sizes differed significantly from  
118 that of Butler and Banerjee (1975), but a modern micromagnetic approach was not ap-  
119 plied to other TM compositions. Khakhalova et al. (2018) simulated single and multi-

120 vortex states in a large pyramidal TM54 particle, but did not explore the variation in  
121 domain state with the size and shape of particles.

122 In this paper, we present results from a series of micromagnetic models using the  
123 Micromagnetic Earth Related Robust Interpreted Language Laboratory (MERRILL; Ó  
124 Conbhuí et al., 2018) software package, v1.8.6p. Each simulation determines the range  
125 of possible sizes over which the single domain and single vortex structures can exist us-  
126 ing a “size hysteresis” algorithm (e.g. Witt et al., 2005; Muxworthy & Williams, 2006,  
127 2015; Nagy et al., 2019) where a minimum energy state is calculated in a titanomagnetite  
128 particle whilst progressively varying its size (described fully in Section 2.1). We perform  
129 these simulations for ellipsoidal titanomagnetite particles of varying composition and ax-  
130 ial ratio, from oblate to prolate. Our results, which are presented in Section 3 give the  
131 size ranges for the SD and SV structures for a range of TM compositions and prolate  
132 and oblate particles. This expands on the existing results of Muxworthy and Williams  
133 (2006) for prolate magnetites by more than an order of magnitude. We discuss the im-  
134 plications of these results, as well as the potential impact on paleomagnetic experiments  
135 in Section 4.

## 136 2 Methodology

### 137 2.1 The size hysteresis algorithm

138 For each geometry and titanomagnetite composition in this paper, we use a “size  
139 hysteresis” algorithm. A graphical example for a sphere of TM25 is shown in Figure 1.  
140 The algorithm works as follows:

- 141 1. For a 40 nm particle of a particular titanomagnetite composition and geometry,  
142 start with a uniform magnetization aligned along one of the magnetocrystalline  
143 easy axes in zero external field. An energy minimization is performed using MER-  
144 RILL on this particle, producing a magnetization that is a local energy minimum  
145 (LEM) state.
- 146 2. The magnetization is taken and scaled up to a particle of a slightly larger size. An  
147 energy minimization is then performed on the new particle size. We define our size  
148 using the diameter of a sphere with equivalent volume (referred to as ESVD; equiv-  
149 alent spherical volume diameter). We increase the particle size by 10 nm when the  
150 ESVD is between 40 and 250 nm, and steps of 25 nm are used from 250 to 500  
151 nm.
- 152 3. For a certain size range, the particle will remain in the SD structure (Figure 1 i.),  
153 but at some critical size, the SD structure stops being energetically favorable, and  
154 the domain state collapses to the SV structure (Figure 1 ii.). We call the diam-  
155 eter associated this size  $d_{\max}$ , which is defined as being the center point between  
156 the SD and SV structures (e.g. between Figure 1 i. and ii.).
- 157 4. We continue this process of scaling the magnetization onto particles of progres-  
158 sively larger sizes and minimizing the energy, repeating up to a size of 500 nm.
- 159 5. After reaching 500 nm, we reverse the process, mapping the magnetization onto  
160 progressively smaller particles and minimizing the energy. At some point, (between  
161 Figure 1 iii. and iv.), the particle transitions from the SV structure to the SD struc-  
162 ture. We call this size  $d_{\min}$ , which may differ from  $d_{\max}$ .

163 As can be seen from Figure 1, the critical sizes for transitioning between the SD  
164 and SV structures and vice-versa are not the same, with  $d_{\max}$  occurring at a larger size  
165 (165 nm) than  $d_{\min}$  (105 nm). During the “shrinking” branch of the magnetization, we  
166 observe a hard-aligned vortex (Figure 1 iii.). The region between  $d_{\min}$  and  $d_{\max}$  is there-  
167 fore of interest as it may contain the “unstable zone” of Nagy et al. (2017).

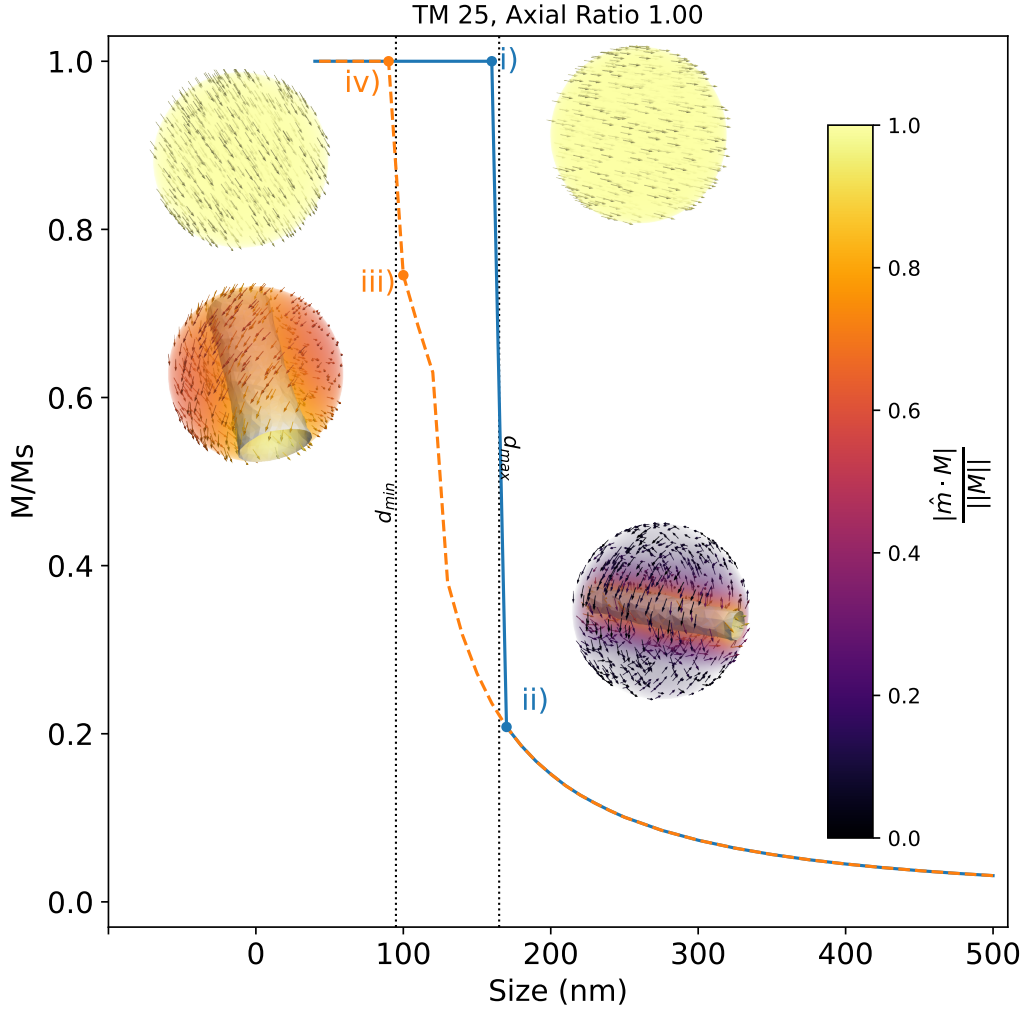


**Figure 1.** Ratio of the magnetization over the saturation magnetization ( $M/M_s$ ) plotted against EVSD (nm) in a “size hysteresis loop” for a sphere of TM25. The blue solid line represents the magnetization as the particle is grown from 40 from 500 nm, and the orange dashed line represents the magnetization as it is shrunk from 500 nm to 40 nm. Example magnetization states from the loop are shown at points i - iv). Vectors represent the direction of the magnetization at that location in the particle. Grey cylinder in ii) and iii) represents an isosurface where the relative helicity ( $h_{rel}$ , described in the supplemental information) is 0.95. Colors represent the absolute value of the dot product of these vectors with the direction of the net magnetization, with lighter yellow regions being aligned with the net magnetization, and darker purple regions being perpendicular. The magnetization transitions from the SD to the vortex state between i) and ii) (160-170 nm) and the magnitude of the magnetization continues to be reduced up to 500 nm due to the tightening of the vortex core. The vortex rotates to a magnetocrystalline hard axis direction between ii) and iii) and transitions back into a single domain state between iii) and iv) (100-90 nm) along a different easy direction.  $d_{min}$  and  $d_{max}$  are plotted as vertical lines.

168

## 2.2 Compositions and geometries

169

170

171

172

173

174

175

176

In this study, we will test the effects of titanomagnetite composition as well as shape on  $d_{\max}$  and  $d_{\min}$ . To produce a micromagnetic model using a particular material, fundamental material parameters are needed: the Curie temperature  $T_c$ , saturation magnetization  $M_s$ , exchange constant  $A_{\text{ex}}$  and magnetocrystalline anisotropy constants  $k_1$  and  $k_2$ . An extensive set of experimental data from previous work was compiled. Polynomial fits to these data were used to obtain functions that can return the material parameters for a given TM composition. Details of the datasets and resulting parameters used in this study are given in the Supplemental Material.

177

178

179

180

181

182

183

184

185

186

187

188

189

190

We applied the size hysteresis algorithm to ellipsoids of rotation with thirteen different axial ratios, logarithmically spaced between 1/3 and 3. A set of thirteen different titanomagnetite compositions was used, in 5% increments from 0% to 60% Ti. Tetrahedral meshes were produced for each size, shape and composition using the Coreform Cubit software package (Coreform LLC, 2017). The coarseness of the mesh used depended on the size of the geometry (keeping minimum number of elements to  $\sim 15000$ ) and the exchange length ( $\lambda_{\text{ex}}$ ; Rave et al., 1998) of the material. For some combinations of composition and geometry,  $d_{\max}$  was not reached by a size of 500 nm. In these cases, we ran the algorithm to a size of 1  $\mu\text{m}$  (in steps of 50 nm to 800 nm, then 100 nm to 1  $\mu\text{m}$ ), with a set of meshes using a maximum of a million elements. This meant that some meshes exceeded  $\lambda_{\text{ex}}$  and so  $d_{\max}$  values greater than 500 nm should be considered less precise. If  $d_{\max}$  was greater than 1  $\mu\text{m}$ , then it was not reported, and  $d_{\min}$  was instead obtained by forcing a vortex state initial condition at 500 nm and proceeding with the “shrinking” branch as normal.

191

192

193

194

195

196

197

198

199

For each composition and geometry, two size hysteresis simulations were run, one in which the major axis of the ellipsoid was aligned with the magnetocrystalline easy axis of the material (referred to as “magnetocrystalline easy-shape easy” or ME-SE), and one in which it was aligned with the magnetocrystalline hard axis (referred to as “magnetocrystalline hard-shape easy” or MH-SE). The results displayed in Section 3 were produced by taking the maximum  $d_{\max}$  and minimum  $d_{\min}$  of the two datasets for each composition and geometry, and the resulting surfaces were interpolated by a 2d cubic spline using the SciPy package (Virtanen et al., 2020). The difference between results from the ME-SE and MH-SE datasets are discussed in Sections 3.2 and 3.3.

200

201

202

203

204

205

206

207

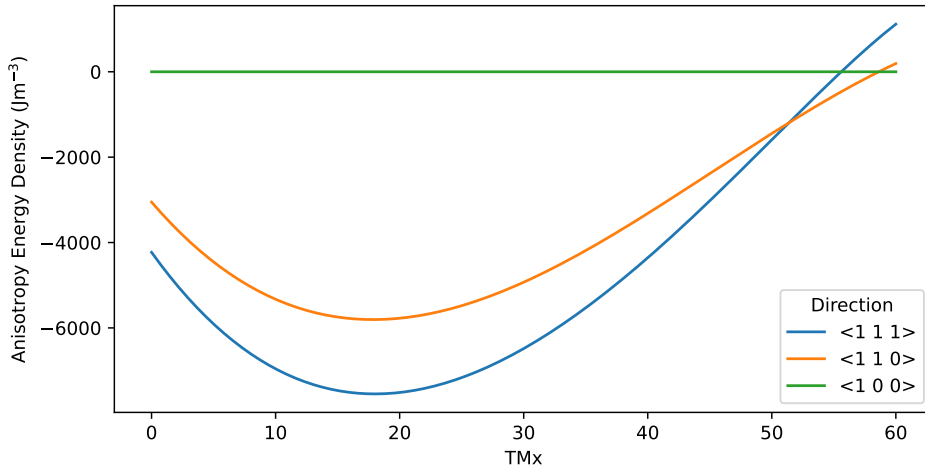
208

209

210

211

The LEMs at each step in the size hysteresis loop were visualized using the ParaView software (Ayachit, 2015). For each visualization, the relative helicity  $h_{\text{rel}}$  was calculated (see supplementary material for details). To determine  $d_{\min}$  and  $d_{\max}$ , the SV structure was identified by the presence of a coherent cylindrical isosurface at  $h_{\text{rel}}=0.95$  containing a “vortex core” intersecting the surface of the particle in two places, and the SD structure was identified by the absence of such a core. Examples of SV structures with vortex cores can be seen in Figure 1 ii and iii). When visualizing LEM states, the volume and magnetization arrows are colored by the absolute cosine of the angle between the individual magnetization vectors and the particle’s net magnetization. The lighter colours in the cores of vortex structures demonstrate that the bulk of the magnetization is carried in this core, and that the volume of the core influences the magnitude of the net magnetization.

212 **3 Results**213 **3.1 Anisotropy energies of the titanomagnetite series**

**Figure 2.** Magnetocrystalline anisotropy energy densities for an SD titanomagnetite particle as a function of composition. Different coloured lines are the anisotropy energy density for different magnetocrystalline directions. The line with the lowest (most negative) magnetocrystalline energy density is the easy axis.

214 Figure 2 shows the magnetocrystalline energy densities in SD titanomagnetites for  
 215 the  $\langle 1\ 0\ 0 \rangle$ ,  $\langle 1\ 1\ 0 \rangle$  and  $\langle 1\ 1\ 1 \rangle$  directions obtained from our fit to experimental data  
 216 for the  $k_1$  and  $k_2$  anisotropy constants. The magnetocrystalline easy axis for a particle  
 217 can be determined by the lowest (most negative) energy. Anisotropy properties change  
 218 significantly across the titanomagnetite series, the easy axis is along  $\langle 1\ 1\ 1 \rangle$  for TM0  
 219 - 50, changing to  $\langle 1\ 1\ 0 \rangle$  at  $\sim$  TM51 and  $\langle 1\ 0\ 0 \rangle$  at  $\sim$  TM59. The hard axis is  $\langle 1$   
 220  $0\ 0 \rangle$  from TM0 - 55 and changes to  $\langle 1\ 1\ 1 \rangle$  just above TM55. The difference in anisotropy  
 221 energy between the easy and hard directions reaches a maximum at  $\sim$  TM20, and is sig-  
 222 nificantly smaller at high TM compositions ( $\geq$ TM40).

223 **3.2 Observed states**

224 Examples of typical states observed during the size hysteresis algorithm are shown  
 225 in Figures 1 and 3. Spherical particles behaved as in Figure 1, with the SD structure chang-  
 226 ing into an SV structure on the growing branch and back to an SD structure on the shrink-  
 227 ing branch, usually rotating to a magnetocrystalline hard direction close to  $d_{\min}$  on the  
 228 shrinking branch (Figure 1 iii). The rotation to a magnetocrystalline hard-aligned vor-  
 229 tex was occasionally preceded by a rotation to a magnetocrystalline intermediate axis,  
 230 particularly in TM55 and TM60 particles. SV states aligned with the magnetocrystalline  
 231 hard axis were found by Nagy et al. (2017) to have extremely low stability, which may  
 232 be of interest for paleomagnetists. Oblate particles behaved similarly for both ME-SE  
 233 and MH-SE anisotropies, nucleating a vortex along the short (shape hard) axis of the  
 234 particle (Figure 3e - f).

235 Different states were observed in prolate particles depending on elongation direc-  
 236 tion: In ME-SE particles, a vortex state aligned along the major axis continued to ex-  
 237 ist without changing up to the maximum size of 500 nm (Figure 3a ii) and continued un-

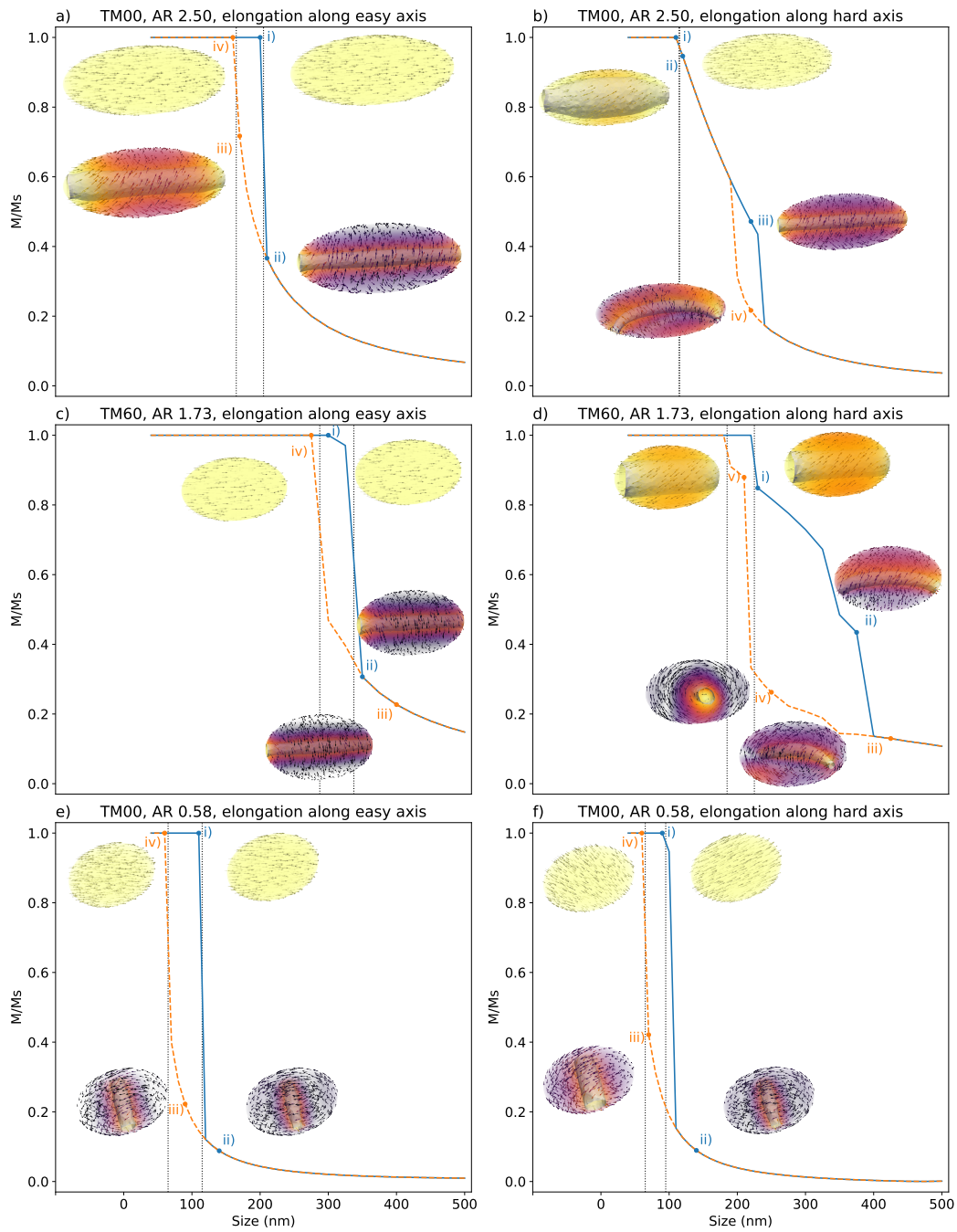


**Figure 3.** Example size hysteresis loop for particles elongated along the magnetocrystalline easy axis (left column) and for the same particles elongated along the magnetocrystalline hard axis (right column). a - b) size hysteresis loop for a prolate magnetite particle with an axial ratio of 2.50. c - d) size hysteresis loop for a prolate TM60 particle with an axial ratio of 1.73. e - f) size hysteresis loop for an oblate particle with an axial ratio of 0.58. In all plots, the numerals i), ii), iii), iv), v) denote the order in which the minimizations were performed, and the colours represent the growing (blue) or shrinking (orange) branch.  $d_{\min}$  and  $d_{\max}$  are plotted as vertical dotted lines.

238 changed down to  $d_{\min}$  (Figure 3a iii). By contrast, in MH-SE particles, a secondary sharp  
 239 drop in the magnetization was observed at sizes above  $d_{\max}$ , with the SV state along the  
 240 major axis (Figure 3b iii) transitioning to a state with a curved vortex core which had  
 241 its ends deflected away from the major axis (Figure 3b iv). These cores were deflected  
 242 in a variety of directions, forming “Banana” or “S” shapes depending on the whether the  
 243 two ends of the core were deflected in adjacent or opposing directions. The deflected vor-  
 244 tex structures persisted to lower sizes on the shrinking branch than on the growing branch,  
 245 leading to another “loop” on the size hysteresis diagrams. The transition at  $d_{\min}$  for MH-  
 246 SE particles was often more subtle than for ME-SE ones, with little change in energy,  
 247 and often a closed loop ( $d_{\min} = d_{\max}$ ) e.g. Fig 3b).

248 The “S” shaped vortices were frequently observed undergoing rotations during the  
 249 shrinking branch of the size hysteresis loop, with the core rotating to lie along one of the  
 250 short (shape-hard) axes of the particle, similar to the states observed in Nagy et al. (2022),  
 251 which were found to cause pTRM tails in paleointensity experiments. This behaviour  
 252 can be seen in Figure 3d ii-iv, and occurred most frequently in prolate particles with ax-  
 253 ial ratios between 1 and 2. This rotation to a short axis was occasionally observed in ME-  
 254 SE particles, but was far less prevalent overall.

### 255 3.3 Trends in $d_{\min}$ and $d_{\max}$

256 The critical domain transition sizes for  $d_{\min}$  and  $d_{\max}$  for each composition and shape  
 257 are presented as contour plots and surfaces in Figure 4. To obtain  $d_{\min}$  and  $d_{\max}$  as a  
 258 continuous function of TM composition and axial ratio, the extant data were interpo-  
 259 lated using a piecewise cubic 2D interpolation routine. White dashed contours with 100  
 260 nm spacing are used to highlight regions where  $d_{\max}$  was greater than 500 nm, where  
 261 a rapid increase occurs. Additionally, some regions of the  $d_{\min}$  and  $d_{\max}$  surfaces are miss-  
 262 ing from this dataset. This is because the SD state persists beyond 1  $\mu\text{m}$  during the grow-  
 263 ing branch of the size hysteresis loop. Obtaining  $d_{\min}$  and  $d_{\max}$  for loops above this size  
 264 becomes rapidly more computationally expensive

265 The surfaces displayed in Figure 4 exhibit some consistent trends with both size  
 266 and shape. Slices through these surfaces (represented by thick lines on Figure 4a, b and  
 267 d) at constant composition or axial ratio are displayed in Figure 5. The most noticeable  
 268 feature of the surfaces is that  $d_{\max}$  sharply increases for both prolate and oblate parti-  
 269 cles relative to equidimensional ones for all compositions (Figure 4a,c). By contrast  $d_{\min}$   
 270 tends to increase with increasing axial ratio across almost all shapes. The relationship  
 271 between  $d_{\max}$  and TM composition is more complicated. For equidimensional particles,  
 272  $d_{\max}$  appears to increase rapidly for compositions from TM00 - TM40, decrease from TM40  
 273 - TM50, followed by another increase to TM55 and a decrease to TM60. This broad trend  
 274 is observed for all other shapes where data are available.  $d_{\min}$  tends to increase relatively  
 275 uniformly with increasing TM composition.

276 The  $d_{\min}$  and  $d_{\max}$  surfaces for both the ME-SE and MH-SE particles are displayed  
 277 in Figure 6. It is apparent that the  $d_{\max}$  surface in Figure 4 is similar to the ME-SE sur-  
 278 face, except at the highest TM compositions. This is primarily driven by the reduced  
 279  $d_{\max}$  for prolate MH-SE particles, with many of the loops being closed (i.e.  $d_{\min} = d_{\max}$ ).  
 280 The anisotropy for MH-SE particles has a less uniaxial character, and so the SD struc-  
 281 ture cannot be a LEM state at larger sizes. The LEM states in the ME-SE particles change  
 282 rapidly from an SD structure to a vortex structure, accompanied by a sharp drop in the  
 283 net magnetization (Figure 3a i to ii) By contrast, the MH-SE particles change more grad-  
 284 ually from an SD to an SV structure (Figure 3b i to ii), with the first SV states having  
 285 wide vortex cores encompassing nearly the entire particle. There is also a reduction in  
 286  $d_{\max}$  for MH-SE oblate surfaces (Figure 3e - f), particularly at intermediate TM com-  
 287 positions.

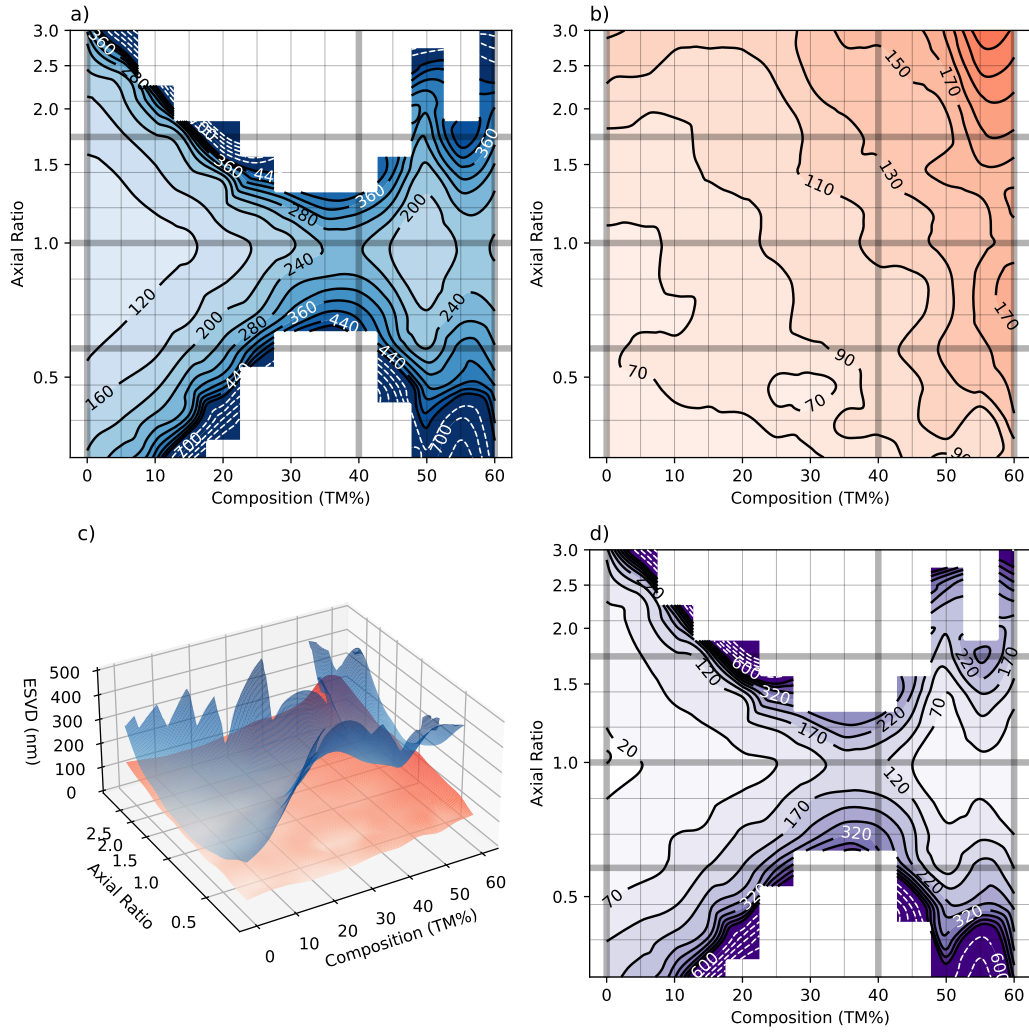


**Figure 4.** Plots of the maximum  $d_{\max}$  and minimum  $d_{\min}$  of the ME-SE and MH-SE anisotropies as a function of composition and shape. a) Contour plot of the maximum size at which the SD structure was observed on growing ( $d_{\max}$ ). b) Contour plot of the minimum size at which the SV structure was observed when shrinking ( $d_{\min}$ ). c) 3D surface plot of the  $d_{\min}$  and  $d_{\max}$  surfaces in a and b. d) Contour plot of the difference (in nm) between the surfaces shown in a, b and c. This represents the range of sizes where both the SD and SV structures are available to a particle of this composition and geometry. The surface and contour plots shown here are produced from a smoothed cubic spline surface fit to the data, with the original data located on the corners of the grid. Thicker grid lines show the locations of slices through the contour plot shown in Figure 5. White dashed contours represent wider spacings of 100 nm in regions where  $500 < d_{\max} < 1000$  nm, where the models may be less precise. Note that for ease of viewing, the surface in c is truncated at 500 nm.  $d_{\max}$  data are missing for particles that remained in the SD structure after growing to  $1 \mu\text{m}$ .

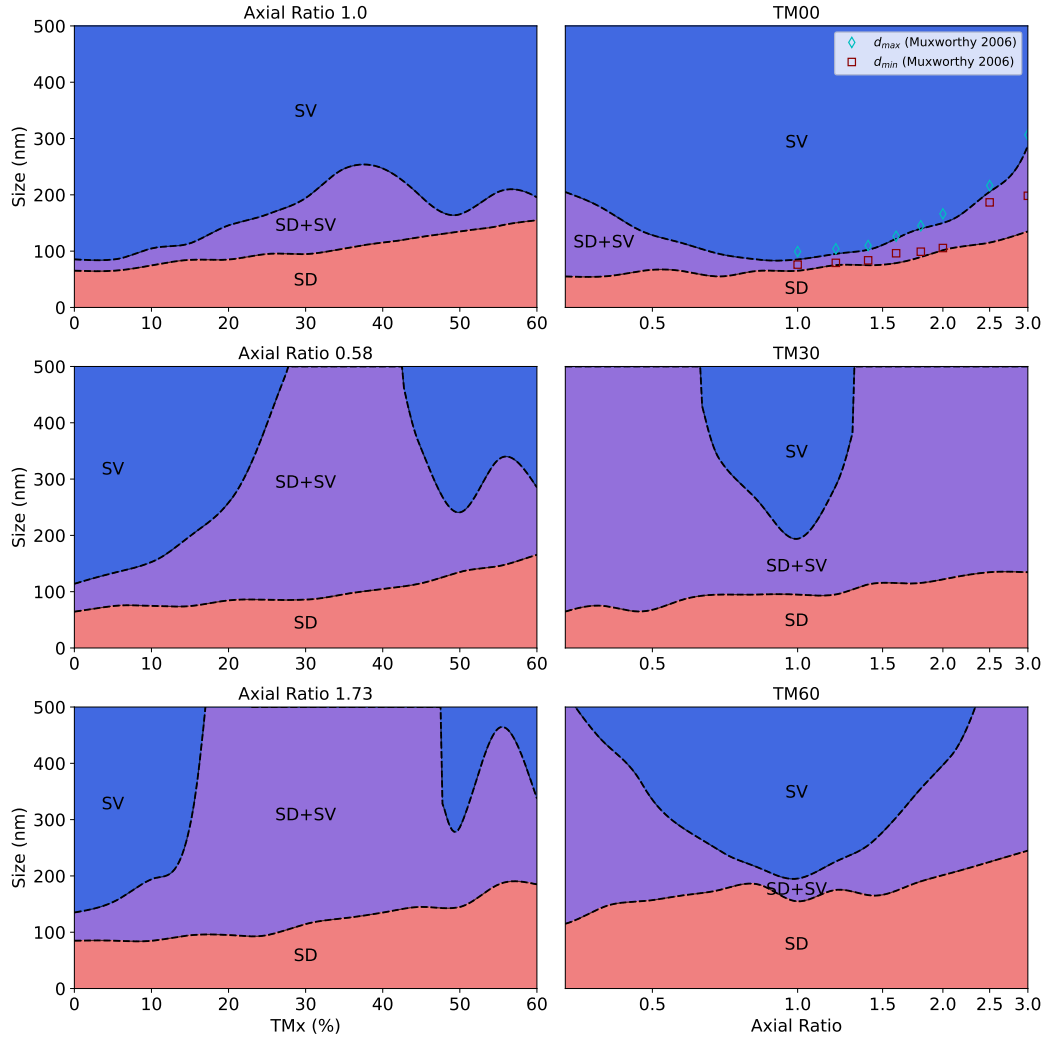


**Figure 5.** Slices through surfaces displayed in Figure 4. Blue represents regions above the upper surface where the SV structure (and other more complicated states) is available. Red represents the region in which the SD structure is available. Purple represents the range of sizes in which the SD and SV structures are both available. For the TM00 (magnetite) composition, the minimum  $d_{min}$  and maximum  $d_{max}$  of Muxworthy and Williams (2006) are plotted as red squares and blue diamonds for comparison.

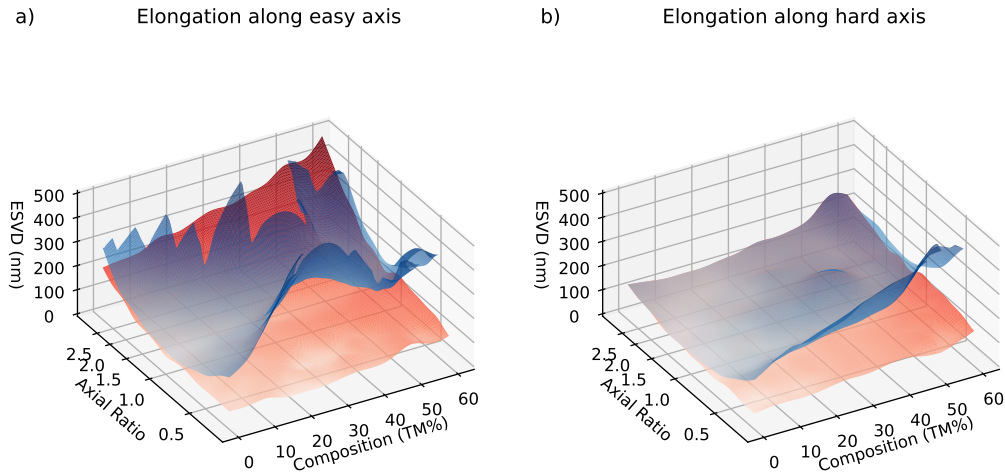


**Figure 6.** Critical size surfaces for ME-SE (left) vs MH-SE (right) particles. The presentation of these surfaces is the same as in Figure 4c.

## 288 4 Discussion

### 289 4.1 Comparison to other studies

290 Our results provide the first description of the domain states present in titanomag-  
 291 netites using modern micromagnetic models. Our maps of the size ranges of the SD and  
 292 SV structures follow the work of Butler and Banerjee (1975), but our results are based  
 293 on unconstrained, inhomogeneous 3-D models. This allows us to evaluate the true LEM  
 294 states not available from classic Kittel two-domain structure calculations. Additionally,  
 295 our titanomagnetite material parameters are empirically derived using far more data than  
 296 were available to Butler and Banerjee, and include the second magnetocrystalline anisotropy  
 297 constant  $k_2$ . This robust physical basis, combined with the increased scale and resolu-  
 298 tion of our models, enables us to make realistic predictions about the domain states of  
 299 remanence carriers in igneous rocks. This in turn enables us to identify carriers with po-  
 300 tential to cause problematic behaviors in paleomagnetic experiments.

301 The results presented in Section 3 are most quantitatively comparable to those of  
 302 Muxworthy and Williams (2006), who applied the size-hysteresis algorithm for prolate  
 303 magnetite parallelepipeds. We extend this approach to 12 additional compositions and  
 304 oblate geometries. Our results for  $d_{\min}$  and  $d_{\max}$  in magnetite are compared to theirs  
 305 (converted to ESVD) in Figure 5. The  $d_{\max}$  data follow a very similar trend with our  
 306  $d_{\max}$  values being slightly smaller for all elongations. The  $d_{\min}$  values are also mostly  
 307 consistent, but Muxworthy & Williams observe a large increase in  $d_{\min}$  at an axial ra-  
 308 tio of 2.5, which is not seen in our data. The general similarity between the trends in  
 309 both studies is encouraging, demonstrating the reproducibility of the size-hysteresis al-  
 310 gorithm.

311 The discrepancy between some of our  $d_{\min}$  values and those of Muxworthy and Williams  
 312 (2006) can be explained by numerous differences between our methodology and theirs;  
 313 The material parameters for magnetite used are slightly different, our domain states are  
 314 defined differently, Muxworthy & Williams used a micromagnetic method involving a fast  
 315 fourier transform rather than the finite element method currently used in MERRILL,  
 316 and our results are for ellipsoidal particles rather than parallelepipeds. Ellipsoids were

317 used because faceted surfaces affect the available domain states available to a particle,  
 318 an effect known as configurational anisotropy (see W. Williams et al., 2006 for a detailed  
 319 discussion). The ellipsoidal geometry minimizes the effect of configurational anisotropy  
 320 by minimizing the size of faceted surfaces, ensuring that the dominant controls on  $d_{\min}$   
 321 and  $d_{\max}$  are composition and axial ratio.

322 Usov and Serebryakova (2023) calculated the energies of different domain states  
 323 present in magnetite ellipsoids, using a different algorithm to that employed in MER-  
 324 RILL. They calculated a critical size, defined as the size at which the energy of the SV  
 325 structure was lower than that of the SD structure. These critical sizes lie between our  
 326  $d_{\min}$  and  $d_{\max}$  when converted to ESVD, which should be expected as our critical sizes  
 327 are bounds on the existence of the structures. The authors findings also shared three com-  
 328 mon features with ours; Firstly, differences between the size ranges of domain structures  
 329 in ME-SE and MH-SE particles. Secondly, SD and SV structures existing in overlapping  
 330 size ranges. Finally, SV states aligned with a variety of magnetocrystalline and shape  
 331 easy/hard directions. These similarities when using a different software, algorithm, and  
 332 material parameters suggest that these features are robust properties of titanomagnetites.

## 333 4.2 Domain states and instability

334 The range of sizes between  $d_{\min}$  and  $d_{\max}$ , where both the SD and SV structures  
 335 can exist, is largest for highly elongated or flattened particles and intermediate TM com-  
 336 positions. Within this range of sizes, the magnetocrystalline hard-aligned vortex observed  
 337 by Nagy et al. (2017) is observed in equidimensional particles, and the multiple avail-  
 338 able domain states could lead to non-ideal “pTRM tail” type behaviour in paleointen-  
 339 sity experiments. The “unstable zone” of Nagy et al. containing magnetocrystalline hard-  
 340 aligned vortices was only found to be  $\sim 10$  nm wide for equidimensional magnetite, but  
 341 we demonstrate that for other compositions and geometries, there are multiple available  
 342 domain states that can exist over many hundreds of nanometers.

343 A second region with multiple domain structures was observed in prolate MH-SE  
 344 particles at larger sizes than  $d_{\max}$  (e.g. Figure 3b, d). In this region, an SV state aligned  
 345 with the long (shape-easy) of the particle coexists with a state where the ends of the vor-  
 346 tex core are deflected away from this axis. The deflection is likely related to the influ-  
 347 ence of the magnetocrystalline easy axes, which could pull the core away from the shape-  
 348 easy direction towards one of a number of magnetocrystalline-easy directions. Upon fur-  
 349 ther shrinking, the vortex core rotated further and shape-hard aligned SV states were  
 350 frequently observed. The multiplicity of states offered by the different magnetocrystalline  
 351 and shape directions, and the wide range of sizes over which these states overlap with  
 352 the SV state suggest that there may be a second “unstable zone” in prolate MH-SE par-  
 353 ticles above  $d_{\max}$  and into the SV size range. Nagy et al. (2022) simulated pTRM tail  
 354 behaviour using a prolate faceted magnetite particle that did not have any single-domain  
 355 LEM states, supporting this hypothesis.

356 Without thermal energy barriers, size hysteresis experiments cannot calculate the  
 357 stability of individual particles, but the  $d_{\min}$  and  $d_{\max}$  sizes represent bounds on a re-  
 358 gion of interest, which should be a target for future micromagnetic studies. Energy bar-  
 359 rier calculations for particles in this region may further our understanding of the pTRM  
 360 tail phenomenon. Equidimensional particles near  $d_{\min}$  and prolate MH-SE particles should  
 361 be of particular interest to researchers studying this phenomenon, as they exhibit the  
 362 largest variety of states including the magnetocrystalline hard-aligned vortices of Nagy  
 363 et al. (2017) and the shape hard-aligned vortices of Nagy et al. (2022).

### 364 4.3 The effect of elongation direction

365 Overall, our findings indicate that the domain states available to magnetic parti-  
 366 cles have a dependence on the alignment of the magnetocrystalline and shape easy axes  
 367 (as seen in Figures 3 and 6). This effect has also been observed in micromagnetic algo-  
 368 rithms using magnetite cuboids by Muxworthy and Williams (2006) and recently in mag-  
 369 netite ellipsoids by Usov and Serebryakova (2023). Our results indicate that this effect  
 370 may be even more important than previously thought, as we observe domain states in  
 371 prolate titanomagnetites that are only present when the elongation direction is along a  
 372 shape hard axis, which may cause instability as multiple domain states exist in this re-  
 373 gion.

374 There have been few observations of the relationship between the elongation di-  
 375 rection and magnetization direction in natural samples. Feinberg et al. (2004) used the  
 376 Electron Back-Scatter Diffraction (EBSD) technique to make observations about the ori-  
 377 entations of prolate magnetite particles exsolved in clinopyroxene, and Ageeva et al. (2020)  
 378 used the same technique to investigate particles exsolved in plagioclase. Both found mag-  
 379 netite particles elongated along the  $\langle 111 \rangle$  (magnetocrystalline easy) and  $\langle 110 \rangle$  (in-  
 380 termediate) directions. By contrast, Li et al. (2020) recently found that bullet shaped  
 381 magnetite particles in chains of magnetosomes were predominantly elongated along the  
 382  $\langle 100 \rangle$  (hard) axis. These limited studies indicate that there is varying competition  
 383 between shape and magnetocrystalline axes in natural samples, with the dominant anisotropies  
 384 being strongly tied to the mechanism of particle growth. More EBSD observations of the  
 385 elongation directions in titanomagnetites of different origins will be necessary to constrain  
 386 the available domain states in a wider range of real samples.

## 387 5 Conclusions

388 We present a comprehensive set of results from micromagnetic models to determine  
 389 the range of possible domain states in ellipsoidal titanomagnetite particles of varying size,  
 390 shape and composition. Previous micromagnetic models characterizing the domain states  
 391 in samples have focused solely on equidimensional and prolate magnetite particles. The  
 392 range of compositions and shapes described in our study increase the number of exist-  
 393 ing domain state characterizations by more than an order of magnitude, improving our  
 394 understanding of a much wider range of remanence carriers.

395 For each titanomagnetite composition and geometry, we find the critical size at which  
 396 a single domain (SD) magnetization transitions to a single vortex (SV) magnetization  
 397 upon growing a particle ( $d_{\max}$ ) and the size at which an SV magnetization transitions  
 398 to an SD magnetization on shrinking the particle ( $d_{\min}$ ). Particles between these sizes  
 399 can be magnetized both in the single domain structure, and the single vortex structure.  
 400 This is significant, as for these particles we observe vortex structures aligned along the  
 401 magnetocrystalline hard axis, which were found to be unstable by Nagy et al. (2017).  
 402 Our results indicate that titanomagnetite particles of intermediate composition have a  
 403 larger range of sizes where both the SD and SV structures are available, and that this  
 404 range of sizes is larger for both oblate and prolate particles than for equidimensional ones.

405 Further, we find that the angle between the magnetocrystalline and shape easy axes  
 406 has a significant effect on the observed domain states in a particle. Prolate particles have  
 407 a much larger SD + SV size range when their elongation direction is along the magne-  
 408 tocrystalline easy axis (ME-SE) than when along the hard axis (MH-SE). MH-SE pro-  
 409 late particles exhibit “S” and “Banana” states in the SV size range, where the vortex core  
 410 of the magnetization is deflected away from the elongation direction. These states some-  
 411 times rotate to the particle’s short axis on shrinking, leading to a potential second “un-  
 412 stable zone” in titanomagnetites. Further investigation of the relationship between par-

413 ticle shape and crystallographic directions in natural samples should be undertaken to  
414 better understand this effect.

415 Overall, we show that the domain states available to grains vary as a function of  
416 shape and composition. The domain states observed indicate that the range of sizes, shapes  
417 and compositions of unstable remanence carriers that cause problematic behavior in pa-  
418 leomagnetic studies could be far larger than previously demonstrated. A prevalence of  
419 these carriers could explain the high failure rate of paleointensity experiments seen in  
420 paleomagnetic literature. Future work will focus on the unstable particles identified in  
421 this study to understand the effects of these instabilities on paleomagnetic experiments.

## 422 Open Research

423 The micromagnetic models were produced using the open source micromagnetic  
424 modeling MERRILL (Ó Conbhuí et al., 2018; W. Williams et al., n.d.), which is avail-  
425 able under a CC-BY-SA 4.0 International license at [https://bitbucket.org/wynwilliams/  
426 merrill/](https://bitbucket.org/wynwilliams/merrill/). A Zenodo repository containing a spreadsheet of results, as well as example  
427 scripts to reproduce this research can be found at [https://doi.org/10.5281/zenodo  
428 .10471806](https://doi.org/10.5281/zenodo.10471806) (Cych, 2024).

## 429 Acknowledgements

430 B.C. and G.A.P. acknowledge funding from Natural Environmental Research Coun-  
431 cil (NERC) grant NE/W006707/1. G.A.P. further acknowledges a NERC Independent  
432 Research Fellowship (NE/P017266/1). L.N. acknowledges funding from NERC Indepen-  
433 dent Research Fellowship NE/V014722/1. W.W. acknowledges NERC grants NE/S001018/1  
434 and NE/V001388/1. The Institute for Rock Magnetism (IRM) is a US National Multi-  
435 user Facility supported through the Instrumentation and Facilities program of the Na-  
436 tional Science Foundation, Earth Sciences Division, award NSF-EAR 2153786, and by  
437 funding from the University of Minnesota. This is IRM publication number 2401.

## 438 References

- 439 Ageeva, O., Bian, G., Habler, G., Pertsev, A., & Abart, R. (2020). Crystallographic  
440 and shape orientations of magnetite micro-inclusions in plagioclase. *Contrib.  
441 Mineral. Petrol.*, *175*(10), 1–16. doi: 10.1007/s00410-020-01735-8
- 442 Ahn, H.-S., Kidane, T., Yamamoto, Y., & Otofujii, Y.-i. (2016). Low geomagnetic  
443 field intensity in the matuyama chron: palaeomagnetic study of a lava se-  
444 quence from afar depression, east africa. *Geophysical Journal International*,  
445 *204*(1), 127–146.
- 446 Akimoto, S.-i., Katsura, T., & Yoshida, M. (1957). Magnetic properties of  $\text{TiFe}_2\text{O}_4$ -  
447  $\text{Fe}_3\text{O}_4$  system and their change with oxidation. *J. Geomagn. Geoelec.*, *9*(4),  
448 165–178. doi: 10.5636/jgg.9.165
- 449 Aragón, R. (1992). Cubic magnetic anisotropy of nonstoichiometric magnetite. *Phys-  
450 ical Review B*, *46*(9), 5334.
- 451 Ayachit, U. (2015). *The paraview guide: a parallel visualization application*. Kitware,  
452 Inc.
- 453 Banerjee, S. K. (1991). Magnetic properties of Fe-Ti oxides. In D. H. Lindsley (Ed.),  
454 *Oxide minerals: Petrologic and magnetic significance* (pp. 107–128). Berlin,  
455 Boston: De Gruyter. doi: 10.1515/9781501508684-007
- 456 Bickford, L., Brownlow, J., & Penoyer, R. (1957). Magnetocrystalline anisotropy  
457 in cobalt-substituted magnetite single crystals. *Proceedings of the IEE-Part B:  
458 Radio and Electronic Engineering*, *104*(5S), 238–244.
- 459 Bickford Jr, L. (1950). Ferromagnetic resonance absorption in magnetite single crys-  
460 tals. *Physical Review*, *78*(4), 449.

- 461 Bleil, U. (1976). An experimental study of the titanomagnetite solid solution series.  
462 *Pure and Applied geophysics*, *114*, 165–175.
- 463 Böhnel, H. N., Dekkers, M. J., Delgado-Argote, L. A., & Gratton, M. N. (2009).  
464 Comparison between the microwave and multispecimen parallel difference p<sub>trm</sub>  
465 paleointensity methods. *Geophysical Journal International*, *177*(2), 383–394.
- 466 Bol'Shakov, A. (1979). A thermomagnetic criterion for determining the domain  
467 structure of ferrimagnetics. *Izv. Acad. Sci. USSR Phys. Solid Earth*, *15*, 111–  
468 117.
- 469 Bowles, J. A., Gerzich, D. M., & Jackson, M. J. (2018). Assessing new and old  
470 methods in paleomagnetic paleothermometry: a test case at Mt. St. Helens,  
471 USA. *Geochemistry, Geophysics, Geosystems*, *19*(6), 1714–1730.
- 472 Bowles, J. A., Morris, A., Tivey, M., & Lascu, I. (2020). Magnetic mineral popula-  
473 tions in lower oceanic crustal gabbros (Atlantis bank, SW Indian ridge): Impli-  
474 cations for marine magnetic anomalies. *Geochemistry, Geophysics, Geosystems*,  
475 *21*(3), e2019GC008847.
- 476 Brown, W. F. B. (1963). *Micromagnetics*. New York: John Wiley & Sons.
- 477 Butler, R. F., & Banerjee, S. K. (1975). Theoretical single-domain grain size range  
478 in magnetite and titanomagnetite. *J. Geophys. Res.*, *80*(29), 4049–4058. doi:  
479 10.1029/JB080i029p04049
- 480 Calhoun, B. (1954). Magnetic and electric properties of magnetite at low tempera-  
481 tures. *Physical Review*, *94*(6), 1577.
- 482 Calvo, M., Prévot, M., Perrin, M., & Riisager, J. (2002). Investigating the reasons  
483 for the failure of palaeointensity experiments: a study on historical lava flows  
484 from Mt. Etna (Italy). *Geophysical journal international*, *149*(1), 44–63.
- 485 Calvo-Rathert, M., Bógalo, M. F., Gogichaishvili, A., Sologashvili, J., & Vashakidze,  
486 G. (2013). New paleomagnetic and paleointensity data from pliocene lava flows  
487 from the lesser caucasus. *Journal of Asian Earth Sciences*, *73*, 347–361.
- 488 Calvo-Rathert, M., Goguitchaichvili, A., Bógalo, M.-F., Vegas-Tubía, N., Carrancho,  
489 Á., & Sologashvili, J. (2011). A paleomagnetic and paleointensity study on  
490 pleistocene and pliocene basaltic flows from the djavakheti highland (southern  
491 georgia, caucasus). *Physics of the Earth and Planetary interiors*, *187*(3-4),  
492 212–224.
- 493 Calvo-Rathert, M., Goguitchaichvili, A., & Vegas-Tubia, N. (2009). A paleointensity  
494 study on middle miocene to pliocene volcanic rocks from south-eastern spain.  
495 *Earth, planets and space*, *61*, 61–69.
- 496 Carvallo, C., Camps, P., Ruffet, G., Henry, B., & Poidras, T. (2003). Mono lake  
497 or Laschamp geomagnetic event recorded from lava flows in Amsterdam is-  
498 land (southeastern Indian Ocean). *Geophysical Journal International*, *154*(3),  
499 767–782.
- 500 Carvallo, C., Özdemir, Ö., & Dunlop, D. J. (2004). Palaeointensity determina-  
501 tions, palaeodirections and magnetic properties of basalts from the Emperor  
502 seamounts. *Geophysical Journal International*, *156*(1), 29–38.
- 503 Chauvin, A., Gillot, P.-Y., & Bonhommet, N. (1991). Paleointensity of the Earth's  
504 magnetic field recorded by two late quaternary volcanic sequences at the island  
505 of La Réunion (Indian ocean). *Journal of Geophysical Research: Solid Earth*,  
506 *96*(B2), 1981–2006.
- 507 Chikazumi, S. (1964). *Physics of magnetism*. John Wiley & Sons.
- 508 Coe, R. S., Grommé, S., & Mankinen, E. A. (1978). Geomagnetic paleointensities  
509 from radiocarbon-dated lava flows on Hawaii and the question of the pacific  
510 nondipole low. *Journal of Geophysical Research: Solid Earth*, *83*(B4), 1740–  
511 1756.
- 512 Coe, R. S., Gromme, S., & Mankinen, E. A. (1984). Geomagnetic paleointensities  
513 from excursion sequences in lavas on Oahu, Hawaii. *Journal of Geophysical Re-  
514 search: Solid Earth*, *89*(B2), 1059–1069.
- 515 Coreform LLC. (2017). *Coreform Cubit, v2022.4 (64-Bit)*. Retrieved from <https://>

- 516 coreform.com
- 517 Cych, B. (2024). *Titanomagnetite size hysteresis*. Zenodo. Retrieved from  
 518 <https://doi.org/10.5281/zenodo.10471806> (Software) doi: 10.5281/  
 519 zenodo.10471806
- 520 de Groot, L. V., Dekkers, M. J., & Mullender, T. A. (2012). Exploring the potential  
 521 of acquisition curves of the anhysteretic remanent magnetization as a tool to  
 522 detect subtle magnetic alteration induced by heating. *Physics of the Earth and  
 523 Planetary Interiors*, *194*, 71–84.
- 524 de Groot, L. V., Mullender, T. A., & Dekkers, M. J. (2013). An evaluation of the  
 525 influence of the experimental cooling rate along with other thermomagnetic  
 526 effects to explain anomalously low palaeointensities obtained for historic lavas  
 527 of Mt Etna (Italy). *Geophysical Journal International*, *193*(3), 1198–1215.
- 528 Donadini, F., Elming, S.-Å., Tauxe, L., & Hålenius, U. (2011). Paleointensity de-  
 529 termination on a 1.786 ga old gabbro from Hoting, central Sweden. *Earth and  
 530 Planetary Science Letters*, *309*(3-4), 234–248.
- 531 Dunlop, D. J., & Özdemir, Ö. (2001). Beyond Néel’s theories: thermal demagne-  
 532 tization of narrow-band partial thermoremanent magnetizations. *Phys. Earth  
 533 Planet. Inter.*, *126*(1), 43–57. doi: 10.1016/S0031-9201(01)00243-6
- 534 Dunlop, D. J., & Özdemir, Ö. (1997). *Rock magnetism: fundamentals and frontiers*  
 535 (No. 3). Cambridge university press.
- 536 Fabian, K., Kirchner, A., Williams, W., Heider, F., Leibl, T., & Huber, A. (1996).  
 537 Three-dimensional micromagnetic calculations for magnetite using FFT. *Geo-  
 538 phys. J. Int.*, *124*(1), 89–104. doi: 10.1111/j.1365-246X.1996.tb06354.x
- 539 Feinberg, J. M., Harrison, R. J., Kasama, T., Dunin-Borkowski, R. E., Scott, G. R.,  
 540 & Renne, P. R. (2006). Effects of internal mineral structures on the magnetic  
 541 remanence of silicate-hosted titanomagnetite inclusions: An electron hologra-  
 542 phy study. *Journal of Geophysical Research: Solid Earth*, *111*(B12).
- 543 Feinberg, J. M., Wenk, H.-R., Renne, P. R., & Scott, G. R. (2004). Epitaxial  
 544 relationships of clinopyroxene-hosted magnetite determined using electron  
 545 backscatter diffraction (EBSD) technique. *Am. Mineral.*, *89*(2-3), 462–466.  
 546 doi: 10.2138/am-2004-2-328
- 547 Ferk, A., Aulock, F. v., Leonhardt, R., Hess, K.-U., & Dingwell, D. (2010). A  
 548 cooling rate bias in paleointensity determination from volcanic glass: An ex-  
 549 perimental demonstration. *Journal of Geophysical Research: Solid Earth*,  
 550 *115*(B8).
- 551 Ferk, A., Denton, J., Leonhardt, R., Tuffen, H., Koch, S., Hess, K.-U., & Dingwell,  
 552 D. (2012). Paleointensity on volcanic glass of varying hydration states. *Physics  
 553 of the Earth and Planetary Interiors*, *208*, 25–37.
- 554 Fletcher, E., & O’Reilly, W. (1974). Contribution of Fe<sup>2+</sup> ions to the magnetocrys-  
 555 talline anisotropy constant  $k_1$  of Fe<sub>3-x</sub>Ti<sub>x</sub>O<sub>4</sub> (0 < x < 1). *Journal of Physics  
 556 C: Solid State Physics*, *7*(1), 171.
- 557 Fontana, G., Mac Niocaill, C., Brown, R. J., Sparks, R. S. J., & Field, M. (2011).  
 558 Emplacement temperatures of pyroclastic and volcanoclastic deposits in kim-  
 559 berlite pipes in southern Africa. *Bulletin of Volcanology*, *73*, 1063–1083.
- 560 Fredkin, D., & Koehler, T. (1987). Numerical micromagnetics by the finite element  
 561 method. *IEEE Transactions on Magnetism*, *23*(5), 3385–3387.
- 562 Gonzalez, S., Sherwood, G., Böhnell, H., & Schnepf, E. (1997). Palaeosecular vari-  
 563 ation in central Mexico over the last 30000 years: the record from lavas. *Geo-  
 564 physical Journal International*, *130*(1), 201–219.
- 565 Hauptman, Z. (1974). High temperature oxidation, range of non-stoichiometry and  
 566 curie point variation of cation deficient titanomagnetite Fe<sub>2.4</sub>Ti<sub>0.6</sub>O<sub>4+γ</sub>. *Geo-  
 567 physical Journal International*, *38*(1), 29–47.
- 568 Heider, F., & Williams, W. (1988). Note on temperature dependence of exchange  
 569 constant in magnetite. *Geophysical Research Letters*, *15*(2), 184–187.
- 570 Hill, M. J., & Shaw, J. (1999). Palaeointensity results for historic lavas from Mt

- 571 Etna using microwave demagnetization/remagnetization in a modified Thellier-  
572 type experiment. *Geophysical Journal International*, 139(2), 583–590.
- 573 Hill, M. J., & Shaw, J. (2000). Magnetic field intensity study of the 1960 Kilauea  
574 lava flow, Hawaii, using the microwave palaeointensity technique. *Geophysical*  
575 *Journal International*, 142(2), 487–504.
- 576 Hunt, C. P., Moskowitz, B. M., & Banerjee, S. K. (1995). Magnetic properties of  
577 rocks and minerals. *Rock physics and phase relations: A handbook of physical*  
578 *constants*, 3, 189–204.
- 579 Kąkol, Z., Sabol, J., & Honig, J. (1991a). Cation distribution and magnetic proper-  
580 ties of titanomagnetites  $\text{Fe}_{3-x}\text{Ti}_x\text{O}_4$  ( $0 \leq x < 1$ ). *Physical Review B*, 43(1),  
581 649.
- 582 Kąkol, Z., Sabol, J., & Honig, J. (1991b). Magnetic anisotropy of titanomagnetites  
583  $\text{Fe}_{3-x}\text{Ti}_x\text{O}_4$  ( $0 \leq x < 0.55$ ). *Physical Review B*, 44(5), 2198.
- 584 Kąkol, Z., Sabol, J., Stickler, J., Kozłowski, A., & Honig, J. (1994). Influence of ti-  
585 tanium doping on the magnetocrystalline anisotropy of magnetite. *Physical Re-*  
586 *view B*, 49(18), 12767.
- 587 Keefer, C. M., & Shive, P. N. (1981). Curie temperature and lattice constant  
588 reference contours for synthetic titanomaghemites. *Journal of Geophysical*  
589 *Research: Solid Earth*, 86(B2), 987–998.
- 590 Khakhalova, E., Moskowitz, B. M., Williams, W., Biedermann, A. R., & Solheid,  
591 P. (2018). Magnetic vortex states in small octahedral particles of interme-  
592 diate titanomagnetite. *Geochem. Geophys. Geosyst.*, 19(9), 3071–3083. doi:  
593 10.1029/2018GC007723
- 594 Kittel, C. (1949). Physical theory of ferromagnetic domains. *Reviews of modern*  
595 *Physics*, 21(4), 541.
- 596 Kono, M. (1974). Intensities of the Earth’s magnetic field about 60 my ago deter-  
597 mined from the Deccan trap basalts, India. *Journal of Geophysical Research*,  
598 79(8), 1135–1141.
- 599 Kono, M., & Tosha, T. (1980). Geomagnetic paleointensity measurements on leg 55  
600 basalts. *Init. Repts. DSDP*, 753–758.
- 601 Larson, E., Ozima, M., Ozima, M., Nagata, T., & Strangway, D. (1969). Stability of  
602 remanent magnetization of igneous rocks. *Geophysical Journal International*,  
603 17(3), 263–292.
- 604 Li, J., Menguy, N., Roberts, A. P., Gu, L., Leroy, E., Bourgon, J., . . . Pan, Y.  
605 (2020). Bullet-shaped magnetite biomineralization within a magnetotactic  
606 deltaproteobacterium: Implications for magnetofossil identification. *J. Geo-*  
607 *phys. Res. Biogeosci.*, 125(7), e2020JG005680. doi: 10.1029/2020JG005680
- 608 Mankinen, E. A. (1994). *Preliminary geomagnetic paleointensities from long valley*  
609 *caldera, california*. US Geological Survey.
- 610 Martín-Hernández, F., Bominaar-Silkens, I. M., Dekkers, M. J., & Maan, J. K.  
611 (2006). High-field cantilever magnetometry as a tool for the determination of  
612 the magnetocrystalline anisotropy of single crystals. *Tectonophysics*, 418(1-2),  
613 21–30.
- 614 Matzka, J., & Krása, D. (2007). Oceanic basalt continuous thermal demagnetization  
615 curves. *Geophysical Journal International*, 169(3), 941–950.
- 616 Michalk, D. M., Biggin, A. J., Knudsen, M. F., Böhnel, H. N., Nowaczyk, N. R.,  
617 Ownby, S., & López-Martínez, M. (2010). Application of the multispecimen  
618 palaeointensity method to pleistocene lava flows from the Trans-Mexican vol-  
619 canic belt. *Physics of the Earth and Planetary Interiors*, 179(3-4), 139–156.
- 620 Moskowitz, B. M. (1980). Theoretical grain size limits for single-domain, pseudo-  
621 single-domain and multi-domain behavior in titanomagnetite ( $x = 0.6$ ) as a  
622 function of low-temperature oxidation. *Earth Planet. Sci. Lett.*, 47(2), 285–  
623 293. doi: 10.1016/0012-821X(80)90045-X
- 624 Moskowitz, B. M. (1993). High-temperature magnetostriction of magnetite and ti-  
625 tanomagnetites. *Journal of Geophysical Research: Solid Earth*, 98(B1), 359–

- 371.
- 626  
627 Moskowitz, B. M., & Halgedahl, S. L. (1987). Theoretical temperature and grain-size  
628 dependence of domain state in  $x=0.6$  titanomagnetite. *Journal of Geophysical*  
629 *Research: Solid Earth*, *92*(B10), 10667–10682.
- 630 Moskowitz, B. M., Jackson, M., & Kissel, C. (1998). Low-temperature magnetic  
631 behavior of titanomagnetites. *Earth and Planetary Science Letters*, *157*(3-4),  
632 141–149.
- 633 Muxworthy, A. R., & Williams, W. (2006). Critical single-domain/multidomain  
634 grain sizes in noninteracting and interacting elongated magnetite particles:  
635 Implications for magnetosomes. *J. Geophys. Res. Solid Earth*, *111*(B12). doi:  
636 10.1029/2006JB004588
- 637 Muxworthy, A. R., & Williams, W. (2015). Critical single-domain grain sizes in  
638 elongated iron particles: implications for meteoritic and lunar magnetism. *Geo-*  
639 *phys. J. Int.*, *202*(1), 578–583. doi: 10.1093/gji/ggv180
- 640 Muxworthy, A. R., Williams, W., Roberts, A. P., Winklhofer, M., Chang, L., &  
641 Pósfai, M. (2013). Critical single domain grain sizes in chains of interacting  
642 greigite particles: Implications for magnetosome crystals. *Geochem. Geophys.*  
643 *Geosyst.*, *14*(12), 5430–5441. doi: 10.1002/2013GC004973
- 644 Nagy, L., Williams, W., Muxworthy, A. R., Fabian, K., Almeida, T. P., Conbhuí,  
645 P. Ó., & Shcherbakov, V. P. (2017). Stability of equidimensional  
646 pseudo-single-domain magnetite over billion-year timescales. *Proc. Natl.*  
647 *Acad. Sci. U.S.A.*, *114*(39), 10356–10360. doi: 10.1073/pnas.1708344114
- 648 Nagy, L., Williams, W., Tauxe, L., & Muxworthy, A. (2022). Chasing tails: In-  
649 sights from micromagnetic modeling for thermomagnetic recording in non-  
650 uniform magnetic structures. *Geophys. Res. Lett.*, *49*(23), e2022GL101032.  
651 doi: 10.1029/2022GL101032
- 652 Nagy, L., Williams, W., Tauxe, L., & Muxworthy, A. R. (2019). From nano to  
653 micro: Evolution of magnetic domain structures in multidomain magnetite.  
654 *Geochem. Geophys. Geosyst.*, *20*(6), 2907–2918. doi: 10.1029/2019GC008319
- 655 Néel, L. (1949). Théorie du traînage magnétique des ferromagnétiques en grains fins  
656 avec application aux terres cuites. *Annales de géophysique*, *5*, 99–136.
- 657 Newell, A. J., Dunlop, D. J., & Enkin, R. J. (1990). Temperature dependence  
658 of critical sizes, wall widths and moments in two-domain magnetite grains.  
659 *Physics of the earth and planetary interiors*, *65*(1-2), 165–176.
- 660 Nishitani, T., & Kono, M. (1983). Curie temperature and lattice constant of oxi-  
661 dized titanomagnetite. *Geophysical Journal International*, *74*(2), 585–600.
- 662 Ó Conbhuí, P. Ó., Williams, W., Fabian, K., Ridley, P., Nagy, L., & Muxworthy,  
663 A. R. (2018). MERRILL: Micromagnetic Earth Related Robust Interpreted  
664 Language Laboratory. *Geochem. Geophys. Geosyst.*, *19*(4), 1080–1106. doi:  
665 10.1002/2017GC007279
- 666 O'Donovan, J., & O'Reilly, W. (1977). The preparation, characterization and mag-  
667 netic properties of synthetic analogues of some carriers of the palaeomagnetic  
668 record. *Journal of geomagnetism and geoelectricity*, *29*(4), 331–344.
- 669 Özdemir, Ö., & O'Reilly, W. (1978). Magnetic properties of monodomain  
670 aluminium-substituted titanomagnetite. *Physics of the Earth and Planetary*  
671 *Interiors*, *16*(3), 190–195.
- 672 Ozima, M., & Larson, E. (1970). Low-and high-temperature oxidation of titano-  
673 magnetite in relation to irreversible changes in the magnetic properties of  
674 submarine basalts. *Journal of Geophysical Research*, *75*(5), 1003–1017.
- 675 Ozima, M., Ozima, M., & Kaneoka, I. (1968). Potassium-argon ages and magnetic  
676 properties of some dredged submarine basalts and their geophysical implica-  
677 tions. *Journal of Geophysical Research*, *73*(2), 711–723.
- 678 Ozima, M., & Sakamoto, N. (1971). Magnetic properties of synthesized ti-  
679 tanomaghemite. *Journal of Geophysical Research*, *76*(29), 7035–7046.
- 680 Pan, Y., Hill, M. J., & Zhu, R. (2005). Paleomagnetic and paleointensity study of

- 681 an oligocene–miocene lava sequence from the Hannuoba basalts in northern  
682 China. *Physics of the Earth and Planetary Interiors*, 151(1-2), 21–35.
- 683 Paterson, G. A., Roberts, A. P., Mac Niocaill, C., Muxworthy, A. R., Gurioli, L.,  
684 Viramonté, J. G., ... Weider, S. (2010). Paleomagnetic determination of  
685 emplacement temperatures of pyroclastic deposits: an under-utilized tool.  
686 *Bulletin of Volcanology*, 72, 309–330.
- 687 Pauthenet, R., & Bochirol, L. (1951). Aimantation spontanée des ferrites. *J. phys.*  
688 *radium*, 12(3), 249–251.
- 689 Piper, J., Koçbulut, F., Gürsoy, H., Tatar, O., Viereck, L., Lepetit, P., ... Akpınar,  
690 Z. (2013). Palaeomagnetism of the Cappadocian volcanic succession, central  
691 Turkey: Major ignimbrite emplacement during two short (Miocene) episodes  
692 and Neogene tectonics of the Anatolian collage. *Journal of Volcanology and*  
693 *Geothermal Research*, 262, 47–67.
- 694 Rahman, A., & Parry, L. (1978). Titanomagnetites prepared at different oxidation  
695 conditions: hysteresis properties. *Physics of the Earth and Planetary Interiors*,  
696 16(3), 232–239.
- 697 Rave, W., Fabian, K., & Hubert, A. (1998). Magnetic states of small cubic parti-  
698 cles with uniaxial anisotropy. *Journal of Magnetism and Magnetic Materials*,  
699 190(3), 332–348. doi: Doi10.1016/S0304-8853(98)00328-X
- 700 Readman, P., & O'Reilly, W. (1972). Magnetic properties of oxidized (cation-  
701 deficient) titanomagnetites (Fe, Ti, □)<sub>3</sub> O<sub>4</sub>. *Journal of geomagnetism and*  
702 *geolectricity*, 24(1), 69–90.
- 703 Riisager, P., & Riisager, J. (2001). Detecting multidomain magnetic grains in Thel-  
704 lier palaeointensity experiments. *Physics of the Earth and Planetary Interiors*,  
705 125(1), 111–117. doi: [https://doi.org/10.1016/S0031-9201\(01\)00236-9](https://doi.org/10.1016/S0031-9201(01)00236-9)
- 706 Robins, B. W. (1972). *Remanent magnetization in spinel iron-oxides* (Unpublished  
707 doctoral dissertation). UNSW Sydney.
- 708 Rolph, T. (1997). An investigation of the magnetic variation within two recent lava  
709 flows. *Geophysical Journal International*, 130(1), 125–136.
- 710 Sahu, S., & Moskowitz, B. M. (1995). Thermal dependence of magnetocrystalline  
711 anisotropy and magnetostriction constants of single crystal Fe<sub>2.4</sub>Ti<sub>0.6</sub>O<sub>4</sub>. *Geo-*  
712 *physical research letters*, 22(4), 449–452.
- 713 Santos, C. N., & Tauxe, L. (2019). Investigating the accuracy, precision, and  
714 cooling rate dependence of laboratory-acquired thermal remanences during  
715 paleointensity experiments. *Geochem. Geophys. Geosyst.*, 20(1), 383–397. doi:  
716 10.1029/2018GC007946
- 717 Schabes, M. E., & Bertram, H. N. (1988). Magnetization processes in ferromagnetic  
718 cubes. *Journal of Applied Physics*, 64(3), 1347–1357.
- 719 Selkin, P. A., Gee, J. S., Meurer, W. P., & Hemming, S. R. (2008). Paleointen-  
720 sity record from the 2.7 Ga Stillwater Complex, Montana. *Geochem. Geophys.*  
721 *Geosyst.*, 9(12). doi: 10.1029/2008GC001950
- 722 Sherwood, G., Shaw, J., Baer, G., & Mallik, S. B. (1993). The strength of the ge-  
723 omagnetic field during the cretaceous quiet zone: palaeointensity results from  
724 Israeli and Indian lavas. *Journal of geomagnetism and geolectricity*, 45(4),  
725 339–360.
- 726 Syono, Y. (1965). Magnetocrystalline anisotropy and magnetostriction of Fe<sub>3</sub>O<sub>4</sub>-  
727 Fe<sub>2</sub>TiO<sub>4</sub> series-with special application to rocks magnetism. *Jpn. J. Geophys.*,  
728 4, 71–143.
- 729 Syono, Y., & Ishikawa, Y. (1963). Magnetostriction constants of xFe<sub>2</sub>TiO<sub>4</sub> · (1 -  
730 x)Fe<sub>3</sub>O<sub>4</sub>. *Journal of the Physical Society of Japan*, 18(8), 1231–1232.
- 731 Tanaka, H., & Komuro, N. (2009). The Shaw paleointensity method: Can the ARM  
732 simulate the TRM alteration? *Physics of the Earth and Planetary Interiors*,  
733 173(3-4), 269–278.
- 734 Thellier, E. (1941). Sur les propriétés de l'aimantation thermorémanente des terres  
735 cuites. *CR Acad. Sci. Paris*, 213, 1019–1022.

- 736 Thellier, E., & Thellier, O. (1941). Sur les variations thermiques de l'aimantation  
737 thermorémanente des terres cuites. *CR Hebd. Seances Acad. Sci*, 213, 59–61.
- 738 Tsunakawa, H., & Shaw, J. (1994). The Shaw method of palaeointensity determina-  
739 tions and its application to recent volcanic rocks. *Geophysical Journal Interna-*  
740 *tional*, 118(3), 781–787.
- 741 Usov, N. A., & Serebryakova, O. N. (2023). Non uniform micromagnetic states in  
742 spheroidal magnetite nanoparticles. *J. Magn. Magn. Mater.*, 588, 171345. doi:  
743 10.1016/j.jmmm.2023.171345
- 744 Uyeda, S. (1958). Thermo-remanent magnetism as a medium of paleomagnetism,  
745 with special reference to reverse thermo-remanent magnetism. *J. Japan Geo-*  
746 *phys.*, 2, 1–123.
- 747 Valdez-Grijalva, M. A., Nagy, L., Muxworthy, A. R., Williams, W., & Fabian, K.  
748 (2018). The magnetic structure and palaeomagnetic recording fidelity of sub-  
749 micron greigite (Fe<sub>3</sub>S<sub>4</sub>). *Earth and Planetary Science Letters*, 483, 76–89.
- 750 V erard, C., Leonhardt, R., Winklhofer, M., & Fabian, K. (2012). Variations of  
751 magnetic properties in thin lava flow profiles: Implications for the recording of  
752 the Laschamp excursion. *Physics of the Earth and Planetary Interiors*, 200,  
753 10–27.
- 754 Villasante-Marcos, V., & Pav on-Carrasco, F. J. (2014). Palaeomagnetic constraints  
755 on the age of lomo negro volcanic eruption (el hierro, canary islands). *Geo-*  
756 *physical Journal International*, 199(3), 1497–1514.
- 757 Virtanen, P., Gommers, R., Oliphant, T. E., Haberland, M., Reddy, T., Courn-  
758 peau, D., . . . SciPy 1.0 Contributors (2020). SciPy 1.0: Fundamental algo-  
759 rithms for scientific computing in Python. *Nature Methods*, 17, 261–272. doi:  
760 10.1038/s41592-019-0686-2
- 761 Wanamaker, B., & Moskowitz, B. M. (1994). Effect of nonstoichiometry on the  
762 magnetic and electrical properties of synthetic single crystal Fe<sub>2.4</sub>Ti<sub>0.6</sub>O<sub>4</sub>. *Geo-*  
763 *physical Research Letters*, 21(11), 983–986.
- 764 Wang, D., & Van der Voo, R. (2004). The hysteresis properties of multidomain mag-  
765 netite and titanomagnetite/titanomaghemite in mid-ocean ridge basalts. *Earth*  
766 *and Planetary Science Letters*, 220(1-2), 175–184.
- 767 Wechsler, B. A., Lindsley, D. H., & Prewitt, C. T. (1984). Crystal structure and  
768 cation distribution in titanomagnetites (Fe<sub>3-x</sub>Ti<sub>x</sub>O<sub>4</sub>). *American Mineralogist*,  
769 69(7-8), 754–770.
- 770 Williams, H., & Bozorth, R. (1953). Magnetic study of low temperature transforma-  
771 tion in magnetite. *Reviews of Modern Physics*, 25(1), 79.
- 772 Williams, W., & Dunlop, D. J. (1989). Three-dimensional micromagnetic modelling  
773 of ferromagnetic domain structure. *Nature*, 337(6208), 634–637.
- 774 Williams, W., Fabian, K., P., R., Nagy, L., Paterson, G. A., & Muxworthy, A. R.  
775 (n.d.). *Merrill* [software]. Retrieved from <https://bitbucket.org/wynwilliams/merrill>
- 776
- 777 Williams, W., Muxworthy, A. R., & Paterson, G. A. (2006). Configurational  
778 anisotropy in single-domain and pseudosingle-domain grains of magnetite.  
779 *Journal of Geophysical Research: Solid Earth*, 111(B12).
- 780 Witt, A., Fabian, K., & Bleil, U. (2005). Three-dimensional micromagnetic calcu-  
781 lations for naturally shaped magnetite: Octahedra and magnetosomes. *Earth*  
782 *Planet. Sci. Lett.*, 233(3), 311–324. doi: 10.1016/j.epsl.2005.01.043

# Supplementary Material for “Magnetic Domain States and Critical Sizes in the Titanomagnetite Series”

Brendan Cych<sup>1</sup>, Greig A. Paterson<sup>1</sup>, Lesleis Nagy<sup>1</sup>, Wyn Williams<sup>2</sup>, Bruce Moskowitz<sup>3</sup>

<sup>1</sup>Geomagnetism Lab, Department of Earth, Ocean and Environmental Sciences, University of Liverpool, The Oliver Lodge, Oxford St, Liverpool, L69 7ZE, UK

<sup>2</sup>School of GeoSciences, University of Edinburgh, Grant Institute, West Mains Road, Edinburgh, EH9 3JW, UK

<sup>3</sup>Institute for Rock Magnetism, Department of Earth and Environmental Sciences, University of Minnesota, 150 John T. Tate Hall, 116 Church St. SE, Minneapolis, MN 55455U, USA

## Contents of this file

1. Section S1 - Curie Temperatures of Natural Samples
2. Section S2 - Intrinsic Properties of the Titanomagnetite Series
3. Section S3 - Visualization of Magnetization States
4. Figure S1 - Histogram of curie temperatures of igneous rocks
5. Table S1 - Rock magnetic properties for the TM series at 20°C
6. Figure S2 - Curie temperature as a function of titanomagnetite composition
7. Figure S3 - Exchange constant for magnetite as a function of temperature

## S1 - Curie Temperatures of Natural Samples

To demonstrate the importance of our study, we compiled 1391 Curie temperature measurements for igneous rocks from a compilation of 38 papers (Ozima et al., 1968; Larson et al., 1969; Kono, 1974; Coe et al., 1978, 1984; Chauvin et al., 1991; Sherwood et al., 1993; Mankinen, 1994; Tsunakawa & Shaw, 1994; Gonzalez et al., 1997; Rolph, 1997; Hill & Shaw, 1999, 2000; Calvo et al., 2002; Carvallo et al., 2003, 2004; Wang & Van der Voo, 2004; Feinberg et al., 2006; Matzka & Krása, 2007; Böhnelt et al., 2009; Calvo-Rathert et al., 2009, 2011, 2013; Tanaka & Komuro, 2009; Ferik et al., 2010, 2012; Michalk et al., 2010; Paterson et al., 2010; Donadini et al., 2011; Fontana et al., 2011; de Groot et al., 2012, 2013; V erard et al., 2012; Piper et al., 2013; Villasante-Marcos & Pav on-Carrasco, 2014; Ahn et al., 2016; Bowles et al., 2018, 2020). These results were filtered to exclude results which could not be titanomagnetites by using a maximum Curie temperature of 590 C. A histogram of the results (with a maximum shown in Figure S1, ignoring results with a maximum temperature higher than that consistent with magnetite). Around 25% of these measured  $T_C$  values fall into the 580 C bin, indicating that the predominant carrier is magnetite in ~25% of all igneous rocks. This indicates that the remaining 75% have a magnetization predominantly carried by titanomagnetites or other low  $T_C$  magnetic minerals.

## S2 - Intrinsic Properties of the Titanomagnetite Series

To be able to simulate the titanomagnetite (TM<sub>x</sub>, where “x” denotes the titanium percentage) series using the Micromagnetic Earth Related Robust Interpreted Language Laboratory (MERRILL;   Conbhu  et al., 2018), continuous descriptions of intrinsic magnetic properties are needed. This includes compositional variations of the Curie temperature ( $T_C$ ), as well as compositional and temperature dependence of saturation magnetization ( $M_s$ ), the first and second anisotropy constants ( $k_1$  and  $k_2$ , respectively), and the ex-

change interaction constant ( $A_{\text{ex}}$ ). We fit these parameters to existing datasets, cited in their respective sections below. The results of our fits at room temperature for the compositions used in this study are shown in Table S1. Further details are given in the respective sections for each parameter.

## S2.1 - Curie Temperature

A total of 95  $T_C$  data spanning the full compositional range (magnetite to ulvospinel) were compiled from 19 sources (Akimoto et al., 1957; Uyeda, 1958; Syono, 1965; Ozima & Larson, 1970; Readman & O'Reilly, 1972; Robins, 1972; Hauptman, 1974; O'Donovan & O'Reilly, 1977; Rahman & Parry, 1978; Özdemir & O'Reilly, 1978; Keefer & Shive, 1981; Nishitani & Kono, 1983; Heider & Williams, 1988; Moskowitz, 1993; Wanamaker & Moskowitz, 1994; Hunt et al., 1995; Sahu & Moskowitz, 1995; Dunlop & Özdemir, 1997; Moskowitz et al., 1998). The data are presented in Figure S1 alongside the best-fit polynomial of the form:

$$T_C = 372.37x^3 - 691.52x^2 - 413.85x + 580^\circ\text{C}, \quad (1)$$

where  $x$  here denotes a fraction rather than a percentage (e.g.  $x=0.6$  for TM60). The polynomial is constrained such that  $T_C$  is  $580^\circ\text{C}$  for magnetite and  $-153^\circ\text{C}$  for ulvospinel.

## S2.2 - Saturation Magnetization

A data set of 486  $M_s$  measurements from 19 sources were compiled (Pauthenet & Bochirol, 1951; Akimoto et al., 1957; Uyeda, 1958; Syono, 1965; Ozima & Larson, 1970; Ozima & Sakamoto, 1971; Rahman & Parry, 1978; Özdemir & O'Reilly, 1978; Nishitani & Kono, 1983; Wechsler et al., 1984; Moskowitz & Halgedahl, 1987; Newell et al., 1990; Banerjee, 1991; Kākol et al., 1991a, 1991b; Moskowitz, 1993; Kākol et al., 1994; Moskowitz et al., 1998). This represents compositions from TM00 to TM70. MERRILL requires input  $M_s$  values as volume normalized magnetizations in A/m, but some studies report  $M_s$  as mass

normalize in Am<sup>2</sup>/kg. To convert these units, we use a density-composition relationship derived from density data for TM00, TM60, and TM100 (Hunt et al., 1995; Dunlop and Özdemir, 1997):  $\rho(x) = -418.03x + 5194.9$ . The room temperature  $M_s$  values obtained from our fit to the data at the compositions used in this paper are given in Table S1.

### S2.3 - Anisotropy Constants

For  $k_1$ , we compiled a set of 99 data from 13 sources, spanning TM00 to TM68 (Bickford Jr, 1950; Williams & Bozorth, 1953; Calhoun, 1954; Bickford et al., 1957; Syono, 1965; Fletcher & O'Reilly, 1974; Moskowitz & Halgedahl, 1987; Kåkol et al., 1991b; Aragón, 1992; Kåkol et al., 1994; Sahu & Moskowitz, 1995; Hunt et al., 1995; Martín-Hernández et al., 2006).

For  $k_2$  only 27 data points are available from four sources, spanning TM00 to TM55 (Bickford et al., 1957; Syono & Ishikawa, 1963; Kåkol et al., 1991b; Martín-Hernández et al., 2006) We note that the limited compositional range of  $k_2$  data restricts room temperature micromagnetic models to TM00–TM60. The room temperature  $k_1$  and  $k_2$  values obtained from our fits to the data at the compositions used in this paper are given in Table S1.

### S2.4 - Exchange Constant

Limited data are available for the variation of the exchange interaction ( $A_{\text{ex}}$ ) for the titanomagnetite series – data are only available for magnetite at a range of temperatures (Heider & Williams, 1988). A fit to these temperatures yielded the following relation:

$$A_{\text{ex}}(T) = 1.3838 \times 10^{-11} \left(1 - \frac{T}{T_C}\right)^{0.67448}, \quad (2)$$

where  $T$  and  $T_C$  are measured in °C and  $T_C = 580^\circ\text{C}$  for magnetite. The fit to the data is plotted in Figure . This fit results in a room temperature (20°C)  $A_{\text{ex}}$  of  $1.351 \times 10^{-11}$  for magnetite. To scale this for compositional variation in the titanomagnetite series we

use a Curie temperature scaling law proposed by Chikazumi (1964) and used in early TM studies (Butler & Banerjee, 1975; Moskowitz, 1980; Moskowitz & Halgedahl, 1987).  $A_{\text{ex}}$  at room temperature is therefore given by the formula:

$$A_{\text{ex}}(x) = 1.3838 \times 10^{-11} \left( \frac{T_{\text{C}}(x) + 273.15}{853.15} \right) \left( 1 - \frac{20}{T_{\text{C}}(x)} \right)^{0.67448}, \quad (3)$$

where  $T_{\text{C}}(x)$  is given by Equation 1.

### Text S3 - Visualization of Magnetization States

The relative helicity  $h_{\text{rel}}$  - used to calculate the presence of vortex cores and magnetization states is given by the formula:

$$h_{\text{rel}} = \frac{\hat{m} \cdot \nabla \times \hat{m}}{\|\nabla \times \hat{m}\|}, \quad (4)$$

where  $\hat{m}$  is the magnetization unit vector at a given location in the mesh. An isosurface of  $|h_{\text{rel}}| = 0.95$  was plotted for everywhere that  $\|\nabla \times \hat{m}\| \geq 1$  (as  $h_{\text{rel}}$  becomes noisy when  $\|\nabla \times \hat{m}\|$  is close to zero).

$|s_{\text{c}}|$ , used to color the LEM states, is given by:

$$|s_{\text{c}}| = \frac{|\hat{m} \cdot M|}{\|M\|}, \quad M = \iiint_V \hat{m} \, dV. \quad (5)$$

### References

- Ahn, H.-S., Kidane, T., Yamamoto, Y., & Otofujii, Y.-i. (2016). Low geomagnetic field intensity in the matuyama chron: palaeomagnetic study of a lava sequence from afar depression, east africa. *Geophysical Journal International*, *204*(1), 127–146.
- Akimoto, S.-i., Katsura, T., & Yoshida, M. (1957). Magnetic properties of  $\text{TiFe}_2\text{O}_4\text{-Fe}_3\text{O}_4$  system and their change with oxidation. *J. Geomagn. Geoelec.*, *9*(4), 165–178. doi: 10.5636/jgg.9.165

- Aragón, R. (1992). Cubic magnetic anisotropy of nonstoichiometric magnetite. *Physical Review B*, 46(9), 5334.
- Banerjee, S. K. (1991). Magnetic properties of Fe-Ti oxides. In D. H. Lindsley (Ed.), *Oxide minerals: Petrologic and magnetic significance* (pp. 107–128). Berlin, Boston: De Gruyter. doi: 10.1515/9781501508684-007
- Bickford, L., Brownlow, J., & Penoyer, R. (1957). Magnetocrystalline anisotropy in cobalt-substituted magnetite single crystals. *Proceedings of the IEE-Part B: Radio and Electronic Engineering*, 104(5S), 238–244.
- Bickford Jr, L. (1950). Ferromagnetic resonance absorption in magnetite single crystals. *Physical Review*, 78(4), 449.
- Böhnel, H. N., Dekkers, M. J., Delgado-Argote, L. A., & Gratton, M. N. (2009). Comparison between the microwave and multispecimen parallel difference pTRM paleointensity methods. *Geophysical Journal International*, 177(2), 383–394.
- Bowles, J. A., Gerzich, D. M., & Jackson, M. J. (2018). Assessing new and old methods in paleomagnetic paleothermometry: a test case at Mt. St. Helens, USA. *Geochemistry, Geophysics, Geosystems*, 19(6), 1714–1730.
- Bowles, J. A., Morris, A., Tivey, M., & Lascu, I. (2020). Magnetic mineral populations in lower oceanic crustal gabbros (Atlantis bank, SW Indian ridge): Implications for marine magnetic anomalies. *Geochemistry, Geophysics, Geosystems*, 21(3), e2019GC008847.
- Butler, R. F., & Banerjee, S. K. (1975). Theoretical single-domain grain size range in magnetite and titanomagnetite. *J. Geophys. Res.*, 80(29), 4049–4058. doi: 10.1029/JB080i029p04049
- Calhoun, B. (1954). Magnetic and electric properties of magnetite at low temperatures. *Physical Review*, 94(6), 1577.

- Calvo, M., Prévot, M., Perrin, M., & Riisager, J. (2002). Investigating the reasons for the failure of palaeointensity experiments: a study on historical lava flows from Mt. Etna (Italy). *Geophysical journal international*, *149*(1), 44–63.
- Calvo-Rathert, M., Bógalo, M. F., Gogichaishvili, A., Sologashvili, J., & Vashakidze, G. (2013). New paleomagnetic and paleointensity data from pliocene lava flows from the lesser caucasus. *Journal of Asian Earth Sciences*, *73*, 347–361.
- Calvo-Rathert, M., Goguitchaichvili, A., Bógalo, M.-F., Vegas-Tubía, N., Carrancho, Á., & Sologashvili, J. (2011). A paleomagnetic and paleointensity study on pleistocene and pliocene basaltic flows from the djavakheti highland (southern georgia, caucasus). *Physics of the Earth and Planetary interiors*, *187*(3-4), 212–224.
- Calvo-Rathert, M., Goguitchaichvili, A., & Vegas-Tubia, N. (2009). A paleointensity study on middle miocene to pliocene volcanic rocks from south-eastern spain. *Earth, planets and space*, *61*, 61–69.
- Carvallo, C., Camps, P., Ruffet, G., Henry, B., & Poidras, T. (2003). Mono lake or Laschamp geomagnetic event recorded from lava flows in Amsterdam island (south-eastern Indian Ocean). *Geophysical Journal International*, *154*(3), 767–782.
- Carvallo, C., Özdemir, Ö., & Dunlop, D. J. (2004). Palaeointensity determinations, palaeodirections and magnetic properties of basalts from the Emperor seamounts. *Geophysical Journal International*, *156*(1), 29–38.
- Chauvin, A., Gillot, P.-Y., & Bonhommet, N. (1991). Paleointensity of the Earth's magnetic field recorded by two late quaternary volcanic sequences at the island of La Réunion (Indian ocean). *Journal of Geophysical Research: Solid Earth*, *96*(B2), 1981–2006.
- Chikazumi, S. (1964). *Physics of magnetism*. John Wiley & Sons.
- Coe, R. S., Grommé, S., & Mankinen, E. A. (1978). Geomagnetic paleointensities from

radiocarbon-dated lava flows on Hawaii and the question of the Pacific nondipole low.

*Journal of Geophysical Research: Solid Earth*, 83(B4), 1740–1756.

Coe, R. S., Gromme, S., & Mankinen, E. A. (1984). Geomagnetic paleointensities from excursion sequences in lavas on Oahu, Hawaii. *Journal of Geophysical Research: Solid Earth*, 89(B2), 1059–1069.

de Groot, L. V., Dekkers, M. J., & Mullender, T. A. (2012). Exploring the potential of acquisition curves of the anhysteretic remanent magnetization as a tool to detect subtle magnetic alteration induced by heating. *Physics of the Earth and Planetary Interiors*, 194, 71–84.

de Groot, L. V., Mullender, T. A., & Dekkers, M. J. (2013). An evaluation of the influence of the experimental cooling rate along with other thermomagnetic effects to explain anomalously low palaeointensities obtained for historic lavas of Mt Etna (Italy). *Geophysical Journal International*, 193(3), 1198–1215.

Donadini, F., Elming, S.-Å., Tauxe, L., & Hålenius, U. (2011). Paleointensity determination on a 1.786 Ga old gabbro from Hoting, central Sweden. *Earth and Planetary Science Letters*, 309(3-4), 234–248.

Dunlop, D. J., & Özdemir, Ö. (1997). *Rock magnetism: fundamentals and frontiers* (No. 3). Cambridge University Press.

Feinberg, J. M., Harrison, R. J., Kasama, T., Dunin-Borkowski, R. E., Scott, G. R., & Renne, P. R. (2006). Effects of internal mineral structures on the magnetic remanence of silicate-hosted titanomagnetite inclusions: An electron holography study. *Journal of Geophysical Research: Solid Earth*, 111(B12).

Ferk, A., Aulock, F. v., Leonhardt, R., Hess, K.-U., & Dingwell, D. (2010). A cooling rate bias in paleointensity determination from volcanic glass: An experimental demonstration. *Journal of Geophysical Research: Solid Earth*, 115(B8).

- Ferk, A., Denton, J., Leonhardt, R., Tuffen, H., Koch, S., Hess, K.-U., & Dingwell, D. (2012). Paleointensity on volcanic glass of varying hydration states. *Physics of the Earth and Planetary Interiors*, 208, 25–37.
- Fletcher, E., & O'Reilly, W. (1974). Contribution of  $\text{Fe}^{2+}$  ions to the magnetocrystalline anisotropy constant  $k_1$  of  $\text{Fe}_{3-x}\text{Ti}_x\text{O}_4$  ( $0 < x < 1$ ). *Journal of Physics C: Solid State Physics*, 7(1), 171.
- Fontana, G., Mac Niocaill, C., Brown, R. J., Sparks, R. S. J., & Field, M. (2011). Emplacement temperatures of pyroclastic and volcanoclastic deposits in kimberlite pipes in southern Africa. *Bulletin of Volcanology*, 73, 1063–1083.
- Gonzalez, S., Sherwood, G., Böhnell, H., & Schnepf, E. (1997). Palaeosecular variation in central Mexico over the last 30000 years: the record from lavas. *Geophysical Journal International*, 130(1), 201–219.
- Hauptman, Z. (1974). High temperature oxidation, range of non-stoichiometry and curie point variation of cation deficient titanomagnetite  $\text{Fe}_{2.4}\text{Ti}_{0.6}\text{O}_{4+\gamma}$ . *Geophysical Journal International*, 38(1), 29–47.
- Heider, F., & Williams, W. (1988). Note on temperature dependence of exchange constant in magnetite. *Geophysical Research Letters*, 15(2), 184–187.
- Hill, M. J., & Shaw, J. (1999). Palaeointensity results for historic lavas from Mt Etna using microwave demagnetization/remagnetization in a modified Thellier-type experiment. *Geophysical Journal International*, 139(2), 583–590.
- Hill, M. J., & Shaw, J. (2000). Magnetic field intensity study of the 1960 Kilauea lava flow, Hawaii, using the microwave palaeointensity technique. *Geophysical Journal International*, 142(2), 487–504.
- Hunt, C. P., Moskowitz, B. M., & Banerjee, S. K. (1995). Magnetic properties of rocks and minerals. *Rock physics and phase relations: A handbook of physical constants*,

3, 189–204.

Kąkol, Z., Sabol, J., & Honig, J. (1991a). Cation distribution and magnetic properties of titanomagnetites  $\text{Fe}_{3-x}\text{Ti}_x\text{O}_4$  ( $0 \leq x < 1$ ). *Physical Review B*, *43*(1), 649.

Kąkol, Z., Sabol, J., & Honig, J. (1991b). Magnetic anisotropy of titanomagnetites  $\text{Fe}_{3-x}\text{Ti}_x\text{O}_4$  ( $0 \leq x < 0.55$ ). *Physical Review B*, *44*(5), 2198.

Kąkol, Z., Sabol, J., Stickler, J., Kozłowski, A., & Honig, J. (1994). Influence of titanium doping on the magnetocrystalline anisotropy of magnetite. *Physical Review B*, *49*(18), 12767.

Keefer, C. M., & Shive, P. N. (1981). Curie temperature and lattice constant reference contours for synthetic titanomaghemites. *Journal of Geophysical Research: Solid Earth*, *86*(B2), 987–998.

Kono, M. (1974). Intensities of the Earth's magnetic field about 60 my ago determined from the Deccan trap basalts, India. *Journal of Geophysical Research*, *79*(8), 1135–1141.

Larson, E., Ozima, M., Ozima, M., Nagata, T., & Strangway, D. (1969). Stability of remanent magnetization of igneous rocks. *Geophysical Journal International*, *17*(3), 263–292.

Mankinen, E. A. (1994). *Preliminary geomagnetic paleointensities from long valley caldera, california*. US Geological Survey.

Martín-Hernández, F., Bominaar-Silkens, I. M., Dekkers, M. J., & Maan, J. K. (2006). High-field cantilever magnetometry as a tool for the determination of the magnetocrystalline anisotropy of single crystals. *Tectonophysics*, *418*(1-2), 21–30.

Matzka, J., & Krása, D. (2007). Oceanic basalt continuous thermal demagnetization curves. *Geophysical Journal International*, *169*(3), 941–950.

Michalk, D. M., Biggin, A. J., Knudsen, M. F., Böhnell, H. N., Nowaczyk, N. R., Ownby,

- S., & López-Martínez, M. (2010). Application of the multispecimen palaeointensity method to pleistocene lava flows from the Trans-Mexican volcanic belt. *Physics of the Earth and Planetary Interiors*, 179(3-4), 139–156.
- Moskowitz, B. M. (1980). Theoretical grain size limits for single-domain, pseudo-single-domain and multi-domain behavior in titanomagnetite ( $x = 0.6$ ) as a function of low-temperature oxidation. *Earth Planet. Sci. Lett.*, 47(2), 285–293. doi: 10.1016/0012-821X(80)90045-X
- Moskowitz, B. M. (1993). High-temperature magnetostriction of magnetite and titanomagnetites. *Journal of Geophysical Research: Solid Earth*, 98(B1), 359–371.
- Moskowitz, B. M., & Halgedahl, S. L. (1987). Theoretical temperature and grain-size dependence of domain state in  $x=0.6$  titanomagnetite. *Journal of Geophysical Research: Solid Earth*, 92(B10), 10667–10682.
- Moskowitz, B. M., Jackson, M., & Kissel, C. (1998). Low-temperature magnetic behavior of titanomagnetites. *Earth and Planetary Science Letters*, 157(3-4), 141–149.
- Newell, A. J., Dunlop, D. J., & Enkin, R. J. (1990). Temperature dependence of critical sizes, wall widths and moments in two-domain magnetite grains. *Physics of the earth and planetary interiors*, 65(1-2), 165–176.
- Nishitani, T., & Kono, M. (1983). Curie temperature and lattice constant of oxidized titanomagnetite. *Geophysical Journal International*, 74(2), 585–600.
- Ó Conbhuí, P. Ó., Williams, W., Fabian, K., Ridley, P., Nagy, L., & Muxworthy, A. R. (2018). MERRILL: Micromagnetic Earth Related Robust Interpreted Language Laboratory. *Geochem. Geophys. Geosyst.*, 19(4), 1080–1106. doi: 10.1002/2017GC007279
- O'Donovan, J., & O'Reilly, W. (1977). The preparation, characterization and magnetic properties of synthetic analogues of some carriers of the palaeomagnetic record.

- Journal of geomagnetism and geoelectricity*, 29(4), 331–344.
- Özdemir, Ö., & O'Reilly, W. (1978). Magnetic properties of monodomain aluminium-substituted titanomagnetite. *Physics of the Earth and Planetary Interiors*, 16(3), 190–195.
- Ozima, M., & Larson, E. (1970). Low-and high-temperature oxidation of titanomagnetite in relation to irreversible changes in the magnetic properties of submarine basalts. *Journal of Geophysical Research*, 75(5), 1003–1017.
- Ozima, M., Ozima, M., & Kaneoka, I. (1968). Potassium-argon ages and magnetic properties of some dredged submarine basalts and their geophysical implications. *Journal of Geophysical Research*, 73(2), 711–723.
- Ozima, M., & Sakamoto, N. (1971). Magnetic properties of synthesized titanomaghemite. *Journal of Geophysical Research*, 76(29), 7035–7046.
- Paterson, G. A., Roberts, A. P., Mac Niocaill, C., Muxworthy, A. R., Gurioli, L., Viramonté, J. G., ... Weider, S. (2010). Paleomagnetic determination of emplacement temperatures of pyroclastic deposits: an under-utilized tool. *Bulletin of Volcanology*, 72, 309–330.
- Pauthenet, R., & Bochirol, L. (1951). Aimantation spontanée des ferrites. *J. phys. radium*, 12(3), 249–251.
- Piper, J., Koçbulut, F., Gürsoy, H., Tatar, O., Viereck, L., Lepetit, P., ... Akpınar, Z. (2013). Palaeomagnetism of the Cappadocian volcanic succession, central Turkey: Major ignimbrite emplacement during two short (Miocene) episodes and Neogene tectonics of the Anatolian collage. *Journal of Volcanology and Geothermal Research*, 262, 47–67.
- Rahman, A., & Parry, L. (1978). Titanomagnetites prepared at different oxidation conditions: hysteresis properties. *Physics of the Earth and Planetary Interiors*, 16(3),

232–239.

- Readman, P., & O'Reilly, W. (1972). Magnetic properties of oxidized (cation-deficient) titanomagnetites (Fe, Ti, □)<sub>3</sub>O<sub>4</sub>. *Journal of geomagnetism and geoelectricity*, *24*(1), 69–90.
- Robins, B. W. (1972). *Remanent magnetization in spinel iron-oxides* (Unpublished doctoral dissertation). UNSW Sydney.
- Rolph, T. (1997). An investigation of the magnetic variation within two recent lava flows. *Geophysical Journal International*, *130*(1), 125–136.
- Sahu, S., & Moskowitz, B. M. (1995). Thermal dependence of magnetocrystalline anisotropy and magnetostriction constants of single crystal Fe<sub>2.4</sub>Ti<sub>0.6</sub>O<sub>4</sub>. *Geophysical research letters*, *22*(4), 449–452.
- Sherwood, G., Shaw, J., Baer, G., & Mallik, S. B. (1993). The strength of the geomagnetic field during the cretaceous quiet zone: palaeointensity results from Israeli and Indian lavas. *Journal of geomagnetism and geoelectricity*, *45*(4), 339–360.
- Syono, Y. (1965). Magnetocrystalline anisotropy and magnetostriction of Fe<sub>3</sub>O<sub>4</sub>-Fe<sub>2</sub>TiO<sub>4</sub> series-with special application to rocks magnetism. *Jpn. J. Geophys.*, *4*, 71–143.
- Syono, Y., & Ishikawa, Y. (1963). Magnetostriction constants of  $x\text{Fe}_2\text{TiO}_4 \cdot (1-x)\text{Fe}_3\text{O}_4$ . *Journal of the Physical Society of Japan*, *18*(8), 1231–1232.
- Tanaka, H., & Komuro, N. (2009). The Shaw paleointensity method: Can the ARM simulate the TRM alteration? *Physics of the Earth and Planetary Interiors*, *173*(3-4), 269–278.
- Tsunakawa, H., & Shaw, J. (1994). The Shaw method of palaeointensity determinations and its application to recent volcanic rocks. *Geophysical Journal International*, *118*(3), 781–787.
- Uyeda, S. (1958). Thermo-remanent magnetism as a medium of paleomagnetism, with

- special reference to reverse thermo-remanent magnetism. *J. Japan Geophys.*, 2, 1–123.
- Vérard, C., Leonhardt, R., Winklhofer, M., & Fabian, K. (2012). Variations of magnetic properties in thin lava flow profiles: Implications for the recording of the Laschamp excursion. *Physics of the Earth and Planetary Interiors*, 200, 10–27.
- Villasante-Marcos, V., & Pavón-Carrasco, F. J. (2014). Palaeomagnetic constraints on the age of lomo negro volcanic eruption (el hierro, canary islands). *Geophysical Journal International*, 199(3), 1497–1514.
- Wanamaker, B., & Moskowitz, B. M. (1994). Effect of nonstoichiometry on the magnetic and electrical properties of synthetic single crystal  $\text{Fe}_{2.4}\text{Ti}_{0.6}\text{O}_4$ . *Geophysical Research Letters*, 21(11), 983–986.
- Wang, D., & Van der Voo, R. (2004). The hysteresis properties of multidomain magnetite and titanomagnetite/titanomaghemite in mid-ocean ridge basalts. *Earth and Planetary Science Letters*, 220(1-2), 175–184.
- Wechsler, B. A., Lindsley, D. H., & Prewitt, C. T. (1984). Crystal structure and cation distribution in titanomagnetites ( $\text{Fe}_{3-x}\text{Ti}_x\text{O}_4$ ). *American Mineralogist*, 69(7-8), 754–770.
- Williams, H., & Bozorth, R. (1953). Magnetic study of low temperature transformation in magnetite. *Reviews of Modern Physics*, 25(1), 79.

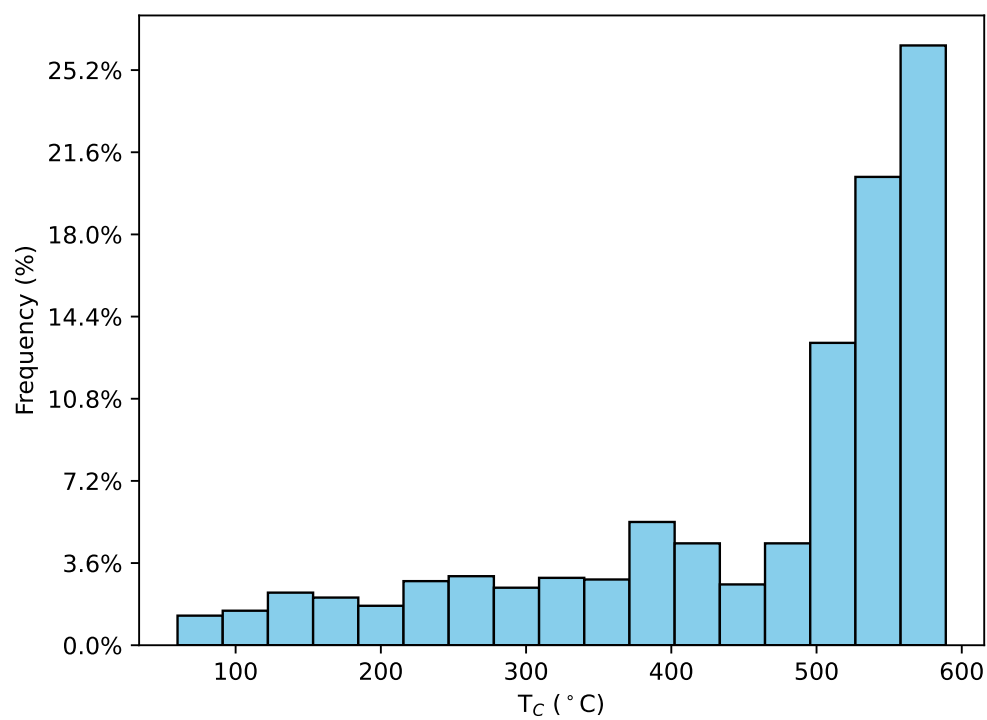


**Figure S1.** Histogram of measured Curie temperatures of igneous rocks from a compilation of 38 papers.

**Table S1.** Rock magnetic properties for the TM series at 20°C, generated by fitting to the datasets referenced in the text.

x (%)	$T_C$ (°C)	$M_s$ (kA/m)	$k_1$ ( $10^4$ J/m <sup>3</sup> )	$k_2$ ( $10^4$ J/m <sup>3</sup> )	$A_{ex}$ ( $10^{-11}$ J/m)
0	580.00	488.46	-1.2209	-0.4303	1.3514
5	557.63	450.33	-1.7818	0.0841	1.3147
10	532.07	414.59	-2.1315	0.3954	1.2727
15	503.62	381.01	-2.2983	0.5217	1.2259
20	472.55	349.40	-2.3095	0.4995	1.1747
25	439.14	319.54	-2.1919	0.3826	1.1196
30	403.66	291.22	-1.9718	0.2385	1.0608
35	366.41	264.22	-1.6752	0.1452	0.9988
40	327.65	238.33	-1.3274	0.1826	0.9340
45	287.67	213.32	-0.9534	0.4214	0.8665
50	246.74	188.96	-0.5781	0.9008	0.7965
55	205.15	164.97	-0.2261	1.5900	0.7239
60	163.17	141.06	0.0772	2.3172	0.6480

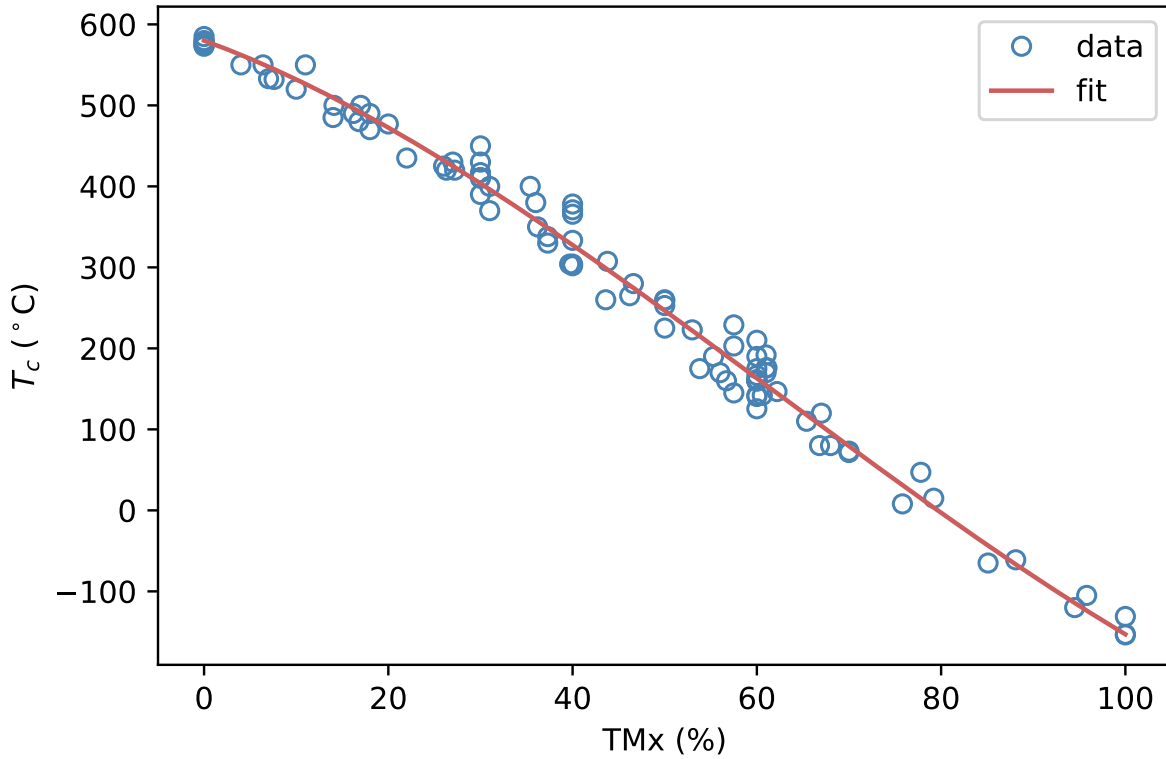


**Figure S1.** Curie temperature as a function of titanomagnetite composition. Blue circles: Individual data points, Red line: polynomial fit to data.

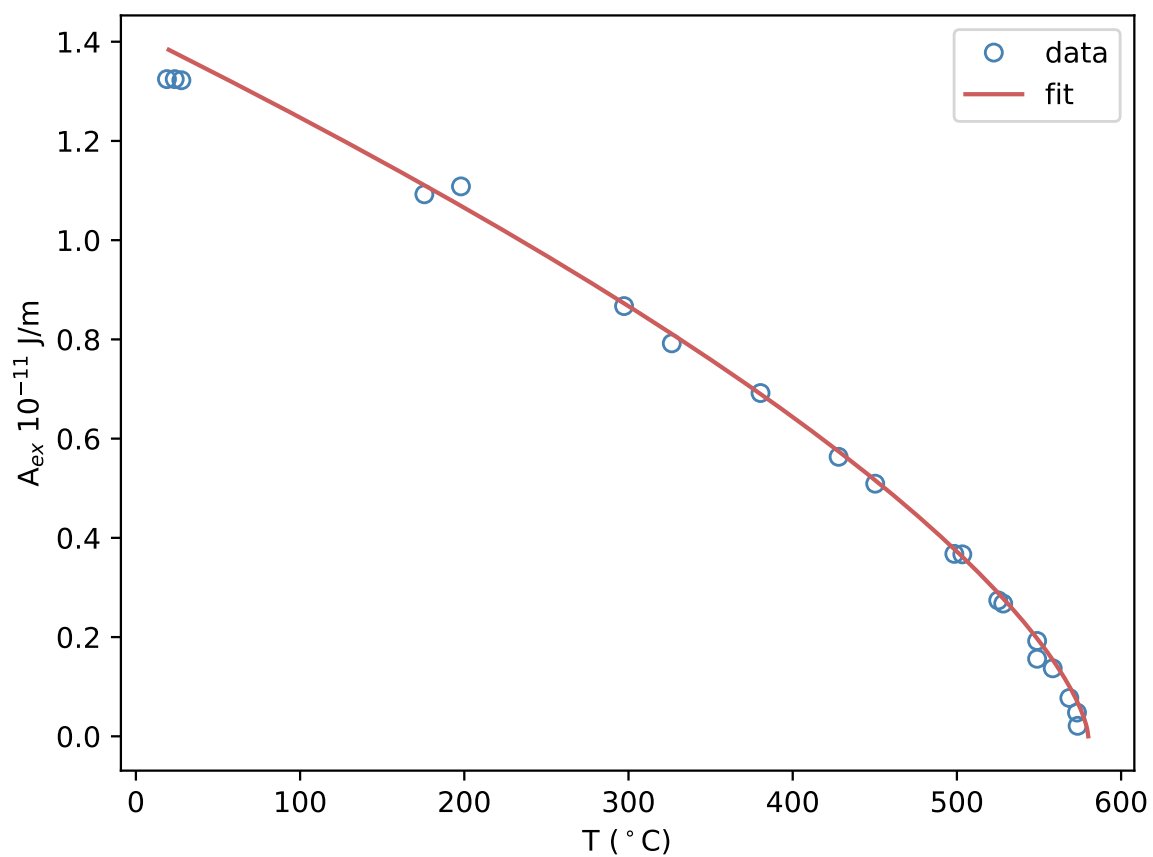


**Figure S2.** Exchange constant for magnetite as a function of temperature (blue circles) and fit to these data (red line) given by Equation 2.